

Optical modeling of holographic memory
employing angularly multiplexed recording
and
improvement of optical quality of
reproduced holographic image

Kenichi Shimada

February 2021

Optical modeling of holographic memory
employing angularly multiplexed recording
and
improvement of optical quality of
reproduced holographic image

Kenichi Shimada
Doctoral Program in Engineering Sciences
Subprogram in Applied Physics

Submitted to the
Degree Programs in Pure and Applied Sciences of the
Graduate School of Science and Technology
in Partial Fulfillment of the Requirements
for the Degree of Doctor of Philosophy in
Engineering

at the
University of Tsukuba

Abstract

The volume of digital data in the worldwide is expanding exponentially every year, then there are many opportunities that require long-term data preservation (LTDP) because of not only complying with laws and regulations, but also utilization on business as an important asset from the viewpoint of Artificial Intelligence and Data Analytics. The storage media for LTDP is required to store digital data at a low cost because reducing the total cost of ownership is important. The holographic memory employing angularly multiplexed recording that the dissertation focuses on is a promising candidate as a storage system for LTDP owing to its longevity and low running cost. To realize high recording density which is enough to achieve comparable bit cost against Tape, the dissertation aimed to explore the feasibility of the targeted recording density of 1 [Tbit/in²].

There are several deterioration factors which degenerates the signal quality of the data channel. Among them, the dissertation has clarified polarization and vibration effects on optical quality of a 2-dimensional (2D) reproduced holographic image, which have not been sufficiently discussed at previous literatures. The effect of polarization states of reference and signal beams during recording and readout on a signal amplitude of a reproduced holographic page data was analytically formulated. The amplitude was able to be expressed in the form of multiplying a signal amplitude calculated from scalar diffraction theory by attenuation coefficients dependent on the polarization states. And the effects of vibration due to mechanical instabilities were formalized by incorporating the concept of time-average holography. The validity of these developed optical model was confirmed through the comparison of simulation with experiments.

Then, the system noise of designed holographic memory at the targeted recording density was estimated to confirm the feasibility of the targeted recording density. Owing to the noise mitigation, such as applying s-polarized reference beam for readout hologram and shorter exposure less than 0.3 [ms] for recording hologram, the system noise was significantly reduced but still exceeded the permissible level. For further improvement of the system noise, the method of compensation for positional error of holographic disk has been devised to strike a balance between high density recording and fast readout. As a result, the system noise was successively reduced below the permissible level, then the feasibility of the targeted recording density of 1 [Tbit/in²] was confirmed through numerical analysis and experiments.

Owing to the results, the realization of a HDSS employing angularly multiplexed recording with the comparable bit cost against Tape became highly promising.

Acknowledgements

First of all, I would like to express my sincere gratitude to my advisor Professor Masahide Itoh for warm guidance and constructive suggestions. He always gave me appropriate advice and patiently watched over me while my progress was slow because of sudden changes of my work in Hitachi due to transfer and difficult situation due to COVID-19 pandemic.

And I would like to thank my thesis committee: Associate Professor Masaki Hada, Lecturer Norio Watanabe, Professor Yoshiaki Yasuno, and Professor Tsutomu Shimura, for their insightful comments and advice that made my research of great achievement. Additionally, I would like to thank Professor Tsutomu Shimura for always kindly consulting me, in particular optical modeling of holographic memory and technique of numerical calculation from the beginning of my research on holographic memory in Hitachi.

Then, I am very grateful to Associate Professor Yuzuru Takashima for giving me the experience as a visiting scholar and supporting research life at University of Arizona. Through your constructive advice, I was able to achieve the research results to start my doctoral dissertation.

Also, I would like to thank all the folks at Hitachi where this research was performed, for their valuable cooperation in my research. The research was not able to be accomplished without the cooperation.

Finally, I would like to express my deepest gratitude to my parents, and especially my wife for her patience and tolerance. I could not be able to finish this work without your support.

Contents

Abstract	i
Acknowledgements	ii
1 Introduction	1
1.1 Research Background	1
1.1.1 Positioning of optical data storage in the era of information explosion	1
1.1.2 Holographic memory as next generation of optical data storage	2
1.1.3 Deterioration factors of holographic image discussed at previous literatures	4
1.1.4 Deterioration factors of holographic image to be discussed	5
1.2 Research Aim and Objectives	7
1.3 Structure of the Dissertation	8
2 Optical Modeling and Analysis of Polarization Effect on Reproduced Holographic Image	10
2.1 Method	10
2.1.1 Mathematical formulation of polarization effect on amplitude of reproduced beam	10
2.1.2 Method of deriving normalized polarization vector of reproduced beam	15
2.2 Experimental setup	17
2.3 Results & Discussion	20
2.3.1 Numerical results of attenuation coefficients due to polarization effect	20
2.3.2 Verification of method of estimating attenuation coefficients	26
2.3.3 Method of suppressing polarization effect on intensity profile	27
2.4 Conclusions	29

3	Optical Modeling and Analysis of Vibration Effect on Reproduced Holographic Image	31
3.1	Mathematical formulation of mechanical instability effect on reproduced beam.....	31
3.1.1	Concept of time-average holography	31
3.1.2	Incorporation of the concept of time-average holography into the modeling of HDSS.....	34
3.1.3	Oscillation effect of reference beam angle on reproduced beam	35
3.1.4	Oscillation effect of holographic disk location on reproduced beam	37
3.2	Optical compensation for mechanical instability effect.....	40
3.3	Results and Discussion.....	42
3.3.1	Validity of optical modeling of oscillation effect.....	42
3.3.2	Effect of optical method of compensation for mechanical vibration effect	49
3.3.3	Suppression of vibration effects on reproduced holographic image	53
3.4	Conclusions.....	54
4	Estimation of System Noise at Recording Density of 1 Tbit/in²	55
4.1	Parameters of optical system for realizing bit cost of 0.01 [\$/GB].....	55
4.2	Estimation of system noise	58
4.2.1	Signal quality metric to estimate system noise.....	58
4.2.2	System noise at recording density of 1 Tbit/in ²	59
4.3	Conclusions.....	64
5	Technique to Compensate for Influence of Disk De-track.....	65
5.1	Methods.....	65
5.1.1	Compensation for effect of positioning error of holographic disk	65
5.1.2	Positioning error signal for Nyquist aperture control	68

5.2	Results and discussion	71
5.2.1	Validity of compensation for effect of positioning error of holographic disk.....	71
5.2.2	Verification of method for generating positioning error signal.....	73
5.2.3	System noise after compensation for effect of positioning error of holographic disk.....	82
5.3	Conclusions.....	84
6	Conclusions	86
	Bibliography	89
	List of Publications	93

Chapter 1

Introduction

1.1 Research Background

1.1.1 Positioning of optical data storage in the era of information explosion

According to International Data Corporation (IDC) reports¹⁾, the volume of digital data in our society is expanding exponentially every year because of the tremendous growth of the industry of information technology, and it is estimated that 40 zettabytes (1 zettabyte (ZB) = 10^{21} bytes) of digital data will be generated worldwide by 2020, and 163ZB by 2025. Some of these digital data require long-term data preservation (LTDP) for such as regulatory and compliance, even if these data are not frequently accessed. The tendency of LTDP is increasing not only for the purpose of regulatory and compliance but also for considering it as an important asset for the future utilization on business due to the rise of Artificial Intelligence (AI) and Data Analytics.

For data storage, the concept of tiered storage management²⁾ is generally applied to data storage system because reducing the total cost of ownership (TCO) is important. The concept is a way to store digital data on adequate storage media based on the feature of the data such as frequency of the data usage. Therefore, the data storage system is tiered and composed of various types of storage media in a hierarchy [Fig. 1.1] such as flash storage, hard disk drive (HDD), Tape and optical storage.

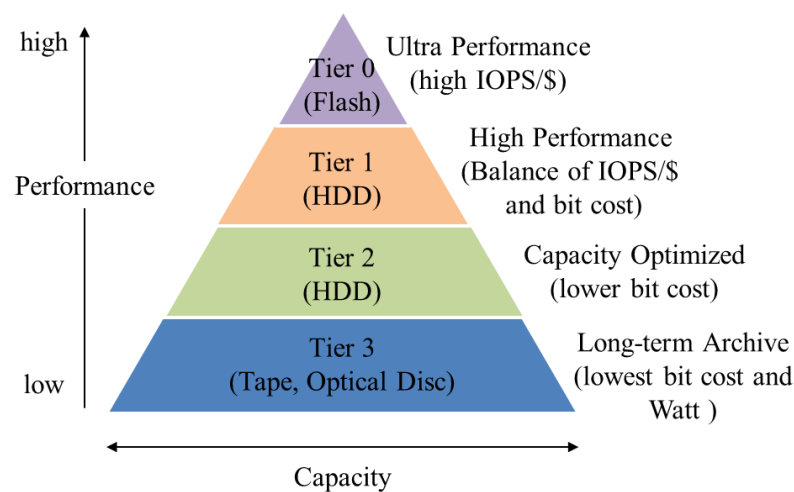


Fig. 1.1 Example of tiered storage.

In general, frequently accessed data is stored on ultra-performance storage media such as flash storage that is usually expensive, and infrequently accessed data that require for LTDP is stored on the lowest bit cost storage media such as Tape media. Figure 1.2 shows the trend of bit cost of each storage media.³⁾ Although the bit cost reductions are slowing, the bit cost of Tape is close to 0.01 [\$/GB]. Owing to the lowest bit cost, Tape storage media have been used for LTDP so far.

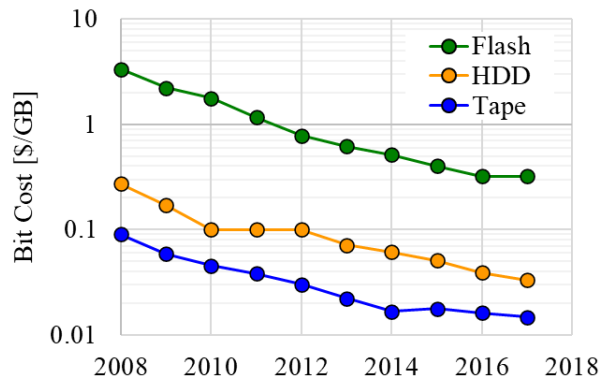


Fig. 1.2 Trend of bit cost of Flash, HDD and Tape.

On the other hand, optical data storage (ODS) is also suitable for LTDP because of its longevity and low running cost. ODS has an advantage over Tape in random-access capability and longevity.⁴⁾ In addition, ODS has a potential of lower running cost than Tape because new generation of Tape is introduced every approximately three years and basically compatible with only the previous two generations.⁵⁾ Considering the situation, data migration about once in less than every ten years will be required for Tape. The migration needs extra operational costs. Moreover, ODS mitigates the environmental load due to its low CO₂ emissions.⁶⁾ For transition to a low-carbon society, ODS is strongly expected as storage media for LTDP.

1.1.2 Holographic memory as next generation of optical data storage

In order to establish ODS as a storage system for LTDP, competitive bit cost against Tape should be realized; consequently, further high-density recording is required. A data capacity of ODS has increased step by step and has been achieved up to 128GB per single-side of disc by the BDXL™ format. The technological trend of increasing data capacity from Compact Disc (CD) to Blu-ray Disc™ (BD) relies on reducing the size of the diffraction limited spot by using a laser beam of shorter wavelength and an objective lens of larger numerical aperture (*NA*). However, the wavelength and *NA* in current BD system are already 405nm and 0.85,

respectively. As long as the same technological trend is simply applied, further improvement of recording density can't be expected because material for optical components applicable to ultra-violet wavelength range is lacking and maximum NA in air is generally limited to be less than one.

Holographic Data Storage System (HDSS) is one of promising candidates for future ODS system toward achieving a data capacity of over 1TB/disk.⁷⁻⁹⁾ If holographic disks of 1TB/disk can be supplied with less than \$10/disk, a bit cost less than 0.01 [\$/GB] that is comparable to Tape media will be realized. HDSS can record an encoded two-dimensional (2D) data page with around a couple of million pixels even with a short single light pulse, and hundreds of data pages can be multiplexed at the same location in the media.¹⁰⁾ Considering these features, HDSS has a high possibility of becoming Post BD system. Up until now, several optical architectures for HDSS have been proposed.¹⁰⁻¹⁶⁾ These are classified broadly into three categories as shown in Figure 1.3. The optical architecture for angularly multiplexed recording generally has two optical paths for a signal beam and a reference beam with an off-axis optical configuration.¹⁰⁻¹²⁾ Regarding the optical architecture for shift multiplexed recording, a reference beam and a signal beam are bundled on the same optical axis and irradiated on a holographic medium through a single objective lens.^{13,14)} Regarding the optical architecture for micro hologram recording, two counter-propagating signal and reference beams are configured to record bitwise information similar to BD system.^{15,16)}

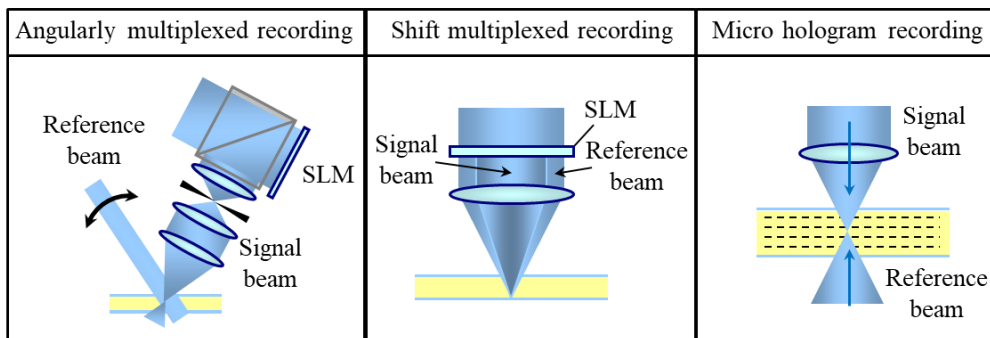


Fig. 1.3 Representative optical architectures for HDSS.

Considering that recording density is proportional to the square of NA of objective lens,¹⁷⁾ the angularly multiplexed recording has an advantage of high-density recording among these architectures. An objective lens of a high NA can be easily introduced into the system because of its off-axis optical configuration which has large angle between the reference and signal beams. In the dissertation, holographic memory employing angularly multiplexed recording is set as subject of research.

1.1.3 Deterioration factors of holographic image discussed at previous literatures

However, using a high NA objective lens for achieving higher recording density will be advantageous only if the uniformity of a signal intensity profile of a reproduced 2D holographic page data on a camera is maintained over the entire area of the page. An inhomogeneous intensity profile of the page data degenerates the signal quality of the data channel. A high NA objective lens tends to induce an inhomogeneous intensity distribution in the page data because the area of the 2D page data becomes large; consequently, it becomes difficult to maintain the uniformity of the intensity distribution over the entire area of the page. There are several factors which induces the inhomogeneous intensity distribution. Representative factors are described below.

(a) Gaussian intensity profile emitted from a laser source

One of main factors is a Gaussian intensity profile emitted from a laser source. Although it is preferable to capture laser beam until the range of the base of Gaussian profile to increase optical throughput in terms of data transfer rates, the situation leads to deterioration of uniformity of intensity profile. Regarding the situation, several research groups have proposed a beam shaper architecture which converts collimated Gaussian input beams into collimated top-hat beams.^{18,19)} Owing to the architecture, a balance between optical throughput and a uniform intensity distribution of input laser beam can be maintained.

(b) Thermal expansion/contraction of a holographic medium

After the improvement of uniformity of intensity distribution of input laser beam, Bragg mismatch which is caused by such as angular or wavelength detuning from the Bragg matching condition is another main factor which degrades intensity profile of reproduced holographic image. The higher NA objective lens makes an area size of the page to be large; consequently, it becomes difficult to keep Bragg matching condition over the entire area of the page. Thermal expansion or contraction is a representative example which causes Bragg mismatch. Previous literatures have dealt with the thermal effect on holographic memory.²⁰⁻²⁴⁾ They established the model combined the fringe-plane rotation model²⁰⁾ with the average refractive-index change model²¹⁾, then analyzed how a temperature change induced a change in the refractive index and a change in the dimensions of volume hologram. For examples, Dhar et. al. estimated Bragg angle shift under the condition that out-of-plane thermal expansion of a photopolymer material is constrained due to two rigid glass substrates.²²⁾ Toishi et. al. expanded Dhar's model to 2D thermal expansion, and then analyzed how the temperature-induced distortions

deteriorated reproduced image on a camera.²³⁾ And Hoskins et. al. proposed a method for determining the needed change in wavelength for compensation of deteriorated reproduced holographic image based on Dhar's model.²⁴⁾

(c) Holographic disk tilt

As with the thermal expansion or contraction, holographic disk tilt induces Bragg mismatch. Incident angle of reference beam with respect to the holographic disk has to be controlled based on the tilt angle of the disk. Up until now, in order to suppress the Bragg mismatch, several servo control methods for keeping Bragg matching condition have been proposed.²⁵⁻²⁷⁾ By applying these methods to the HDSS, the effect of Bragg mismatch due to holographic disk tilt can be minimized.

(d) Wavefront aberration of reference beam

When wavefront aberration of reference beam during hologram readout is different from that during recording, the intensity profile of the reproduced holographic image deteriorates. At previous literatures, how to calculate the effect of wavefront aberrations have been discussed.²⁸⁻³¹⁾ And it has been analyzed what kind of aberration components have a great effect on the optical quality of the image through expanding wavefront aberrations to Zernike polynomial, then it was reported that COMA and spherical aberration more deteriorated the quality than astigmatism.³⁰⁾

Thus, analysis methods and measures for these deterioration factors have been widely discussed at previous literatures. However, discussion about other important factors such as polarization and vibration effects have not been sufficiently conducted. It is important for system design of holographic memory employing angularly multiplexed recording to take into these effect account, in particular when a high NA objective lens is used for high density recording.

1.1.4 Deterioration factors of holographic image to be discussed

(e) polarization effect

In HDSSs using angularly multiplexed recording using a high NA objective lens, the angular range of an incident angle of a signal beam with respect to the holographic medium widens. A wide angle between the

signal and reference beams generates holograms with quite a narrower pitch than the wavelength of the beams [Fig. 1.4]; thus, the polarization effect becomes apparent for readout of holograms.

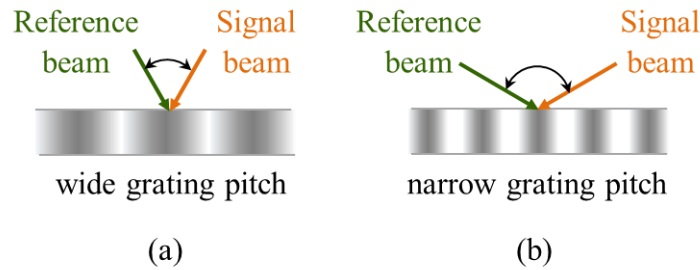


Fig. 1.4 Hologram pitch recorded by (a) narrow angle and (b) wide angle between signal and reference beams.

For example, an intensity gradient due to the polarization effect in a Bragg direction on a page data in an HDSS using a high NA of 0.6 has been discussed.³²⁾ The intensity gradient is apparent when a p-polarized reference beam is used for readout compared to when an s-polarized reference beam is used [Fig. 1.5]. Discussion regarding the polarization effect on an intensity profile remains in one direction on a page data³²⁾, but the effect on a 2D intensity profile over the entire area of the page data has not been discussed.

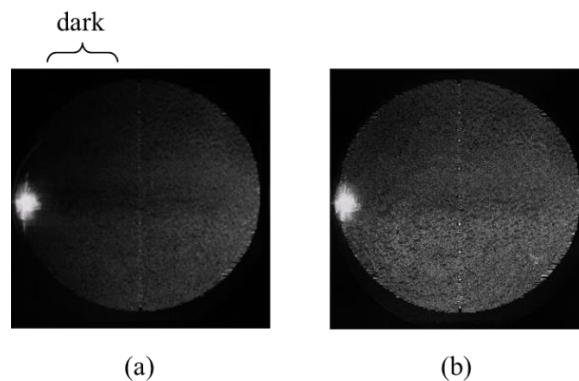


Fig. 1.5 reproduced holographic image with (a) p-polarized and (b) s-polarized reference beam.

When the polarization effect on an intensity profile over the entire area of a 2D page data is analyzed, optical analysis methods based on vector diffraction theory for light wave propagation in a volumetric hologram, such as Coupled Wave Theory³³⁾ (CWT), Rigorous Coupled Wave Analysis³⁴⁾ (RCWA) and Finite Difference Time Domain³⁵⁾ (FDTD), will become candidates because methods based on scalar diffraction theory do not take into the polarization effect account. However, FDTD is not suitable for HDSSs having 2D page data with a

couple of million pixels from the viewpoint of computational complexity because an area to be analyzed becomes on the order of square millimeters, which is significantly larger than the wavelength of a light wave in the system. Similarly, CWT and RCWA also require high computational complexity because they basically deal with only plane waves. In actual HDSSs, a reference beam contains wavefront aberration, and a spatially modulated signal beam is condensed using an objective lens. The aberrated reference beam and condensed signal beam should be decomposed into a large number of plane waves with different propagation angles for CWT and RCWA calculation. Something practical method that can calculate polarization effect with low computational complexity is required.

(f) vibration effect

Although “off-axis” optical configuration of angularly multiplexed recording contributes to improving high density recording because of their narrow Bragg selectivity, vibration tolerance of the configuration will be tighter than so-called “co-axis” configuration. The HDSS employing angular multiplexing generally implements a stop & go recording scheme⁸⁾ for stable recording and readout. In this scheme, the recording medium intermittently stays for recording or readout. The scheme is considered effective, as a first order, to eliminate the vibration effect due to mechanical instabilities while holograms are being recorded or reproduced. However, in practice, mechanical instabilities related to relaxation oscillation or residual oscillation caused by servomechanism more or less remain during recording and readout. Galvano mirror (Galvo) and spindle motor are typical mechanism controlled by servo in the system. Mechanical instability of mirror angle of Galvo induces oscillation of the incident angle of the reference beam and mechanical instability of rotation angle of spindle induces oscillation of the disk location. The vibration effect of these mechanical instability has not been discussed at previous literatures.

1.2 Research Aim and Objectives

In order to realize the holographic memory employing angularly multiplexed recording with high recording density which achieves comparable bit cost against Tape, the dissertation aims to explore the feasibility of the targeted recording density. For the purpose, the dissertation establishes an optical model which is capable to estimate the effect of deterioration factors on optical quality of a 2D reproduced holographic image in a practical way, in particular polarization and vibration effects, which have not been sufficiently discussed at

previous literatures. Then, major influence factors among the deterioration factors are clarified through numerical analysis using the established model and experiments. Moreover, a method of compensation for the factors is examined to acquire sufficient signal quality at the targeted high-density recording.

1.3 Structure of the Dissertation

The dissertation is organized into 6 Chapters as shown in Fig. 1.6. In Chapter 1, the research background, research aim and objectives was described. In Chapter 2, as one of important remaining issues toward realizing higher recording density which achieves comparable bit cost against Tape, the polarization effect on optical quality of reproduced holographic image is optically modeled. How the polarization state of reference and signal beams during recording and readout affects signal intensity profile on a camera over the entire area of the image is analytically formulated. Through the analytical formulation, adequate polarization state of reference and signal beams is clarified.

In Chapter 3, as another important remaining issue, the vibration effects of mechanical instability on optical quality of the reproduced holographic image is also optically modeled. Galvano-mirror and spindle motor, which are the main mechanical components incorporated into the system, are considered as vibration sources. Through the modeling of the effect, how mechanical instabilities affects intensity profile of the holographic image and degrades its signal quality are quantitatively analyzed. Then, the method to suppress the effect is discussed.

In Chapter 4, system noise at the targeted recording density of 1 [Tbit/in²] is estimated with taking into account various kinds of signal deterioration factors including polarization and vibration effects which are described in Chapter 2 and 3. Through the comparison of the system noise with required noise threshold for 1Tbit/in², noise improvement to be required is estimated. In Chapter 5, technique to achieve the required noise improvement is described. The technique compensates for the influence of disk de-track by controlling the position of a spatial filter according to the disk de-track; consequently, the optical quality of reproduced holographic image is improved. Again, system noise is compared with the required noise threshold under the condition that the technique is incorporated in the system. Then, the feasibility to achieve high density recording at 1Tbit/in² is verified.

Chapter 6 summarizes the research results of this paper and concludes the overall conclusion.

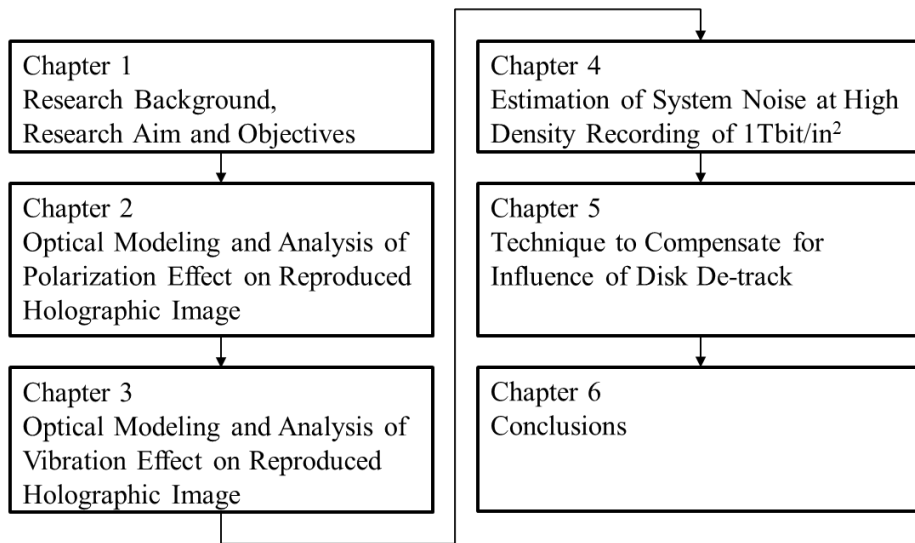


Fig. 1.6 Structure of the dissertation.

Chapter 2

Optical Modeling and Analysis of Polarization Effect on Reproduced Holographic Image

The polarization effect on signal intensity over the entire area of a 2D page data is analytically formulated, introducing an attenuation coefficient defined by the polarization state of reference and signal beams during recording and readout, by combining with optical analysis methods based on scalar diffraction theory. The proposed method is practical because the intensity profile can be calculated without using vector diffraction theory, such as CWT, RCWA and FDTD, which generally requires high computational complexity. The validity of the analytical formulation is discussed through comparison of experiments with numerical analysis. The formulation led to a new method of increasing signal intensity of the page data area deteriorated by the polarization effect and the effectiveness of the method is verified by numerical analysis.

2.1 Method

2.1.1 Mathematical formulation of polarization effect on amplitude of reproduced beam

First, a simple optical model of recording a Fourier transform hologram in which a reference plane wave interferes with a 2 dimensionally modulated signal beam is considered, as shown in Fig. 2.1(a). Each on-pixel on a spatial light modulator (SLM) corresponds to each signal plane wave with a different incident angle, such as $\vec{k}_{S_1}, \vec{k}_{S_2}, \dots, \vec{k}_{S_N}$, with respect to the holographic medium. Each pair of reference and signal plane waves produces each sinusoidal grating for the recording state. As many sinusoidal gratings as the decomposed signal plane waves are produced in the holographic medium. For the readout state, the reproduced beam diffracted from the medium is then considered an ensemble of each reproduced plane wave diffracted from those sinusoidal gratings, as shown in Fig. 2.1(b).

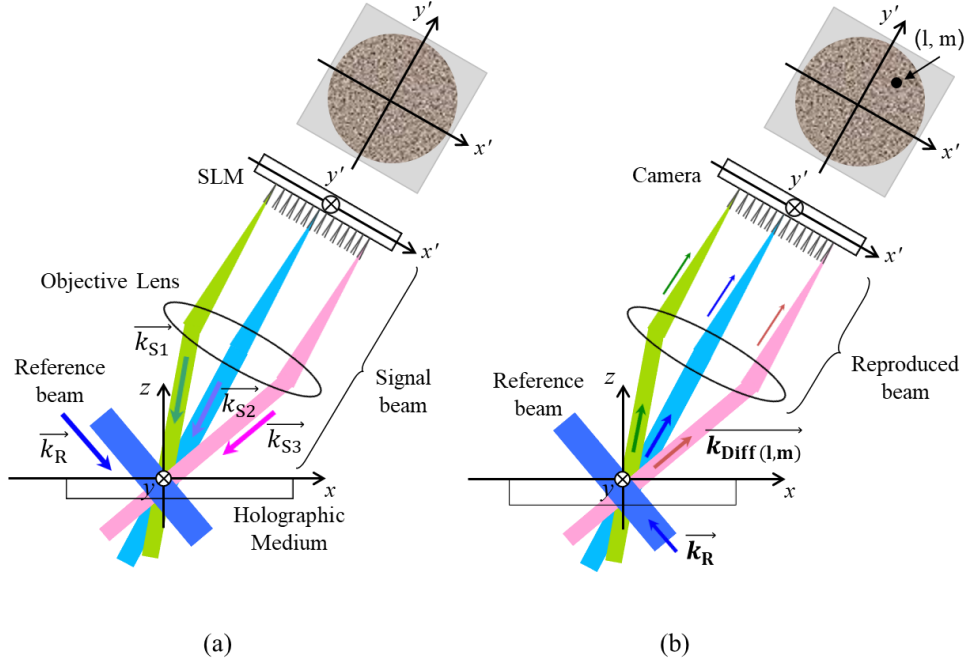


Fig. 2.1 Optical model of plane wave expansion during (a) recording and (b) readout.

According to CWT for a thick hologram of lossless dielectric grating whose amplitude of the spatial modulation is the index of refraction n_1 , the signal amplitude E_{Diff} of the reproduced plane wave diffracted from a sinusoidal grating is defined as

$$E_{\text{Diff}} = -j\nu \left(\frac{c_R}{c_S}\right)^{\frac{1}{2}} e^{-j\xi} \text{sinc}\sqrt{\nu^2 + \xi^2}, \quad (2.1)$$

$$\nu = \frac{\pi n_1 d}{\lambda \sqrt{c_R c_S}} (\vec{P}_{R_r} \cdot \vec{P}_D), \quad (2.2)$$

$$\xi = \vartheta d / 2c_S, \quad (2.3)$$

where λ is a wavelength, d is grating thickness, ϑ is a dephasing measure, c_R and c_S are obliquity factors of the reference and reproduced beams, respectively, “ \cdot ” is a dot product, and \vec{P}_{R_r} and \vec{P}_D are normalized polarization vectors of reference and reproduced beams during the readout state, respectively. When n_1 is quite small and Born approximation (BA) is applicable, the signal amplitude is redefined as

$$E_{\text{Diff}} = -j \frac{\pi n_1 d}{\lambda c_S} e^{-j\xi} \text{sinc}\xi (\vec{P}_{R_r} \cdot \vec{P}_D), \quad (2.4)$$

In order to examine that how small amplitude of the spatial modulation in index of refraction n_1 is necessary for proving the validity of Eq. (2.4), the optical model of hologram described in Fig. 2.2(a) was considered. Figure 2.2(b) shows the maximum relative error of diffraction efficiency (DE) calculated by Eq. (2.4) derived from BA against Eq. (2.1) derived from CWT as a function of n_1 when wavelength λ is 405 [nm], grating thickness d is 1.5 [mm], and average index of refraction n_0 is 1.5. When n_1 is 5×10^{-5} , the difference of DE between CWT and BA can be recognized [Fig. 2.2(b)]. However, when n_1 is 1×10^{-5} , the DE calculated by BA becomes same as that calculated by CWT and approximately 2 [%], then the maximum relative error of DE is less than 1 [%] and negligible. This result means Eq. (2.4) is applicable as long as n_1 is 1×10^{-5} or less, when λ is 405 [nm], d is 1.5 [mm] and n_0 is 1.5.

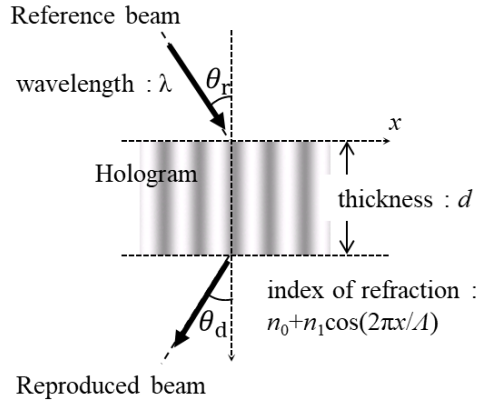
We then expand Eq. (2.4) to a two-dimensional expression. We introduce a pixel coordinate of (l, m) on a camera, as shown in Fig. 2.1(b), and a signal amplitude of the reproduced plane wave, which contributes to the intensity on (l, m) , is defined as $E_{\text{Diff}(l,m)}$. The parameters n_1 , c_S and $\overrightarrow{P_D}$ in Eq. (2.4) are dependent on (l, m) ; consequently, the signal amplitude $E_{\text{Diff}(l,m)}$ is written as

$$E_{\text{Diff}(l,m)} = -j \frac{\pi n_{1(l,m)} d}{\lambda c_{S(l,m)}} e^{-j\xi} \text{sinc}\xi(\overrightarrow{P_{R_r}} \cdot \overrightarrow{P_{D(l,m)}}), \quad (2.5)$$

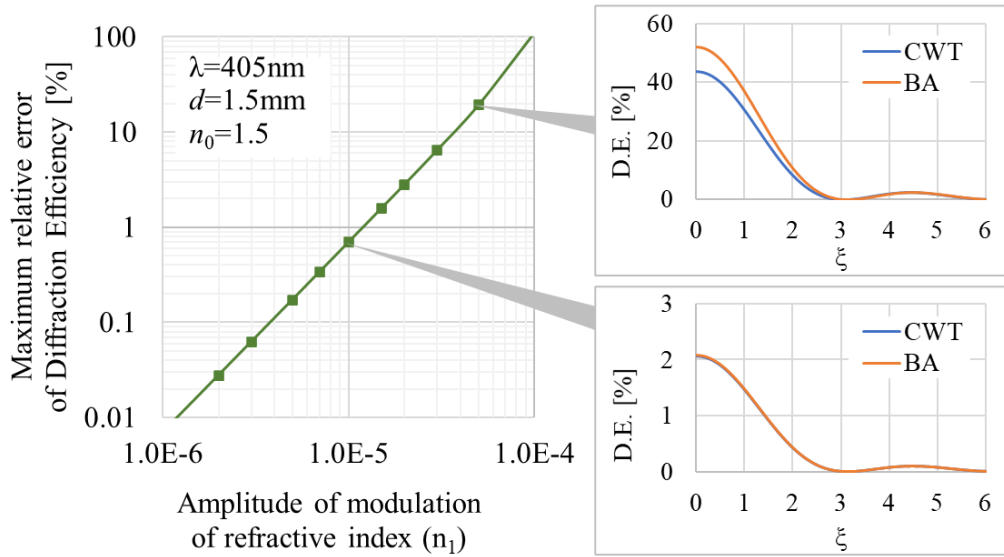
$$n_{1(l,m)} = n_1(\overrightarrow{P_{R_w}} \cdot \overrightarrow{P_{S(l,m)}}), \quad (2.6)$$

where $\overrightarrow{P_{R_w}}$ is the normalized polarization vector of the reference beam during recording, $\overrightarrow{P_{S(l,m)}}$ is the normalized polarization vector of the signal beam generated from the (l, m) on the SLM. By substituting Eq. (2.6) into Eq. (2.5), the signal amplitude can be expressed by separation of variables concerning the polarization effect,

$$\begin{aligned} E_{\text{Diff}(l,m)} &= -j \frac{\pi n_1 d}{\lambda c_{S(l,m)}} e^{-j\xi} \text{sinc}\xi(\overrightarrow{P_{R_w}} \cdot \overrightarrow{P_{S(l,m)}})(\overrightarrow{P_{R_r}} \cdot \overrightarrow{P_{D(l,m)}}) \\ &= E_{\text{NP}(l,m)}(\overrightarrow{P_{R_w}} \cdot \overrightarrow{P_{S(l,m)}})(\overrightarrow{P_{R_r}} \cdot \overrightarrow{P_{D(l,m)}}) \end{aligned} \quad (2.7)$$



(a)



(b)

Fig. 2.2 (a) Optical model of hologram and (b) graph of maximum relative error of diffraction efficiency as a function of amplitude of modulation of refractive index n_1 .

When a reference beam contains wavefront aberration, the aberrated reference beam is decomposed into many plane waves with different propagation angles. When the aberrated reference beam is decomposed into M 's plane waves, equation (2.7) can then be rewritten as

$$E_{\text{Diff}(l,m)} = \sum_{i=1}^M \{ E_{\text{NP}_i(l,m)} (\vec{P}_{R_w} \cdot \vec{P}_{S(l,m)}) (\vec{P}_{R_{r1}} \cdot \vec{P}_{D(l,m)}) \}, \quad (2.8)$$

We assume the wave front aberration is suppressed to some extent for the recorded hologram to be readable, which means the angular difference between incident angles of each decomposed reference plane wave and center of the incident angle of the aberrated reference beam θ_{R_0} is less than angular Bragg selectivity $\Delta\theta_B$,

$$\Delta\theta_B = \frac{\lambda \cos \theta_{S(l,m)}}{d \sin(\theta_{S(l,m)} + \theta_{R_0})}, \quad (2.9)$$

where $\theta_{S(l,m)}$ is an incident angle of the decomposed signal plane wave from the (l, m) on the SLM. When a hologram is thick ($d = 1.5$ mm) and λ is 405 nm, $\Delta\theta_B$ is approximately 0.02 degree, which is quite small value. Therefore, the third term on the right side of Eq. (2.8) is written as,

$$\overrightarrow{P_{R_r1}} \cdot \overrightarrow{P_{D(l,m)}} = \overrightarrow{P_{R_r0}} \cdot \overrightarrow{P_{D(l,m)}}, \quad (2.10)$$

where $\overrightarrow{P_{R_r0}}$ is a normalized polarization vector of the reference plane wave having the center of incident angle of the aberrated reference beam. Equation (2.8) can then be rewritten as

$$E_{\text{Diff}(l,m)} = \{\sum_i^M E_{\text{NP}_i(l,m)}\} (\overrightarrow{P_{R_w}} \cdot \overrightarrow{P_{S(l,m)}}) (\overrightarrow{P_{R_r0}} \cdot \overrightarrow{P_{D(l,m)}}) = \{\sum_i^M E_{\text{NP}_i(l,m)}\} A_w A_r \quad (2.11)$$

$$A_w = \overrightarrow{P_{R_w}} \cdot \overrightarrow{P_{S(l,m)}}, \quad (2.12)$$

$$A_r = \overrightarrow{P_{R_r0}} \cdot \overrightarrow{P_{D(l,m)}}, \quad (2.13)$$

Equation (2.11) indicates that the signal amplitude of a reproduced plane wave can be expressed in the form of multiplying a signal amplitude without the polarization effect by the attenuation coefficients A_w and A_r being dependent on the polarization state during recording and readout [Fig. 3]. The calculation is advantageous in terms of computational complexity because we no longer need to use vector diffraction theory such as CWT and RCWA. The first term on the right side in Eq. (2.11) can be calculated by using such as method, e.g., the Layer-by-Layer method³⁶⁻³⁸⁾ based on scalar diffraction theory. The A_w can be simply calculated by considering the optical architecture and polarization state of the reference and signal beams during recording. On the other hand, when we estimate A_r , we need to derive the normalized polarization vector of the reproduced beam $\overrightarrow{P_{D(l,m)}}$. The method of deriving the vector and estimating A_r is described in the next section.

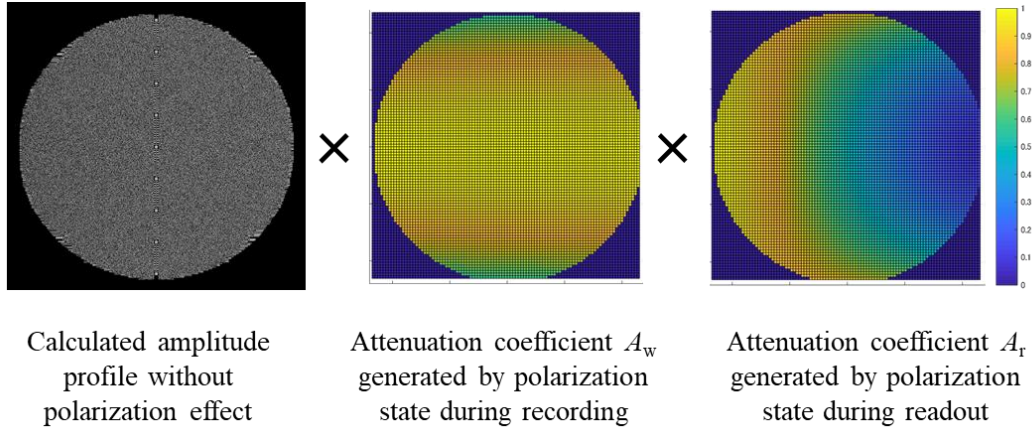


Fig. 2.3 Calculation of signal amplitude of reproduced holographic page data by taking polarization effect into account.

2.1.2 Method of deriving normalized polarization vector of reproduced beam

First, we define wave vectors of the reference plane wave as \vec{k}_R and reproduced plane wave, which contributes to intensity on (l, m) on the camera, as $\vec{k}_{D(l,m)}$. We then define an axis perpendicular to the plane containing \vec{k}_R and $\vec{k}_{D(l,m)}$ as the A_S -axis, axis perpendicular to the plane containing \vec{k}_R and A_S -axis as the A_{PR} -axis, and axis perpendicular to the plane containing A_S -axis and $\vec{k}_{D(l,m)}$ as the A_{PD} -axis, and $\theta_{RD(l,m)}$ is the angle between the A_{PR} and A_{PD} -axes, as shown in Fig. 2.4.

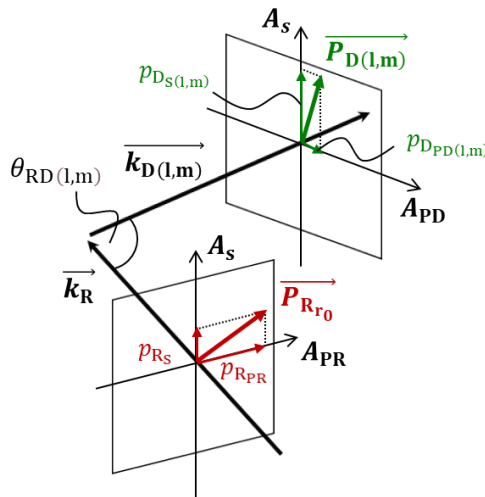


Fig. 2.4 Relationship between wave vectors and A_S -, A_{PR} - and A_{PD} -axes.

According to Eq. (2.4), the signal amplitude of reproduced plane wave is directly proportional to the inner product of two polarization vectors of reference and reproduced beams during the readout state. The A_{PD} -axis component of the signal amplitude of reproduced plane wave decreases by a factor of $\cos \theta_{RD(l,m)}$ due to the decrease in the coupling constant in CWT. Therefore, the A_S -axis component $p_{D_S(l,m)}$ and A_{PD} -axis component $p_{D_{PD}(l,m)}$ of the polarization vector of reproduced plane wave $\overrightarrow{P_{D(l,m)}}$ are written as

$$p_{D_S(l,m)} = cp_{R_S} \quad (2.14)$$

$$p_{D_{PD}(l,m)} = cp_{R_{PR}} \cos \theta_{RD(l,m)} \quad (2.15)$$

where p_{R_S} and $p_{R_{PR}}$ are the A_S -axis and A_{PR} -axis components of the polarization vector of reference plane wave $\overrightarrow{P_{R_0}}$ during readout, respectively, and c is a constant to regulate the magnitude of $\overrightarrow{P_{D(l,m)}}$ to be one because $\overrightarrow{P_{D(l,m)}}$ is normalized polarization vector,

$$(cp_{R_S})^2 + (cp_{R_{PR}} \cos \theta_{RD(l,m)})^2 = 1. \quad (2.16)$$

The constant c is written as

$$c = \frac{1}{\sqrt{p_{R_S}^2 + (p_{R_{PR}} \cos \theta_{RD(l,m)})^2}}. \quad (2.17)$$

By substituting Eq. (2.17) into (2.14) and (2.15), $p_{D_S(l,m)}$ and $p_{D_{PD}(l,m)}$ are rewritten as

$$p_{D_S(l,m)} = \frac{p_{R_S}}{\sqrt{p_{R_S}^2 + (p_{R_{PR}} \cos \theta_{RD(l,m)})^2}}, \quad (2.18)$$

$$p_{D_{PD}(l,m)} = \frac{p_{R_{PR}} \cos \theta_{RD(l,m)}}{\sqrt{p_{R_S}^2 + (p_{R_{PR}} \cos \theta_{RD(l,m)})^2}}, \quad (2.19)$$

$$\frac{p_{D_{PD}(l,m)}}{p_{R_{PR}}} = \frac{p_{D_S(l,m)}}{p_{R_S}} \cos \theta_{RD(l,m)}, \quad (2.20)$$

Consequently, A_r can be calculated using Eqs. (2.18) and (2.19),

$$A_r = \overrightarrow{P_{R_0}} \cdot \overrightarrow{P_{D(l,m)}} = \sqrt{p_{R_S}^2 + (p_{R_{PR}} \cos \theta_{RD(l,m)})^2}, \quad (2.21)$$

From the viewpoint of Fresnel equations, we can explain $\cos \theta_{\text{RD}(l,m)}$. The ratio of reflectance for p-polarized light r_p to reflectance for s-polarized light r_s is written as

$$\frac{r_p}{r_s} = \frac{\tan(\theta_i - \theta_j)/\tan(\theta_i + \theta_j)}{\sin(\theta_i - \theta_j)/\sin(\theta_i + \theta_j)} = \frac{\cos(\theta_i + \theta_j)}{\cos(\theta_i - \theta_j)}, \quad (2.22)$$

where θ_i is an incident angle, and θ_j is a refracted angle. When we consider hologram diffraction by applying the Fresnel equations, θ_i is equal to θ_j because a refracted beam is considered as the 0th order of the diffraction beam. Equation (2.22) is then rewritten as

$$r_p = \frac{\cos(\theta_i + \theta_j)}{\cos(\theta_i - \theta_j)} r_s = r_s \cos(\theta_i + \theta_j) = r_s \cos \theta_{\text{RD}}, \quad (2.23)$$

We can see that Eq. (2.23) indicates the same expression as Eq. (2.20).

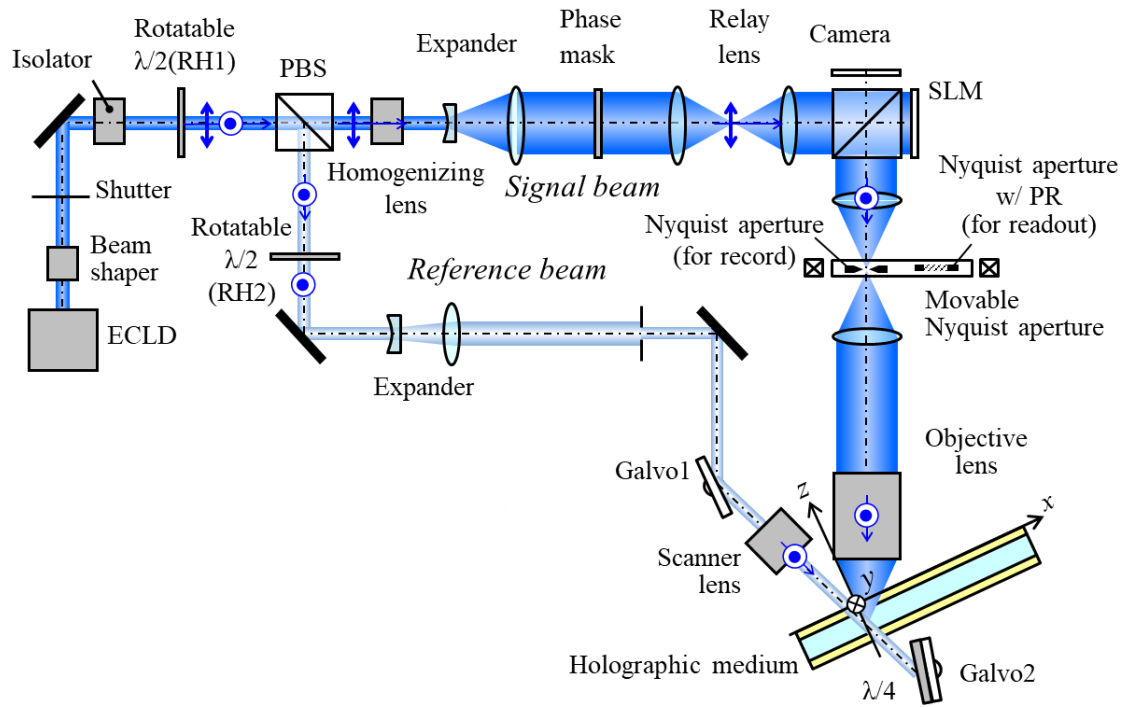
2.2 Experimental setup

To confirm the validity of the formulation described in Sect. 2.1, we conducted an experiment for observing the intensity profile of the reproduced holographic page data in an HDSS using an objective lens with an NA of 0.6 [Fig. 2.5].

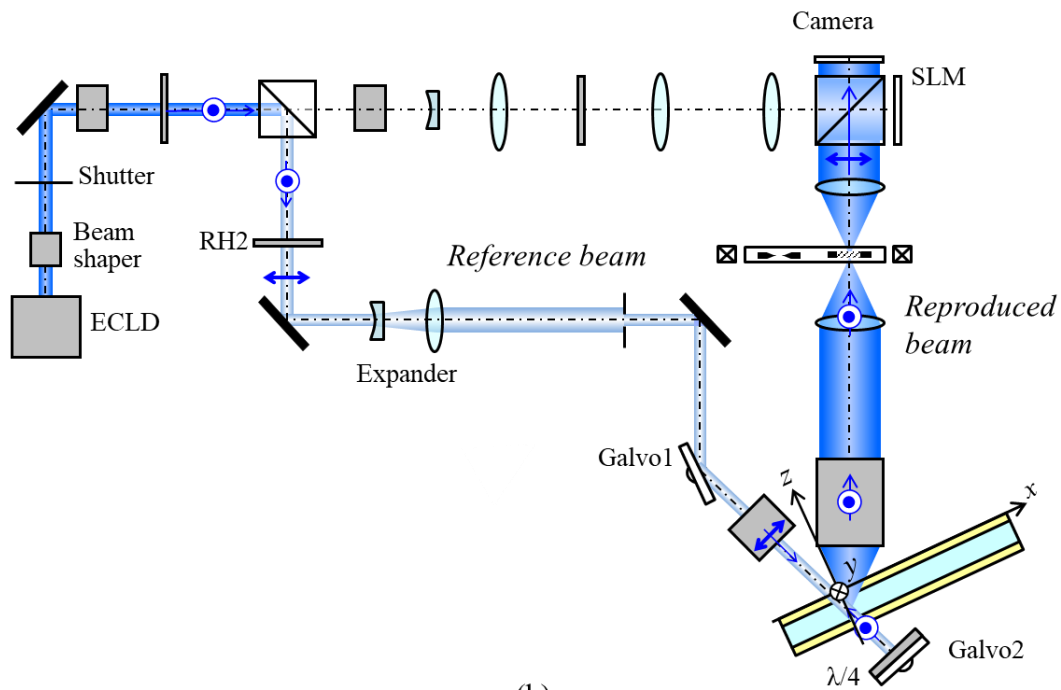
The experimental procedure is as follows. A laser beam from an external cavity laser diode (ECLD) is an elliptical collimated Gaussian beam. A beam shaper located just after ECLD expands the elliptical collimated beam in the minor axis direction and corrects it to a circular collimated beam. The circular collimated beam is divided into p-polarized and s-polarized beams by using a polarized beam splitter (PBS). The intensity ratio of the signal beam to the reference beam is controlled using a rotatable half-wave plate (RH1) in front of the PBS. When a hologram is recorded [Fig. 5(a)], the amplitude of the signal beam is spatially modulated using a phase mask and an encoded page data on a 2100 x 2100-pixel SLM with a 7.8- μm pixel pitch. The phase mask is incorporated into the signal beam path to make the intensity distribution in a holographic medium spatially uniform to prevent from locally consuming dynamic range of the holographic medium. The s-polarized signal beam travels through a relay lens. A movable Nyquist aperture, which consists of a Nyquist aperture for recording and a second Nyquist aperture for readout holograms, is placed in the Fourier plane of the relay lens. The s-polarized signal beam travels through the first Nyquist aperture, then the s-polarized signal beam is focused on a holographic medium by using an objective lens with a focal length of 12.4 mm. The incident angle of the s-polarized reference beam with respect to the holographic medium is controlled using a galvano

mirror (Galvo1). By interfering between the S-polarized reference and signal beams, a hologram is generated in the medium, which is a custom-made transparent disk with a 1.5-mm recording layer (photopolymer) sandwiched between two cover layers with antireflection coating.

When a hologram is reproduced [Fig. 2.5(b)], the direction of the linear polarization of the reference beam is rotated from the s- to p-polarized beam by using a rotatable half-wave plate (RH2). A second galvano mirror (Galvo2) with a quarter-wave plate ($\lambda/4$) is placed on the back side of the medium to retroreflect the reference beam and rotate the direction of linear polarization from p- to s-polarization for data recovery in a quasi-phase conjugate readout geometry. The s-polarized reproduced beam from the hologram travels through the same path as the signal beam, then passes through the second Nyquist aperture. A half-wave plate in the aperture rotates the direction of linear polarization of the reproduced beam from the s- to p-polarized beam. The p-polarized reproduced beam is imaged onto a 2816×2816 -pixel camera with a 5.8 [\mu m] pixel pitch, and the hologram image is reproduced by oversampling detection. Experimental parameters are summarized in Table I.



(a)



(b)

Fig. 2.5 Experimental setup and beam propagation during (a) recording and (b) readout.

Table I. Experimental parameters.

<i>ECLD</i>	Wavelength	405nm
<i>Optical axis with respect to medium</i>	Reference beam angle (in free space)	48°
	Signal beam (in free space)	-25°
<i>SLM</i>	Pixel pitch	7.8 μm
	Pixel number	2100 \times 2100
<i>Camera</i>	Pixel pitch	5.8 μm
	Pixel number	2816 \times 2816
<i>Objective lens</i>	Focal length	12.4 mm
	Numerical Aperture	0.6
<i>Medium</i>	Thickness of recording layer	1.5 mm
	Index of refraction	1.5

2.3 Results & Discussion

2.3.1 Numerical results of attenuation coefficients due to polarization effect

Figure 2.6 shows the calculated profile of the square of A_w superimposed onto a reproduced 2D page data [Fig. 2.6(a)] under the condition that the reference beam is p-polarized [Fig. 2.6(b)] and signal beam is polarized in the direction of the x' -axis [Fig. 2.6(c)]. In this numerical analysis, we calculated A_w within a larger NA range of the objective lens than that in the experiment to confirm how the coefficient changes as a function of NA . The outer edge of the analysis area corresponds to an NA of 0.95. A steep gradient in the direction of the x' -axis (Bragg direction) was observed.

Figure 2.7 shows calculated profile of the square of A_w [Fig. 2.7(a)] under the condition that the reference beam is s-polarized [Fig. 2.7(b)] and signal beam is polarized in the direction of the y' -axis [Fig. 2.7(c)]. The square of A_w in Fig. 2.7 was relatively larger than that in Fig. 2.6, and the steep gradient in the Bragg direction was not observed any more. Compared to the condition illustrated in Fig. 2.6, the condition illustrated in Fig. 2.7 was preferable for recording holograms. However, a slight decrease was observed in an area of high NA in the direction of the y' -axis (Bragg-degenerate direction) in Fig. 2.7(a).

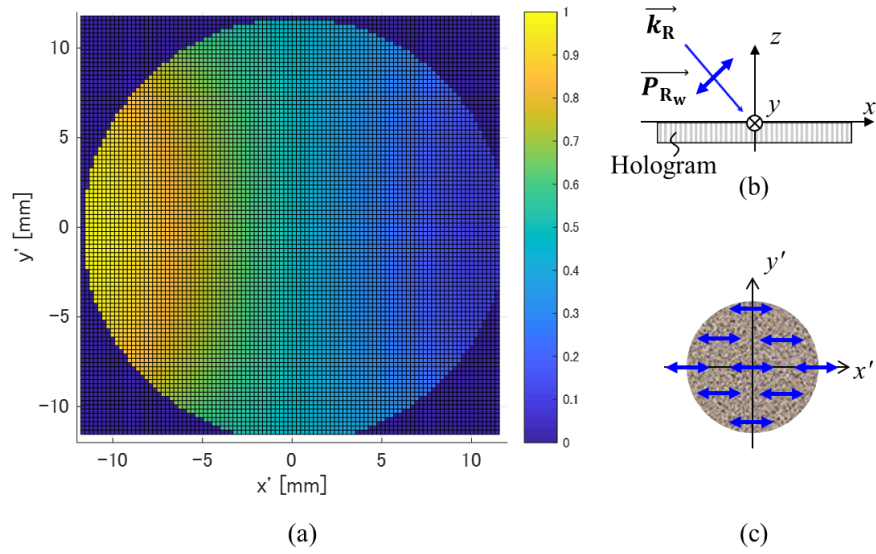


Fig. 2.6 (a) Simulated profile of $|A_w|^2$ superimposed onto a reproduced 2D page data on the condition that (b) reference beam is p-polarized and (c) signal beam is polarized in the direction of x' -axis.

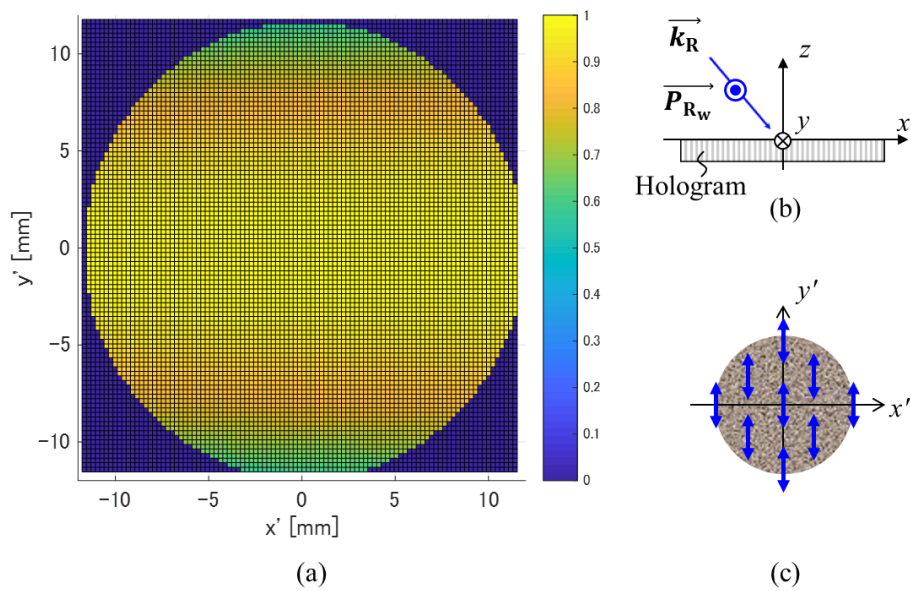


Fig. 2.7 (a) Simulated profile of $|A_w|^2$ superimposed onto reproduced 2D page data under condition that (b) reference beam is s-polarized and (c) signal beam is polarized in direction of y' -axis.

Figure 2.8 shows a graph of the decreasing A_w in the Bragg-degenerate direction as a function of NA under the condition illustrated in Fig. 2.7. We confirm that A_w becomes less than 0.9, which means the intensity of the reproduced beam decreases by around 20% when the y' coordinate exceeds an area corresponding to an NA of 0.6.

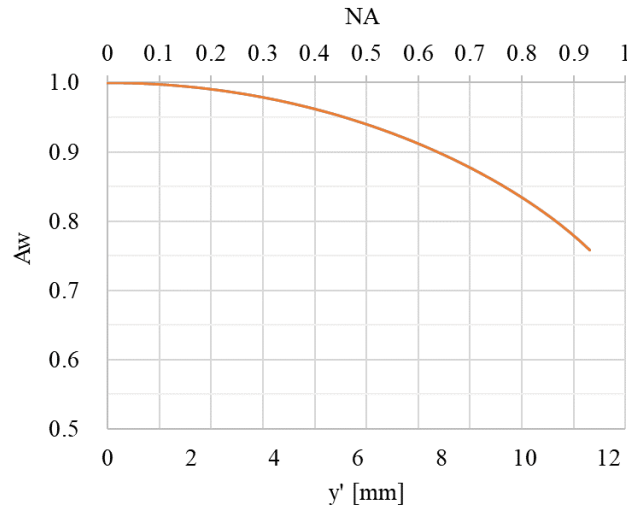


Fig. 2.8 Graph of cross section of A_w on y' -axis.

The reason why A_w decreases in an area of high NA is that the difference in the polarization direction between reference and signal plane waves is no longer negligible due to the refractive power of the objective lens. In other words, if we can control the polarization direction of signal plane waves in-plane direction during recording, we can suppress the decrease in A_w to some extent. The details of method of increasing the signal intensity are given in Section 2.4.3.

Figure 2.9 shows the calculated profile of the square of A_r superimposed onto a reproduced 2D page data [Fig. 2.9(a)] when the reference beam is p-polarized during readout [Fig. 2.9(b)]. As with the case of A_w , a steep gradient in the Bragg direction was observed. The degree of the gradient was dependent on the incident angle of reference beam θ_{ref} , as shown in Fig. 2.10. Figure 2.10 shows a graph of the cross section of the square of A_r along the direction of x' when y' is zero. As θ_{ref} increases, the gradient becomes steeper because the angle between the incident angle of reference beam and the diffraction angle of most of the decomposed reproduced plane waves get close to 90 [deg] in a holographic medium, then the condition of Brewster's angle is easy to be satisfied and the intensity of reproduced beam decreases remarkably.

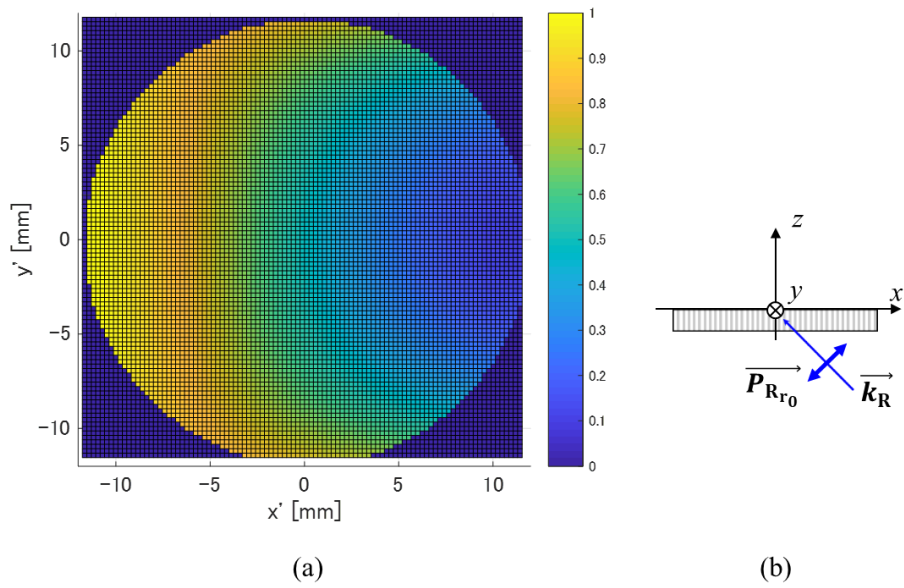


Fig. 2.9 (a) Simulated profile of $|A_r|^2$ superimposed onto reproduced 2D page data when (b) reference beam is p-polarized during readout.

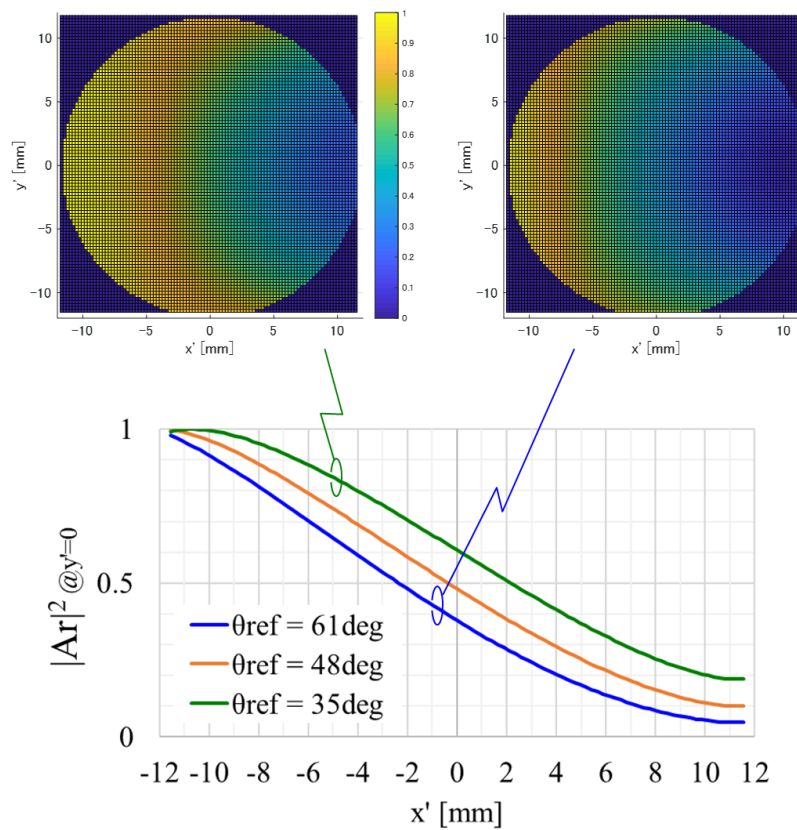


Fig. 2.10 Graph of cross section of $|A_r|^2$ on x' -axis.

Figure 2.11 shows the calculated profile of the square of A_r superimposed onto a reproduced 2D page data [Fig. 2.11(a)] when the reference beam is s-polarized during readout [Fig. 2.11(b)]. As with the case of A_w , s-polarized reference beam was preferable for readout holograms.

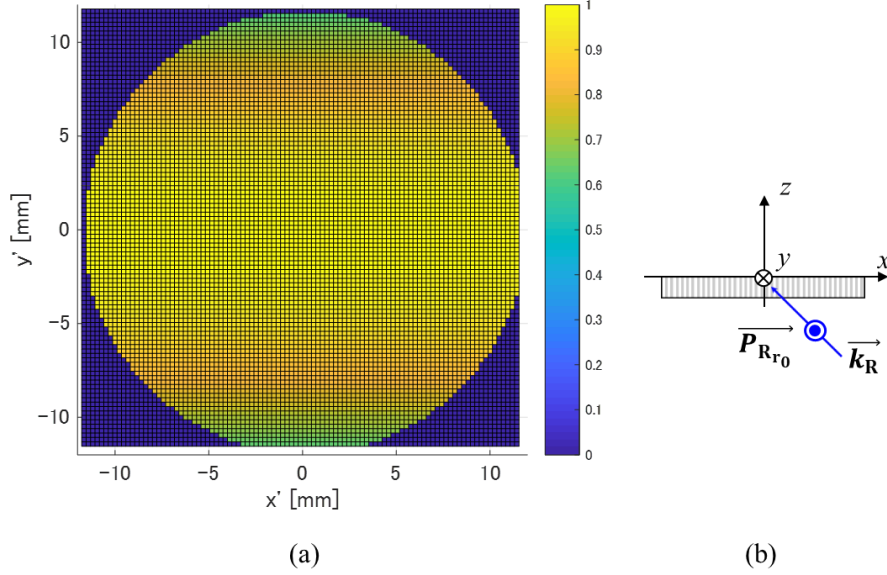


Fig. 2.11 (a) Simulated profile of $|A_r|^2$ superimposed onto reproduced 2D page data when (b) reference beam is s-polarized during readout.

Figure 2.12(a) and 2.12(c) show the simulated reproduced page data when the reference beam is p-polarized and s-polarized during readout, respectively. And Fig. 2.12(b) and 2.12(d) show the calculated Signal-to-Noise Ratio (SNR) map from the page data shown in Fig. 2.12(a) and 2.12(c), respectively. SNR is estimated as

$$SNR [dB] = 20 \log_{10}((\mu_{on} - \mu_{off})/(\sigma_{on} + \sigma_{off})) \quad (2.24)$$

where μ_{on} and μ_{off} are the mean values and σ_{on} and σ_{off} are the standard deviations of “on” and “off” of the reproduced binary digital signal, respectively. While p-polarized reference beam induces severe degradation of SNR, we confirmed a sufficient SNR when the reference beam was s-polarized.

Although s-polarized reference beam was preferable for readout holograms, a slight intensity decrease was observed in an area of high NA in the direction of the y' -axis (Bragg-degenerate direction). The intensity decrease was calculated by multiplying $|A_w|^2$ with $|A_r|^2$, then the decrease was about 30% in an area corresponding to NA of 0.6. The decrease of A_r is due to decrease in the coupling constant in CWT, as

discussed in Sect. 2.2.

From the clear difference in the profiles in Figs. 6(a) and 9(a), the polarization direction of the signal beam during recording $\overrightarrow{P_{S(l,m)}}$ is not conserved during readout, and moreover the polarization direction of the reproduced beam $\overrightarrow{P_{D(l,m)}}$ is independent from that of the signal beam $\overrightarrow{P_{S(l,m)}}$. That means a part of signal amplitude of reproduced beam will be blocked by the PBS in front of the camera in Fig. 2.5, then the signal intensity of the reproduced beam further decreases. Although the decrease in the coupling constant is inevitable, the decrease due to the PBS filtering is evitable by controlling the polarization direction of the reproduced beam in-plane direction during readout. The details of method of increasing the signal intensity are given in Section 2.4.3.

In conclusion, by taking the polarization state of reference, signal, and reproduced beams into account, we confirmed that the intensity profile of a reproduced 2D page data becomes inhomogeneous. In particular, a high- NA lens is likely to develop a markedly inhomogeneous intensity profile.

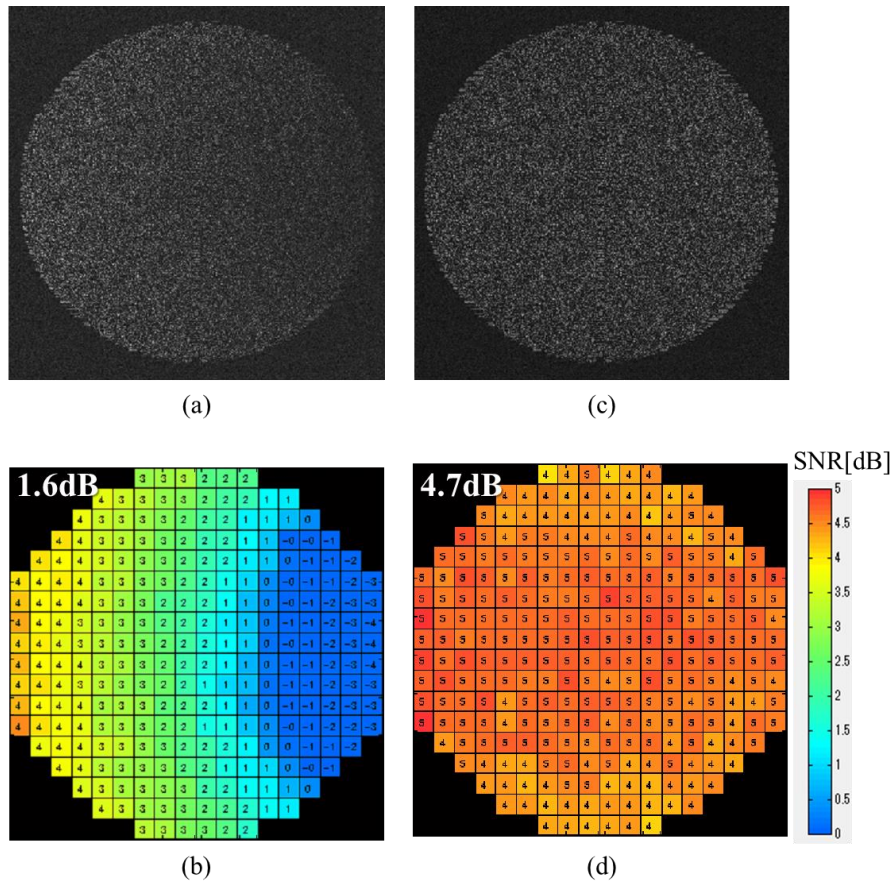


Fig. 2.12 (a) Simulated reproduced page data and (b) SNR map when reference beam is p-polarized, and (c) Simulated reproduced page data and (d) SNR map when reference beam is s-polarized during readout.

2.3.2 Verification of method of estimating attenuation coefficients

Figure 2.13 shows images of a (a) signal page data just after being reflected with the SLM in during recording and reproduced holographic page data on the camera in the experiment described in Sect. 2.2 by using (b) p-polarized and (c) s-polarized reference beams. The hot spot at the right edge in both images in Figs. 2.13(b) and 2.13(c) was caused by the surface reflection of the reference beam at the medium.

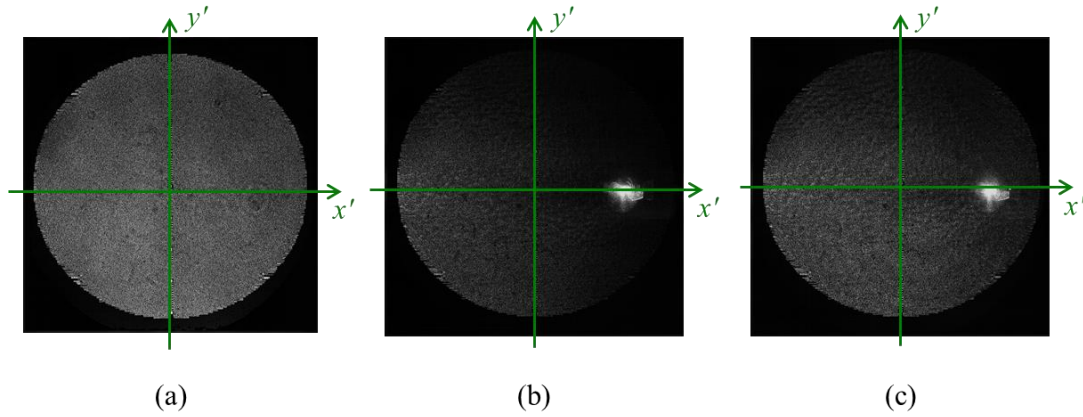


Fig. 2.13 Images of (a) signal page data just after being reflected by SLM and (b) holographic page data on camera reproduced by using p-polarized and (c) s-polarized reference beams.

Figure 2.14 shows a graph of the cross section of the intensity profile along the (a) direction of the x' -axis and (b) direction of the y' -axis of the experimental results shown in Fig. 2.13. The vertical axis shows the ratio of the intensity reproduced by the p-polarized reference beam to that by the s-polarized reference beam. The reason we use the ratio as an indicator is to remove the effect of angle dependence of transmittance of a holographic medium and fluctuation in the intensity profile of the signal beam during recording.³²⁾ There are two simulated profile in the graph. One is a simulated profile calculated using the analytical formulation described in Sect. 2.2, and the other is a simulated profile calculated using conventional RCWA. In the graph, we have removed the intensity of the hot spot from the experimental intensity profile to make it easier to compare the simulation with the experimental results. These two simulated results were in good agreement with the experimental results in both x' - and y' -axis directions. Through this comparison, we confirmed the analytical formulation described in Sect. 2.1 is valid.

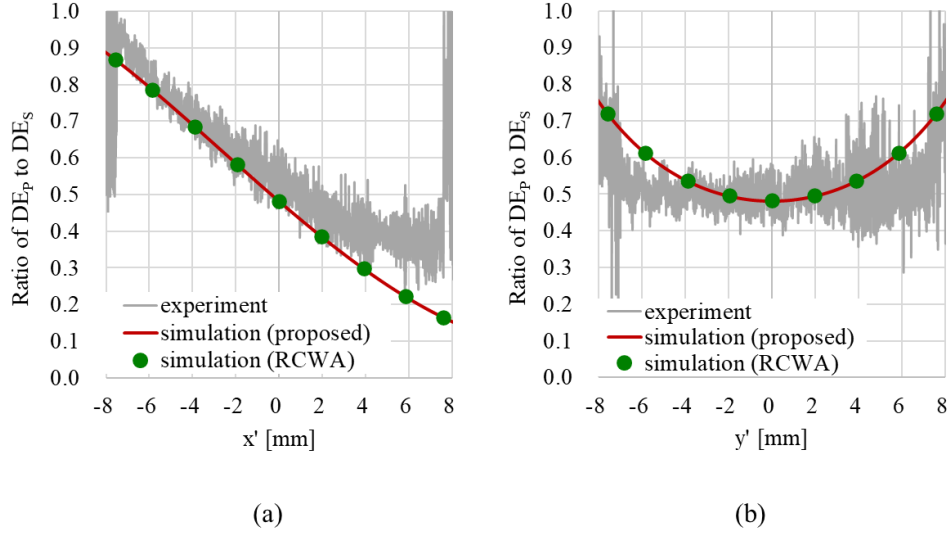


Fig. 2.14 Graph of signal intensity of experimental and simulation results on (a) x' -axis and (b) y' -axis.

2.3.3 Method of suppressing polarization effect on intensity profile

Figure 2.15 shows the simulated angular difference $\Delta\theta$ between the y' -axis and polarization direction of the reproduced beam on the y' -axis at the back focal plane of the objective lens when the s-polarized reference beam is used during readout. As the y' coordinate becomes larger, $\Delta\theta$ increases. When the reproduced beam travels through the PBS placed in front of the camera illustrated in Fig. 2.5, only the amplitude component parallel to the y' -axis passes through the PBS. This means the amplitude multiplied by only $\cos\Delta\theta$ passes through the PBS and contributes to signal intensity; however, the amplitude multiplied by $\sin\Delta\theta$ is blocked by the PBS.

Therefore, we developed a method of suppressing this intensity decrease by applying an optical filter such as an area division retarder [Fig. 2.16(a)] which controls the polarization direction of the reproduced beam in-plane direction and sets $\Delta\theta$ to zero [Fig. 2.16(b)].

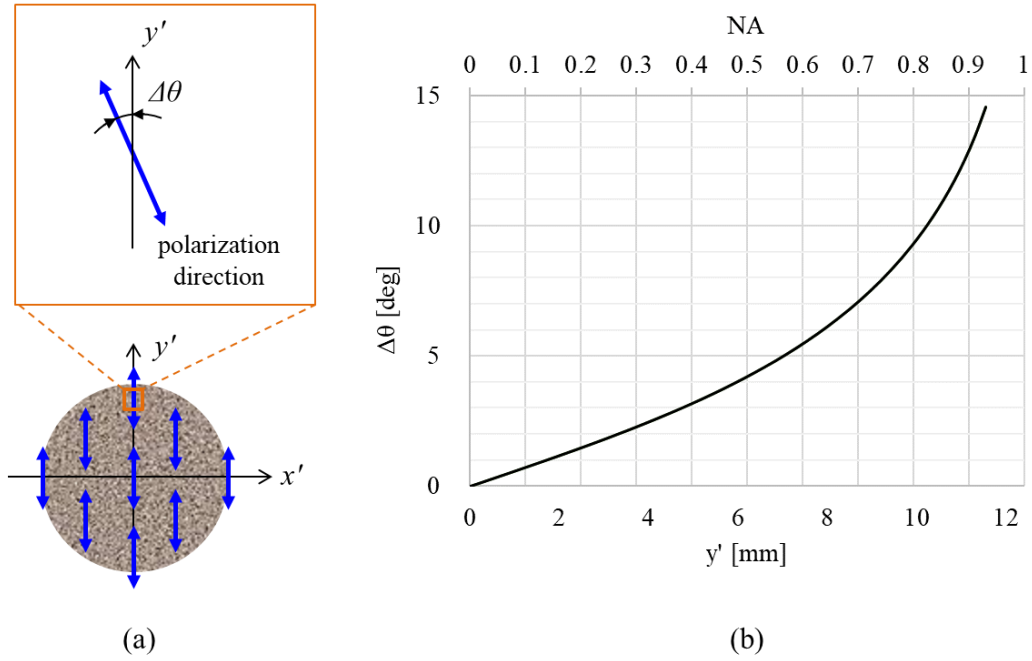


Fig. 2.15 (a) Definition of angular difference $\Delta\theta$ and (b) graph of simulated $\Delta\theta$ on y' -axis.

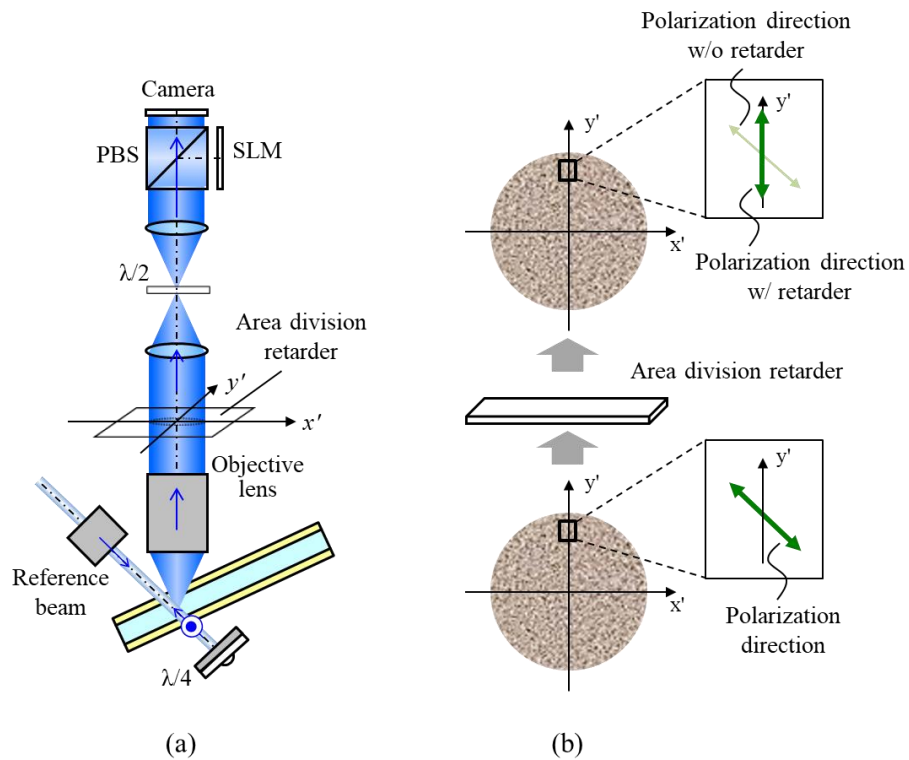


Fig. 2.16 (a) Optical architecture introduced area division retarder to suppress intensity decrease of reproduced signal and (b) change in polarization direction caused by the retarder.

Figure 2.17 shows the graph of the ratio of intensity increase on the camera as a function of the y' coordinate, when $\Delta\theta$ can be set to zero. The signal intensity at y' coordinate corresponding to an NA of 0.6 increases by about 2% by using the method. Moreover, the intensity at this coordinate corresponding to an NA of 0.9 increases by about 10%. As the NA of an objective lens becomes higher for a large capacity, the rate of intensity increase becomes larger.

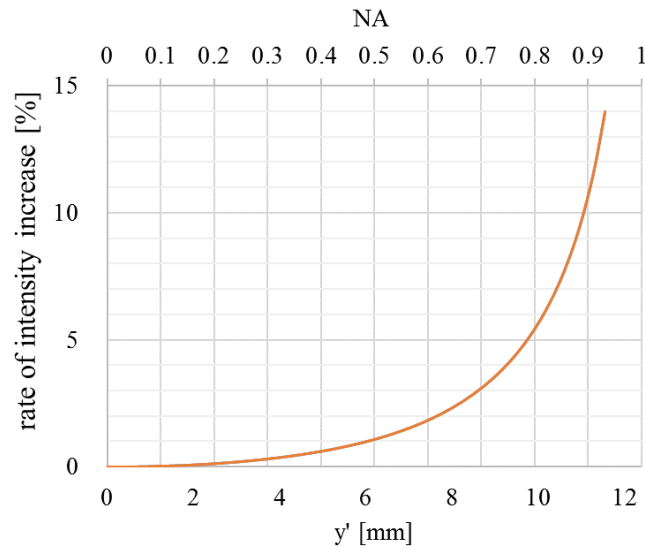


Fig. 2.17 Graph of rate of intensity increase on y' -axis.

2.4 Conclusions

The effect of polarization states of reference and signal beams during recording and readout on a signal amplitude of a reproduced holographic page data was analytically formulated. It was found that the amplitude can be expressed in the form of multiplying a signal amplitude calculated from scalar diffraction theory by attenuation coefficients dependent on the polarization states, when Born approximation is applicable. The validity of the formulation was confirmed through the comparison of experimental results with numerical analysis. By using the analytical formulation, the polarization effect on an intensity profile over the entire area of the page data was clarified without calculation using vector diffraction theory which requires high computational complexity. Through the experiments and the numerical analysis, it was found that s-polarized reference beam was suitable for achieving a uniform intensity profile of the page data. However, even when the reference beam was s-polarized, we observed the intensity decreased by about 30% in an area corresponding to NA of 0.6 in the Bragg-degenerate direction. As the NA of an objective lens becomes higher

for a large capacity, the rate of the intensity decrease becomes larger.

Then, we developed the method of suppressing the intensity decrease by applying an area division retarder which controls the polarization direction of the signal and reproduced beams in-plane direction. The intensity at the coordinate corresponding to an NA of 0.9 in the Bragg-degenerate direction increases by about 10% by using the method. Although the improvement was verified through only simulation, the simulation results indicates that it is highly feasible to improve a signal intensity profile in an HDSS with a high NA objective lens for achieving large data capacity.

Chapter 3

Optical Modeling and Analysis of Vibration Effect on Reproduced Holographic Image

This Chapter focuses on the vibration effect due to mechanical instabilities. As described in Chapter 1, mechanical instability of mirror angle of Galvo induces oscillation of the incident angle of the reference beam and mechanical instability of rotation angle of spindle induces oscillation of the disk location. How these mechanical instabilities affect the performance of HDSS is a subject of this Chapter. In particular, this Chapter deals with these instabilities occurring during recording state rather than during readout state. A hologram recorded under these instabilities consists of the ensemble of the fringes corresponding to each oscillating state during recording state. When such a hologram is reproduced, interference occurs between reproduced beams diffracted from each fringe. Due to the interference, a quality of reproduced image will be more deteriorated than that when the same mechanical instabilities occur during readout state. First of all, in order to analyze the effect of these mechanical instabilities on the HDSS quantitatively, the concept of time-averaged holography^{39,40)} is discussed. The concept is widely adopted in the field of holographic interferometry to measure vibrational characteristics of an object.

Next, how the concept is incorporated into the modeling of data recording and readout process for HDSS is discussed. Through the discussion and relating the mechanical parameters such as amplitude and frequency of mechanical oscillation to optical parameters such as amplitude and phase of reference and signal beams, the effect of mechanical instabilities of Galvo and the spindle motor on HDSS is numerically modeled. Then, the validity of the modeling is discussed through the comparison of experiments with numerical analysis. Furthermore, how to suppress the effect of mechanical instabilities on HDSS is discussed.

3.1 Mathematical formulation of mechanical instability effect on reproduced beam

3.1.1 Concept of time-average holography

Time-averaged holography^{39,40)} is one of methods among holographic interferometry which is widely used for such as vibration, structural, stress and strain analysis. The concept of the method is useful to interpret the characteristic of reproduced beam from a hologram recorded in mechanically unstable environment.

A fringe intensity profile in a holographic medium due to interference between reference and signal beams generates a spatial modulation in index of refraction in the medium. Assuming the spatial modulation Δn is proportional to the fringe intensity profile, Δn can be written by

$$\Delta n = \alpha(|R_w|^2 + |S_w|^2 + R_w^* S_w + R_w S_w^*), \quad (3.1)$$

where R_w and S_w are the complex amplitude of reference and signal beams during recording state in the medium, α is a constant of sensitivity of the medium to light, and the symbol “*” denotes complex conjugate. When a mechanical instability occurs during recording state, the instability induces alternation of complex amplitude of reference and/or signal beams. Consequently, Δn can be expressed by time average of the fringe intensity profile over recording exposure time t_r ,

$$\Delta n = \frac{\alpha}{t_r} \int_0^{t_r} (|R_w|^2 + |S_w|^2 + R_w^* S_w + R_w S_w^*) dt \quad (3.2)$$

The complex amplitude of reproduced beam E_p diffracted from the time average hologram is calculated by phase modulation of reference beam during readout state R_{r0} ,

$$E_p = \exp\left\{i \frac{2\pi d}{\lambda} (n_0 + \Delta n)\right\} R_{r0} = c_0 \exp\left(i \frac{2\pi d}{\lambda} \Delta n\right) R_{r0} \quad (3.3)$$

where n_0 is an average index of refraction in the medium, λ is a wavelength of R_{r0} , c_0 is a constant of complex value, and d is a thickness of the holographic medium. As long as the quantity, $2\pi d \Delta n / \lambda$ is sufficiently smaller than unity, Eq. (3.3) can be rewritten by using Taylor expansion up to the second term,

$$E_p = c_0 \left(1 + i \frac{2\pi d}{\lambda} \Delta n\right) R_{r0} \quad (3.4)$$

By substituting Eq. (3.2) into (3.4), the reproduced beam E_p can be expressed by following four terms,

$$\begin{aligned} E_p = c_0 & \left\{1 + i \frac{2\pi \alpha d}{\lambda} \left(\frac{1}{t_r} \int_0^{t_r} |R_w|^2 dt\right)\right\} R_{r0} + i \frac{2\pi \alpha c_0 d}{\lambda} \left(\frac{1}{t_r} \int_0^{t_r} |S_w|^2 dt\right) R_{r0} \\ & + i \frac{2\pi \alpha c_0 d}{\lambda} \left(\frac{1}{t_r} \int_0^{t_r} R_w^* S_w dt\right) R_{r0} + i \frac{2\pi \alpha c_0 d}{\lambda} \left(\frac{1}{t_r} \int_0^{t_r} R_w S_w^* dt\right) R_{r0} \end{aligned} \quad (3.5)$$

When a mechanical instability induces alternation of the complex amplitude of only signal beam S_w and R_{w0} is time-independent function, the reproduced beam E_p can be rewritten by

$$E_p = c_0 \left(1 + i \frac{2\pi\alpha d}{\lambda} |R_{w0}|^2 \right) R_{r0} + i \frac{2\pi\alpha c_0 d}{\lambda} \left(\frac{1}{t_r} \int_0^{t_r} |S_w|^2 dt \right) R_{r0} \\ + i \frac{2\pi\alpha c_0 d}{\lambda} R_{w0}^* \left(\frac{1}{t_r} \int_0^{t_r} S_w dt \right) R_{r0} + i \frac{2\pi\alpha c_0 d}{\lambda} R_{w0} \left(\frac{1}{t_r} \int_0^{t_r} S_w^* dt \right) R_{r0} \quad (3.6)$$

where R_{w0} is the complex amplitude of reference beam in a steady state. If the reference beams R_{w0} and R_{r0} are plane waves, the first term on the right-hand side of Eq. (3.6) represents an attenuated un-diffracted reproducing reference beam because the intensity of the reference beam $|R_{w0}|^2$ becomes uniform across the medium. The second term is a diffraction beam due to a hologram formed by mutual interference within the signal beam S_w . The third term represents a diffraction beam which has information on the signal beam S_w , while the fourth term is a diffraction beam which has information on the conjugate beam of the signal beam S_w^* . Among these four terms, the third term is detected by a camera.

$$E_p = i \frac{2\pi\alpha c_0 d}{\lambda} R_{w0}^* \left(\frac{1}{t_r} \int_0^{t_r} S_w dt \right) R_{r0} \quad (3.7)$$

The Eq. (3.7) is a general formulation of the complex amplitude of reproduced beam E_p from the time average hologram. For example, when the phase of S_w varies in a sinusoidal motion whose period is smaller than recording exposure time t_r , Eq. (3.7) can be rewritten by,

$$E_p = i \frac{2\pi\alpha c_0 d}{\lambda} R_{w0}^* S_w(x, y, z) \left\{ \frac{1}{t_r} \int_0^{t_r} \exp \left(i a_\omega \cos \frac{2\pi}{t_r} t \right) dt \right\} R_{r0} \\ = i \frac{2\pi\alpha c_0 d}{\lambda} R_{w0}^* S_w(x, y, z) J_0(a_\omega) R_{r0} \\ = E_{p0} \cdot J_0(a_\omega) \quad (3.8)$$

where E_{p0} is the complex amplitude of reproduced beam from hologram recorded in mechanically stable environment. The reproduced beam E_p from the time-average hologram is modulated by 0th order Bessel function of the first kind. These are interpretation of the concept of time-average holography. We incorporate the concept into the modeling of data recording and readout process for HDSS.

3.1.2 Incorporation of the concept of time-average holography into the modeling of HDSS

Generally, recorded holograms in HDSS are categorized into a thick hologram defined as $Q = 2\pi\lambda d/n\Lambda^2 \gg 1$ by Kogelnik.³³⁾ When a hologram is a thick hologram, phase modulation due to phase hologram can't be simply expressed by Eq. (3.3) anymore because this expression is valid for thin hologram. However, in the case of a thick hologram, the expression becomes valid by dividing the thick hologram into plural thin layers and by considering Eq. (3.7) as the complex amplitude of reproduced beam from each thin layer, known as a Layer-by-Layer method³⁶⁻³⁸⁾. When the thick hologram is divided into N 's thin layers and the complex amplitude of reference and signal beams in the m^{th} layer are described by $R_{w0,m}$, $R_{r0,m}$ and $S_{w,m}$, respectively, the complex amplitude of reproduced beam from m^{th} layer $E_{P,m}$ can be expressed through Eq. (3.7) by

$$E_{P,m} = i \frac{2\pi\alpha c_0 d}{\lambda N} R_{w0,m} * \left(\frac{1}{t_r} \int_0^{t_r} S_{w,m} dt \right) R_{r0,m} \quad (3.9)$$

Reproduced beam E_P diffracted from the thick hologram can be calculated by summing up all of each reproduced beam from each thin layer $E_{P,m}$,

$$E_P = \sum_{m=1}^N E_{P,m} = i \frac{2\pi\alpha c_0 d}{\lambda N} R_{w0,m} * \sum_{m=1}^N \left(\frac{1}{t_r} \int_0^{t_r} S_{w,m} dt \right) R_{r0,m} \quad (3.10)$$

Similarly, when a mechanical instability induces alternation of the complex amplitude of only reference beam, the reproduced beam E_P can be derived through the same procedure as the above and expressed by

$$E_P = \sum_{m=1}^N E_{P,m} = i \frac{2\pi\alpha c_0 d}{\lambda N} \sum_{m=1}^N \left(\frac{1}{t_r} \int_0^{t_r} R_{w,m} * dt \right) S_{w0,m} R_{r0,m} \quad (3.11)$$

Then, when a mechanical instability induces alternation of the complex amplitude of both reference and signal beams, the reproduced beam E_P can be expressed by,

$$E_P = \sum_{m=1}^N E_{P,m} = i \frac{2\pi\alpha c_0 d}{\lambda N} \sum_{m=1}^N \left(\frac{1}{t_r} \int_0^{t_r} R_{w,m}^* S_{w,m} dt \right) R_{r0,m} \quad (3.12)$$

Finally, when hologram is recorded in mechanically stable environment, the reproduced beam from the hologram is defined as E_{P0} in this paper and can be simply expressed by

$$E_{P0} = i \frac{2\pi\alpha c_0 d}{\lambda N} \sum_{m=1}^N R_{w0,m}^* S_{w0,m} R_{r0,m} \quad (3.13)$$

Thus, the concept of time-average holography was incorporated into the modeling of data recording and readout process for HDSS via the Layer-by-Layer³⁶⁻³⁸⁾ modeling approach.

3.1.3 Oscillation effect of reference beam angle on reproduced beam

In the section, mechanical instability effects on reproduced beam in specific cases are discussed. In angularly multiplexed recording, dynamic behavior of mirror angle of Galvo during recording state is a crucial factor in terms of recording hologram of good quality. Mechanical instability of mirror angle of Galvo induces oscillation of reference beam angle $\Delta\theta$ [Fig. 3.1]. How the oscillation of reference beam angle $\Delta\theta$ affects reproduced beam is examined in this section.

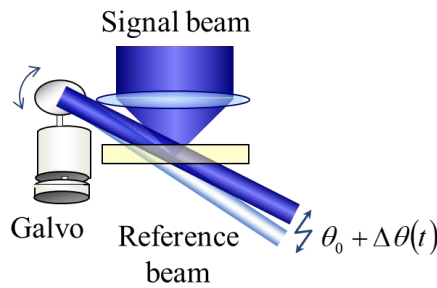


Fig. 3.1 Schematic diagram of oscillation of the reference beam angle due to the the instability of the mirror angle of Galvo.

When reference beam is considered as a plane wave whose DC component of incident angle with respect to a holographic medium is θ_0 , the complex amplitude of reference beam in the medium can be expressed by

$$R_w = A \exp \left[i \frac{2\pi}{\lambda} \left\{ \sin(\theta_0 + \Delta\theta) x + \sqrt{n_0^2 - \sin^2(\theta_0 + \Delta\theta)} z \right\} \right] \quad (3.14)$$

where the z-axis is chosen perpendicular to the surface of the holographic medium, the x-axis parallel to the medium. The x-z plane is the plane of incidence of reference beam. Under the condition that $\Delta\theta$ is a small

oscillation and of the order of sub-degree, we can consider $\cos \Delta\theta = 1$, $\sin \Delta\theta = \Delta\theta$ and neglect $\Delta\theta^2$ or higher terms. As a result, Eq. (3.14) can be rewritten by

$$\begin{aligned}
R_w &= A \exp \left[i \frac{2\pi}{\lambda} \left\{ (\sin\theta_0 + \cos\theta_0 \Delta\theta) x + z \sqrt{n_0^2 - \sin^2\theta_0 - 2\sin\theta_0 \cos\theta_0 \Delta\theta} \right\} \right] \\
&= A \exp \left[i \frac{2\pi}{\lambda} \left\{ (\sin\theta_0 + \cos\theta_0 \Delta\theta) x + z \sqrt{n_0^2 - \sin^2\theta_0} \sqrt{1 - \frac{2\cos\theta_0 \tan\theta_0'}{n_0 \cos\theta_0'} \Delta\theta} \right\} \right] \\
&= A \exp \left\{ i \frac{2\pi}{\lambda} \left(\sin\theta_0 x + z \sqrt{n_0^2 - \sin^2\theta_0} \right) \right\} \exp \left\{ i \frac{2\pi}{\lambda} \cos\theta_0 (x - z \tan\theta_0') \Delta\theta \right\} \quad (3.15)
\end{aligned}$$

where θ_0' is the internal angle of θ_0 inside the medium. The first exponential term in Eq. (3.15) denotes the plane wave without oscillation whose incident angle is θ_0 . The term in m^{th} layer ($z = z_m$) is expressed by $R_{w0,m}$ in the following,

$$R_{w0,m} = A \exp \left\{ i \frac{2\pi}{\lambda} \left(\sin\theta_0 x + z_m \sqrt{n_0^2 - \sin^2\theta_0} \right) \right\} \quad (3.16)$$

By substituting Eq. (3.15) and (3.16) into (3.11), the complex amplitude of reproduced beam E_P can be rewritten by

$$E_P = i \frac{2\pi \alpha c_0 d}{\lambda N} \sum_{m=1}^N \left[R_{w0,m} \frac{1}{t_r} \int_0^{t_r} \exp \left\{ i \frac{2\pi}{\lambda} \cos\theta_0 (x - z_m \tan\theta_0') \Delta\theta \right\} dt \right]^* S_{w0,m} R_{r0,m} \quad (3.17)$$

This is the mathematical formulation which indicates oscillation effect of reference beam angle on reproduced beam. Here, we define new parameter $f_{wf,m}$ as a weighting factor which indicates an oscillation effect due to oscillation of reference beam angle.

$$f_{wf,m} = \frac{1}{t_r} \int_0^{t_r} \exp \left\{ i \frac{2\pi}{\lambda} \cos\theta_0 (x - z_m \tan\theta_0') \Delta\theta \right\} dt \quad (3.18)$$

When there is no oscillation in incident angle ($\Delta\theta = 0$), the weighting factor becomes “1” as evidenced by the integral in Eq. (3.18). By comparing Eq. (3.17) to (3.13), the oscillation effect can be optically interpreted as if an optical filter whose transmittance is $f_{wf,m}$ is simply applied to the original reference beam $R_{w0,m}$. In other words, the reproduced beam affected by the oscillation can be numerically analyzed by replacing $R_{w0,m}$ with the following $R_{w0,m}'$,

$$R_{w0,m'} = R_{w0,m} f_{wf,m} \quad (3.19)$$

For example, when $\Delta\theta$ is a simple harmonic oscillation,

$$\Delta\theta = \frac{a_w}{2} \cos \frac{2\pi}{t_r} t \quad (3.20)$$

the weighting factor $f_{wf,m}$ can be solved analytically and the solution is the 0th order Bessel function of the first kind,

$$f_{wf,m} = J_0 \left(\frac{\pi}{\lambda} \cos\theta_0 (x - z_m \tan\theta_0') a_w \right) \quad (3.21)$$

Thus, the oscillation effect of reference beam angle on reproduced beam due to mechanical instability of Galvo can be formulated. The oscillation profile for this optical model is not limited to a simple harmonic oscillation. By calculating the weighting factor $f_{wf,m}$ analytically or numerically, arbitral oscillation profile of the reference beam angle can be incorporated into the model.

3.1.4 Oscillation effect of holographic disk location on reproduced beam

Mechanical instability of rotation angle of spindle $\Delta\varphi$ [Fig. 3.2(a)] induces oscillation of holographic disk location with respect to an intended location Δx [Fig. 3.2(b)]. How the oscillation of the disk displacement affects reproduced beam is discussed in this section.

A numerical analysis for the effect of the oscillation in a sinusoidal motion has been reported using the concept of double exposure.⁴¹⁾ In the analysis, only two holograms recorded at zero velocity (i.e., at peak state in a sinusoidal motion) are considered to contribute to reproduced beam. Holograms recorded at transient state between peaks in a sinusoidal motion are now taken into account by using the concept of time-averaged holography discussed in Sect. 3.2.1. Therefore, more rigorous analysis for the oscillation effect of disk displacement will be possible.

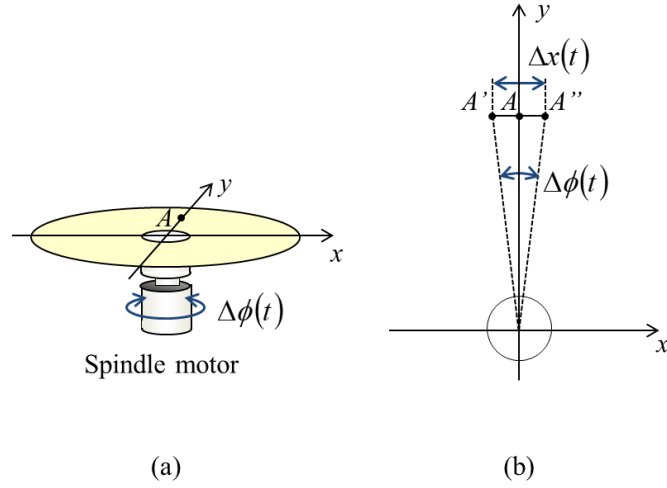


Fig. 3.2 Schematic diagram of (a) the instability of the spindle motor and (b) holographic disk displacement due to the instability of spindle motor.

When the oscillation of disk location Δx during recording state is viewed in relative way, the situation can be interpreted as an oscillatory shift of amplitude patterns of both the reference and signal beams on the surface of the medium. Once the situation is interpreted as such an alternation of the complex amplitude of both reference and signal beams, the reproduced beam E_P from the hologram recorded under the situation can be expressed by Eq. (3.12). To further investigate the oscillatory shift effect, the complex amplitude of the reproduced beam on a camera E_{PCAM} is examined. When hologram is recorded as a Fourier transform hologram, E_{PCAM} can be calculated by Fourier transform of Eq. (3.12).

$$E_{PCAM} = \mathfrak{F}[E_P] = i \frac{2\pi a c_0 d}{\lambda N} \mathfrak{F} \left[\sum_{m=1}^N \left(\frac{1}{t_r} \int_0^{t_r} R_{w,m}(x + \Delta x(t), z_m)^* S_{w,m}(x + \Delta x(t), y, z_m) dt \right) R_{r0,m}(x, z_m) \right] \quad (3.22)$$

where $R_{w,m}$ and $R_{r0,m}$ are plane waves as below,

$$R_{w,m} = A \exp \left[i \frac{2\pi}{\lambda} \left\{ \sin \theta_0 (x + \Delta x(t)) + \sqrt{n_0^2 - \sin^2 \theta_0} z_m \right\} \right] \quad (3.23)$$

$$R_{r0,m} = A \exp \left\{ i \frac{2\pi}{\lambda} \left(\sin \theta_0 x + \sqrt{n_0^2 - \sin^2 \theta_0} z_m \right) \right\} \quad (3.24)$$

If there is no oscillation during recording state, E_{PCAM} can be simply expressed by

$$E_{\text{PCAM}} = i \frac{2\pi\alpha c_0 d}{\lambda N} \mathfrak{F} \left[\sum_{m=1}^N R_{w0,m}^* S_{w0,m} R_{r0,m} \right] = E_{\text{PCAM},0} \quad (3.25)$$

First, the function $R_{r0,m}$ in Eq. (3.22) is included in the integral because the function is time-independent function.

$$E_{\text{PCAM}} = i \frac{2\pi\alpha c_0 d}{\lambda N} \mathfrak{F} \left[\sum_{m=1}^N \left(\frac{1}{t_r} \int_0^{t_r} R_{w,m}(x + \Delta x(t), z_m)^* S_{w,m}(x + \Delta x(t), y, z_m) R_{r0,m}(x, z_m) dt \right) \right] \quad (3.26)$$

Next, the order of integral operator and Fourier transform are transposed because Fourier transform is a linear transform,

$$E_{\text{PCAM}} = i \frac{2\pi\alpha c_0 d}{\lambda N} \frac{1}{t_r} \sum_{m=1}^N \int_0^{t_r} \left\{ \mathfrak{F} \left[R_{w,m}(x + \Delta x(t), z_m)^* S_{w,m}(x + \Delta x(t), y, z_m) R_{r0,m}(x, z_m) \right] \right\} dt \quad (3.27)$$

Then, $R_{r0,m}$ is modified as

$$R_{r0,m} = A \exp \left[i \frac{2\pi}{\lambda} \left\{ \sin\theta_0 (x + \Delta x(t)) + \sqrt{n_0^2 - \sin^2\theta_0} z_m \right\} \right] \exp \left\{ -i \frac{2\pi}{\lambda} \sin\theta_0 \Delta x(t) \right\} \quad (3.28)$$

By substituting Eq. (3.28) into (3.27) and Fourier Shift Theorem,

$$\mathfrak{F}[f(x + \Delta x)] = \mathfrak{F}[f(x)] \exp(i2\pi k_x \Delta x) \quad (3.29)$$

the complex amplitude E_{PCAM} can be rewritten by

$$\begin{aligned} E_{\text{PCAM}} &= E_{\text{PCAM},0} \frac{1}{t_r} \int_0^{t_r} \exp \left\{ i2\pi \left(k_x - \frac{\sin\theta_0}{\lambda} \right) \Delta x(t) \right\} dt \\ &= E_{\text{PCAM},0} g_{\text{wf}} \end{aligned} \quad (3.30)$$

$$g_{\text{wf}} = \frac{1}{t_r} \int_0^{t_r} \exp \left\{ i2\pi \left(k_x - \frac{\sin\theta_0}{\lambda} \right) \Delta x(t) \right\} dt \quad (3.31)$$

Here, k_x is a variable in Fourier domain and corresponds to a coordinate of position on the camera normalized by the wavelength times a focal length of Fourier transform lens which produces the Fourier transform

hologram.

As a result, the complex amplitude E_{PCAM} can be expressed by $E_{\text{PCAM},0}$ modulated by g_{wf} . This is the mathematical formulation which indicates oscillation effect of disk displacement on reproduced wave. For example, when Δx is a simple harmonic oscillation,

$$\Delta x = \frac{a_w}{2} \cos \frac{2\pi}{t_r} t \quad (3.32)$$

g_{wf} can be solved analytically and the solution is the 0th order Bessel function of the first kind,

$$g_{\text{wf}} = J_0 \left(\pi \left(k_x - \frac{\sin \theta_0}{\lambda} \right) a_w \right) \quad (3.33)$$

That is to say, the intensity distribution on a camera varies according to the square of the 0th order Bessel function of the first kind. Similar to the case described in Sect. 3.2.3, the oscillation profile for this optical model is not limited to a simple harmonic oscillation. As long as g_{wf} defined by Eq. (3.31) can be calculated, arbitral oscillation profile of the disk displacement can be incorporated into the model.

3.2 Optical compensation for mechanical instability effect

As previously stated, the oscillation effect of reference beam angle during recording is optically interpreted as an optical filter against reference beam and its transmittance is $f_{\text{wf},m}$ described in Eq. (3.18). Therefore, if the complex amplitude of reference beam can be modulated in advance by an optical filter whose transmittance is opposite characteristic of $f_{\text{wf},m}$, the oscillation effect can be compensated.^{42,43)}

For simplicity, we assume that an incident angle of reference beam oscillates in a simple harmonic oscillation. The oscillation effect on reproduced beam can be compensated by applying an optical filter whose transmittance is T_w to reference beam during recording state,

$$T_w = \frac{1}{f_{\text{wf},m}} = \frac{1}{J_0 \left(\frac{\pi}{\lambda} \cos \theta_0 (x - z_m \tan \theta_0) a_w \right)} \quad (3.34)$$

because the complex amplitude of reproduced beam becomes same as Eq. (3.13),

$$E_P = i \frac{2\pi\alpha c_0 d}{\lambda N} \sum_{m=1}^N (R_{w0,m} T_w f_{wf,m})^* S_{w0,m} R_{r0,m} = i \frac{2\pi\alpha c_0 d}{\lambda N} \sum_{m=1}^N R_{w0,m}^* S_{w0,m} R_{r0,m} \quad (3.35)$$

Similarly, the oscillation effect can be compensated by modulating the complex amplitude of reference beam during readout state because Eq. (3.17) can be rewritten by

$$E_P = i \frac{2\pi\alpha c_0 d}{\lambda N} \sum_{m=1}^N R_{w0,m}^* S_{w0,m} (R_{r0,m} f_{wf,m}^*) \quad (3.36)$$

By applying an optical filter whose transmittance T_r is opposite characteristic of complex conjugate of $f_{wf,m}$ to reference beam during reproducing state,

$$T_r = \left(\frac{1}{f_{wf,m}} \right)^* = \frac{1}{J_0 \left(\frac{\pi}{\lambda} \cos \theta_0 (x - z_m \tan \theta_0') a_w \right)} \quad (3.37)$$

the complex amplitude of reproduced beam also becomes same as Eq. (3.13).

$$E_P = i \frac{2\pi\alpha c_0 d}{\lambda N} \sum_{m=1}^N R_{w0,m}^* S_{w0,m} (R_{r0,m} T_r f_{wf,m}^*) = i \frac{2\pi\alpha c_0 d}{\lambda N} \sum_{m=1}^N R_{w0,m}^* S_{w0,m} R_{r0,m} \quad (3.38)$$

Examples of required transmittance profile of the optical filter are shown in Figure 3.3. These profiles are calculated by using Eq. (3.37) at $a_w = 10$ [mdeg] [Fig. 3.3(a)] and at $a_w = 20$ [mdeg] [Fig. 3.3(b)], when θ_0 is 40 [deg], θ_0' is 25.4 [deg], z_m is 0 [μm] which indicates the middle of the holographic medium, and λ is 405 [nm]. The horizontal axes in these graphs denote the location corresponded to that in the medium in the x-axis. The vertical axes denote required transmittance at the location. By modulating amplitude and phase of reference beam appropriately as described in Fig. 3.3, the mechanical oscillation effect can be optically compensated. The region where the transmittance exceeds 100% means higher incident power than the original power which is originally set in the case of no oscillation is necessary for reference beam. Increasing incident power will be feasible to increase the output of light source during the compensation.

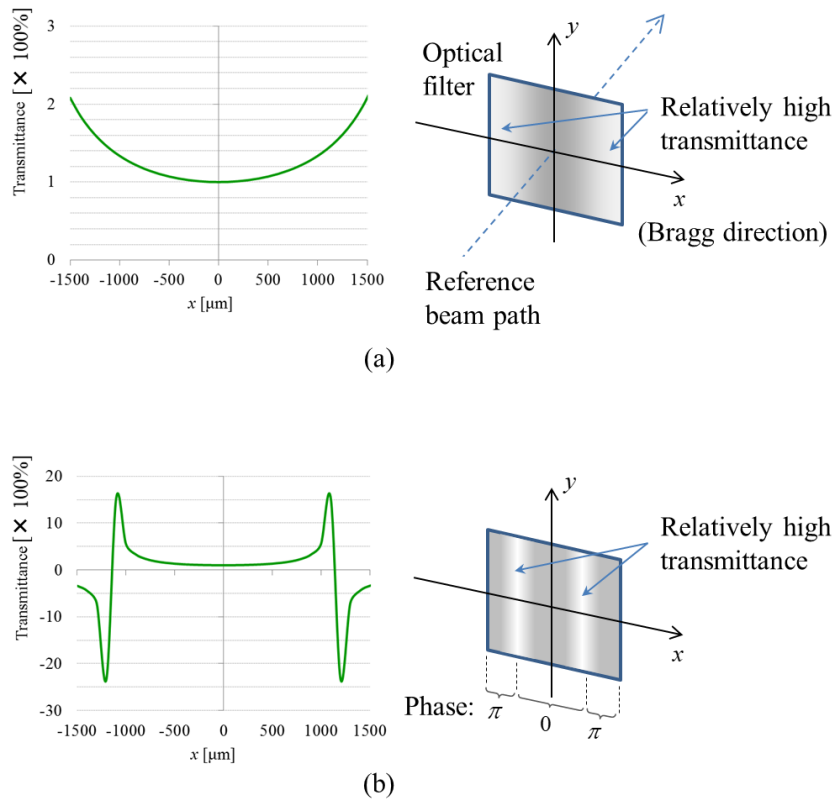


Fig. 3.3 Amplitude and phase profile of the proposed optical filter to compensate for mechanical vibration effect: (a) $a_w = 10$ mdeg, (b) $a_w = 20$ mdeg, when θ_0 is 40 deg and λ is 405 nm.

3.3 Results and Discussion

3.3.1 Validity of optical modeling of oscillation effect

In order to verify the validity of the optical modeling described in Sect. 3.2, an experiment for observing the oscillation effect of reference beam angle was conducted. The experimental setup for the verification is shown in Fig. 3.4. A laser beam from an External Cavity Laser Diode (ECLD) is divided into signal and reference beams by a Polarized Beam Splitter (PBS). The amplitude of the signal beam is spatially modulated using an encoded page data on a 576 x 1152 pixel SLM with an 8 μm pixel pitch. Incident angle of reference beam with respect to a holographic medium is controlled by galvano mirror (Galvo1). The objective lens is a custom lens whose focal length is 12.4 [mm]. Both of the signal and reference beams pass through the objective lens.⁴⁴⁻⁴⁷⁾ The focal point of the reference beam is at the back focal plane of the lens, resulting in a collimated reference beam at the holographic medium. The medium is a custom transparent disk with a 1.5 [mm] recording layer (photopolymer) sandwiched between a 0.1 [mm] first substrate and a 1.0 [mm] second substrate with anti-

reflection (AR) coating. A second galvano mirror (Galvo2) is placed on the back side of the medium to retro-reflect the reference beam for data recovery in a quasi-phase conjugate readout geometry. Recovered holograms are imaged using a 2000 x 2000 pixel camera with a 5.5 [μm] pixel pitch and the hologram image is reproduced by an oversampling detection. In the experiment, a disturbance signal was applied to Galvo1 during recording exposure time.

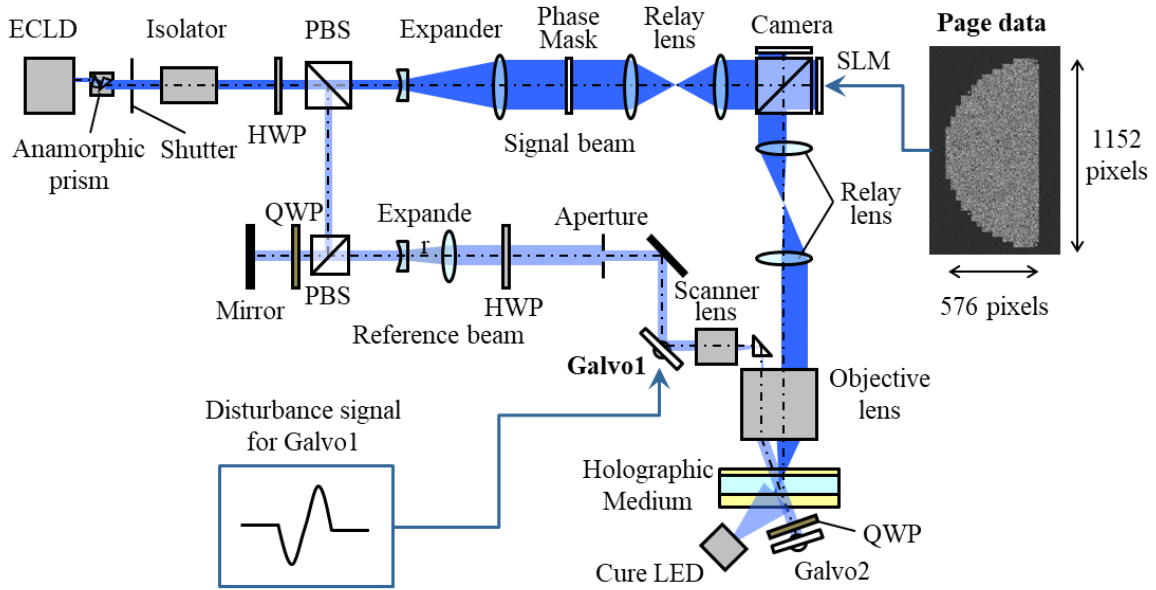


Fig. 3.4 Schematic diagram of the experimental setup.

The waveform of disturbance signal for Galvo1 is shown in Fig. 3.5. Due to a mechanical specification of the experimental setup, generation of disturbance signal was constrained to a step-wise waveform. Therefore, a step-wise sinusoidal signal was applied to Galvo1 for disturbance in the experiment [Fig. 3.5(a)]. Accordingly, in numerical analysis, the approximate step-wise signal was used for modeling oscillation of incident angle of reference beam [Fig. 3.5(b)].

The peak-to-valley of oscillation of reference beam angle is defined as a_w in both experiment and numerical analysis. The weighting factor $f_{wf,m}$ in Eq. (3.18) was calculated by using numerical integral of Simpson's law under the condition of the step-wise signal. Input parameters for numerical analysis are summarized in Table II. Each value of input parameter was assigned to correspond with specifications of the experimental setup.

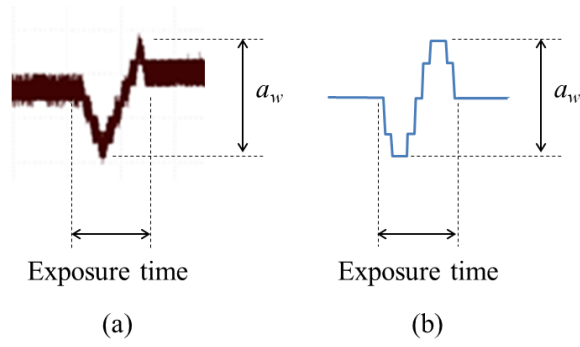


Fig. 3.5 Phase front form of disturbance signal for Galvo1 (a) in the experiment and (b) in numerical analysis.

Table II Input parameters for numerical analysis

<i>General</i>	Number of grid points	$N_x \times N_y$	8192×8192
<i>Optical beam</i>	Reference beam angle (in free space)	θ_0	40°
	Wavelength (in free space)	λ	405nm
<i>SLM</i>	Pixel pitch	Δ_{SLM}	$8.0\mu\text{m}$
	Oversampling rate	m_{SLM}	3
	Page format	$NN_x \times NN_y$	576×1152
<i>Camera</i>	Pixel pitch	Δ_{cam}	$5.5\mu\text{m}$
<i>Objective lens</i>	Focal length	f	12.4mm
<i>Medium</i>	Thickness of recording layer	d	$1500\mu\text{m}$
	Number of layers	N	10
	Index of refraction	n	1.5
<i>Spatial filter</i>	Aperture size	$\Delta_{spatial}$	$\times \sqrt{1.3}$ Nyquist

Reproduced images on the camera in both the experiment and numerical analysis are shown in Figure 3.6. When a change tendency of brightness distribution in these images was focused on, both results showed same tendency such that the left side of the image is relatively darker than other regions, as the magnitude of the oscillation increased.

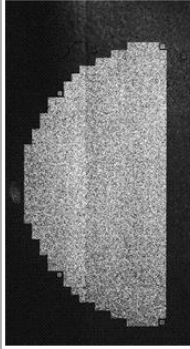
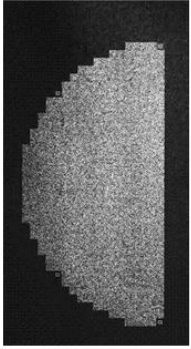
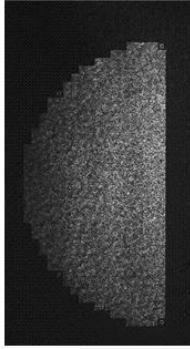
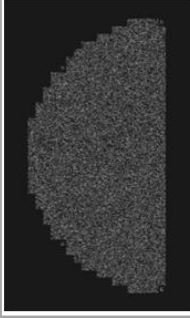
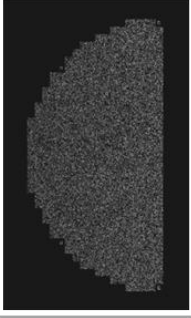
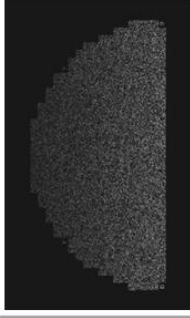
	$\alpha_w = 5\text{mdeg}$	$\alpha_w = 30\text{mdeg}$	$\alpha_w = 60\text{mdeg}$
Experiment			
Numerical analysis			

Fig. 3.6 Reproduced images on the camera (top: experiment, bottom: numerical analysis).

The cause of the phenomenon was explained as follows. First of all, we expanded signal beam in the medium into an ensemble of plane waves. The expansion is reasonable because the recorded hologram is Fourier transform hologram. Each on-pixel on the SLM corresponds to each plane wave with each different incident angle inside the medium. Next, we examined the reproduced beam diffracted from the hologram formed by interference of reference beam and one of the plane waves of signal beam whose incident angles are θ_0 and θ_S . Figure 3.7 shows the cross section of amplitude profile of reproduced beam $E(x)$ at each z position with reference to the center position of the plane wave of signal beam. When there is no oscillation in incident angle, there is no change in the waveforms of reproduced beam at each z position [Fig. 3.7(a)] because the weighting factor defined by Eq. (3.18) becomes always unity “1” at each z position. However, when there is an oscillation, the weighting factor is not “1”; consequently, the waveforms of reproduced beam become different at each z position. Figure 3.7(b) and 3.7(c) show the waveforms at $\theta_S = 0$ [deg] which corresponds to the right end pixel on the image in Figure 6 and at $\theta_S = 14$ [deg] which corresponds to the left end pixel on the image, respectively under the condition that $\alpha_w = 60$ [mdeg], $\theta_0 = 40$ [deg] and $\lambda = 405$ [nm]. As incident

angle of signal beam θ_S increases, the difference of the waveforms at each z position becomes large. Large difference of waveform yields a large decrease in intensity of reproduced beam because reproduced beams generated from each z position are superimposed in various phases.

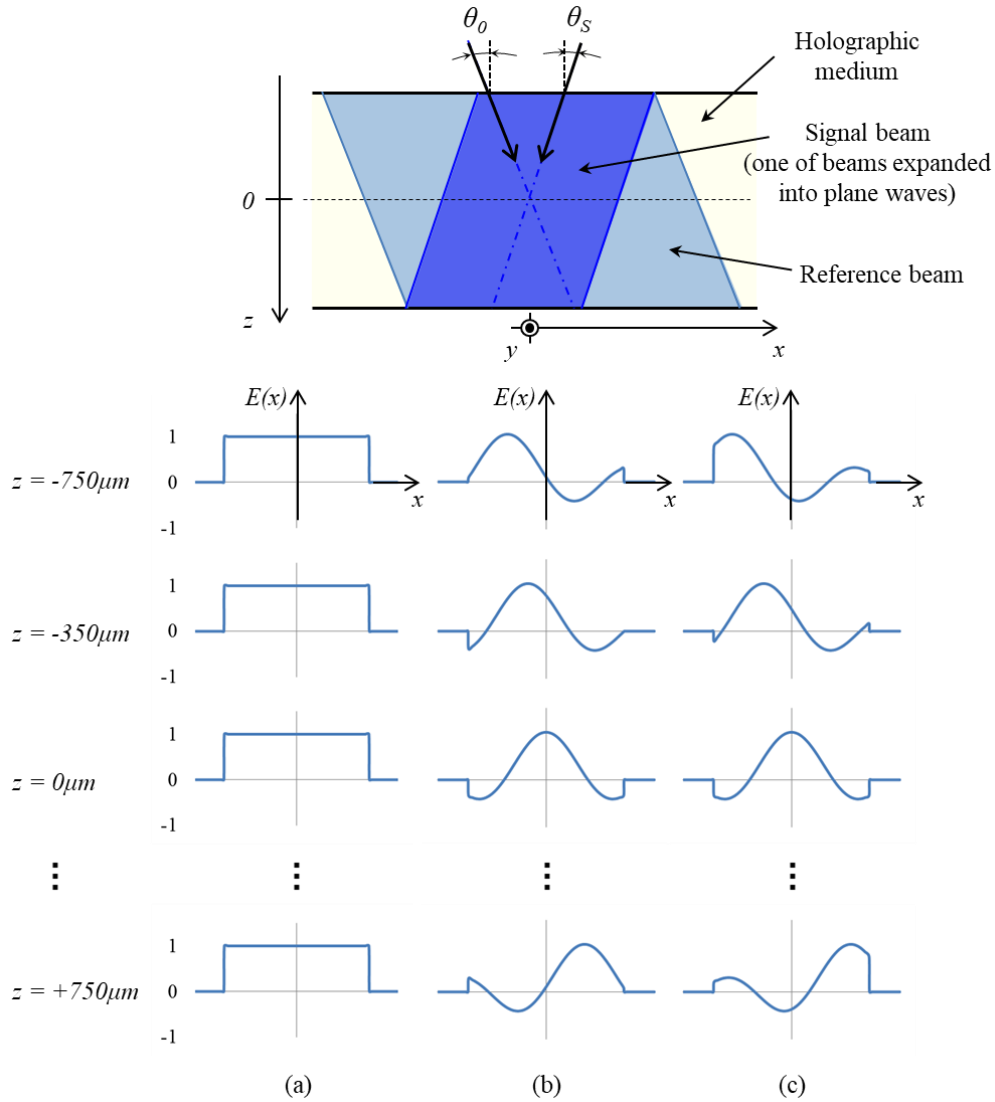


Fig. 3.7 Cross section of amplitude profile of reproduced beams at each z position, when (a) $a_w = 0$ mdeg, (b) $a_w = 60$ mdeg and $\theta_S = 0$ deg, and (c) $a_w = 60$ mdeg and $\theta_S = 14$ deg, under the condition that θ_0 is 40 deg and λ is 405 nm.

Figure 3.8 shows the results of the amplitude of the superimposed reproduced beam evaluated on the camera and square of the absolute value of point spread function (PSF) calculated by using the amplitude at each condition corresponding to Fig. 3.7.

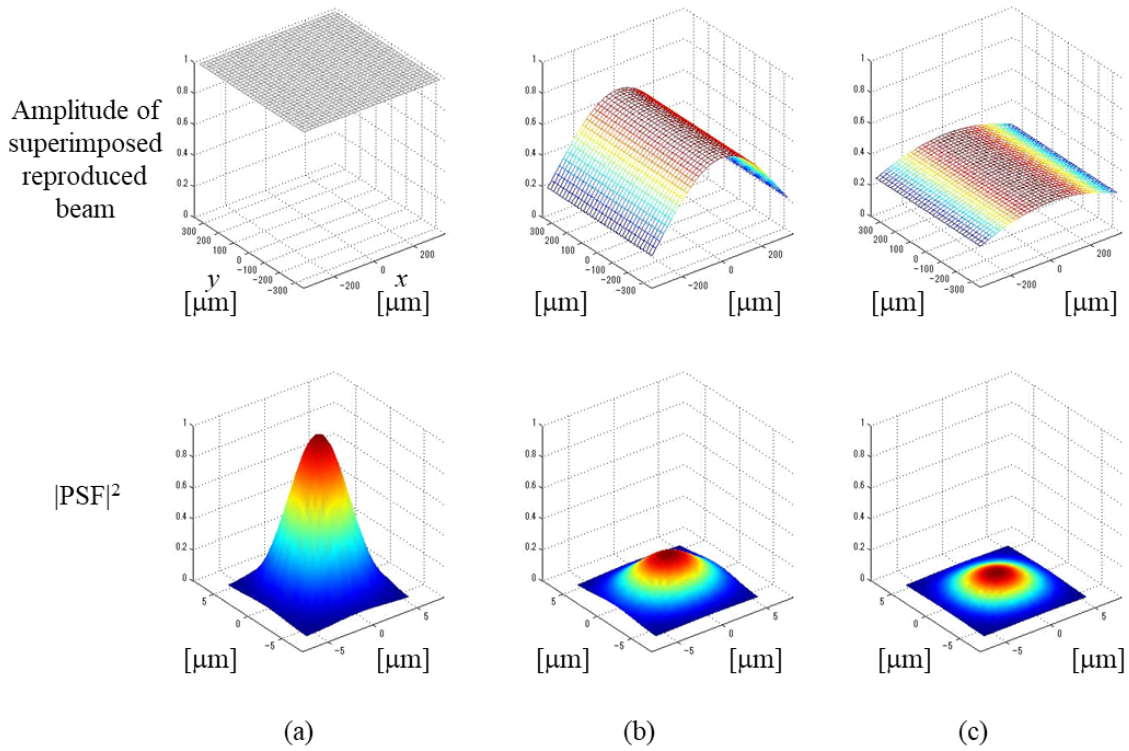


Fig. 3.8 Amplitude profile of the superimposed reproduced beam and $|PSF|^2$, when (a) $a_w = 0$ mdeg, (b) $a_w = 60$ mdeg and $\theta_s = 0$ deg, and (c) $a_w = 60$ mdeg and $\theta_s = 14$ deg, under the condition that θ_0 is 40 deg and λ is 405 nm.

$|PSF|^2$ means how the intensity profile recovered from the hologram formed by interference between reference beam and one of the plane waves of signal beam illuminates on the camera. We introduce the $|PSF|^2$ as an evaluation indicator to estimate degradation of recovered hologram image. When there is no oscillation in incident angle, $|PSF|^2$ shows relatively large value [Fig. 3.8(a)]. However, when there is an oscillation [Fig. 3.8(b), (c)], $|PSF|^2$ decreases compared to no oscillation case because reproduced beams generated from each z position are superimposed in various phases, which means the corresponding pixel on the camera becomes dark. As incident angle of signal beam θ_s increases, the decrease of $|PSF|^2$ is noticeable. As a result, the region of large angle of θ_s that is left side on the image in Fig. 3.6 becomes dark relatively.

Bragg selectivity curves in both (a) the experiment and (b) numerical analysis at each peak-to-valley of oscillation of reference beam angle a_w are shown in Fig. 3.9. The numerically analyzed curves were in good agreement with the experimental results.

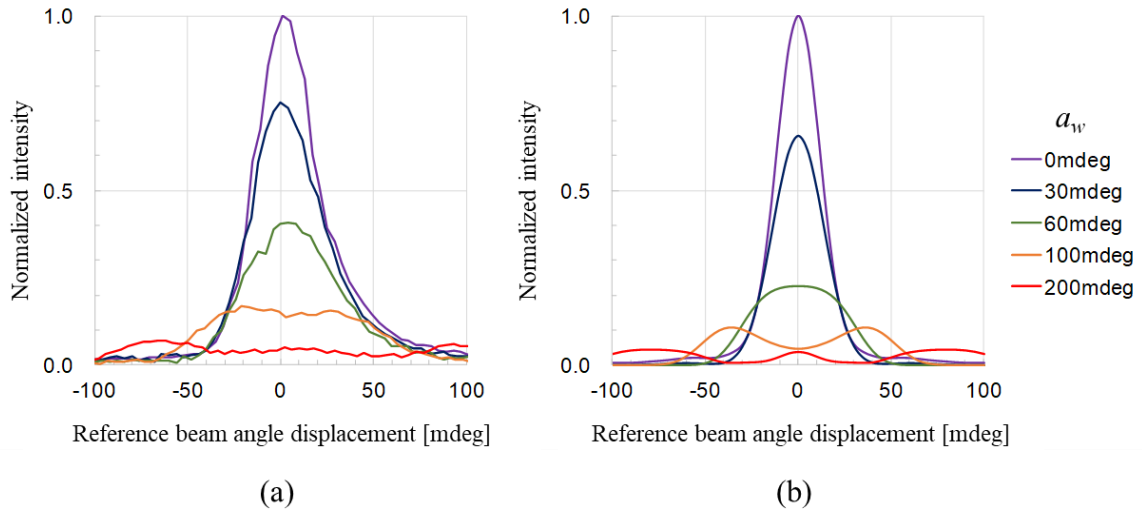


Fig.3.9 Bragg selectivity curves in both (a) the experiment and (b) numerical analysis.

Figure 3.10 shows a graph of SNR with α_w on the horizontal axis. The solid line and some points in the graph show results of numerical analysis and measured SNR. Although the curve calculated by numerical analysis showed a little higher sensitivity, the deterioration behavior caused by the oscillation was in good agreement with experimental results. A phase change of signal beam was not implemented in the numerical analysis as a preliminary study, however, phase fluctuations in the optical path of signal beam caused by such as atmospheric fluctuations and phase mask ^{48,49)} should occur in practical cases. It is considered these phase fluctuations minimized the effect of interference occurred between reproduced beams diffracted from the ensemble of the fringes corresponding to each oscillating state during recording state, eventually showed better SNR in the experiment compared to the numerical analysis.

Thus, in terms of reproduced image and SNR, comparison of experimental results with numerical analysis was carried out. Both results indicated same behavior as a function of amplitude of oscillation. The validity of optical modeling of oscillation effect was verified through the comparison.

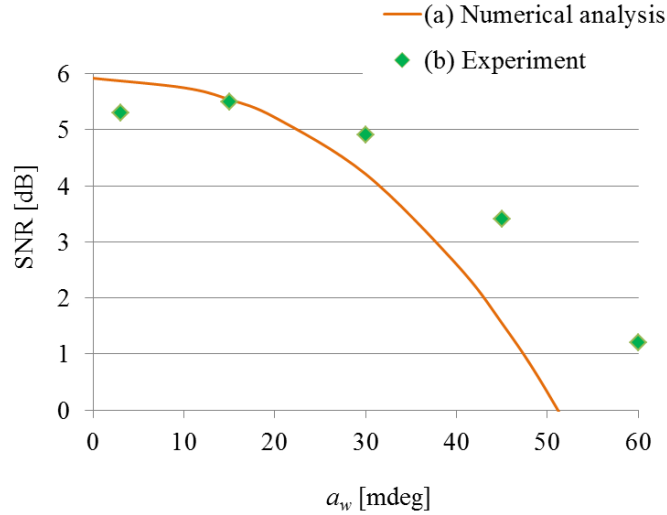


Fig. 3.10 SNR as a function of amplitude of angle oscillation a_w .

3.3.2 Effect of optical method of compensation for mechanical vibration effect

As proposed in Sect. 3.2, the oscillation effect of reference beam angle during recording state can be compensated optically by appropriately modulating amplitude and phase of reference beam during readout state. The compensation effect due to the modulation was numerically analyzed in this section. Under the condition that an incident angle of reference beam oscillates in a simple harmonic oscillation, three different types of optical filters for the modulation were compared. First optical filter is the one defined by Eq. (3.37). For instance, when $a_w = 40$ [mdeg], $\theta_0 = 40$ [deg] and $\lambda = 405$ [nm], the amplitude and phase profile of the first filter is described in Fig. 3.11(a).

We also consider a simplified optical filter as a second one, based on the profile of the first filter. For the second filter the phase modulation is the same as that of the first filter, however, the amplitude modulation is set uniform [Fig. 3.11(b)]. The transmittance is designed so that the intensity of reproduced beam on the camera becomes same as the first optical filter case. In this example, 1.4 times larger amplitude of reference beam was necessary to achieve the same intensity. The characteristic of third optical filter is further simplified based on the second optical filter [Fig. 3.11(c)]. There is no phase modulation anymore, and transmittance is designed as same as the second filter.

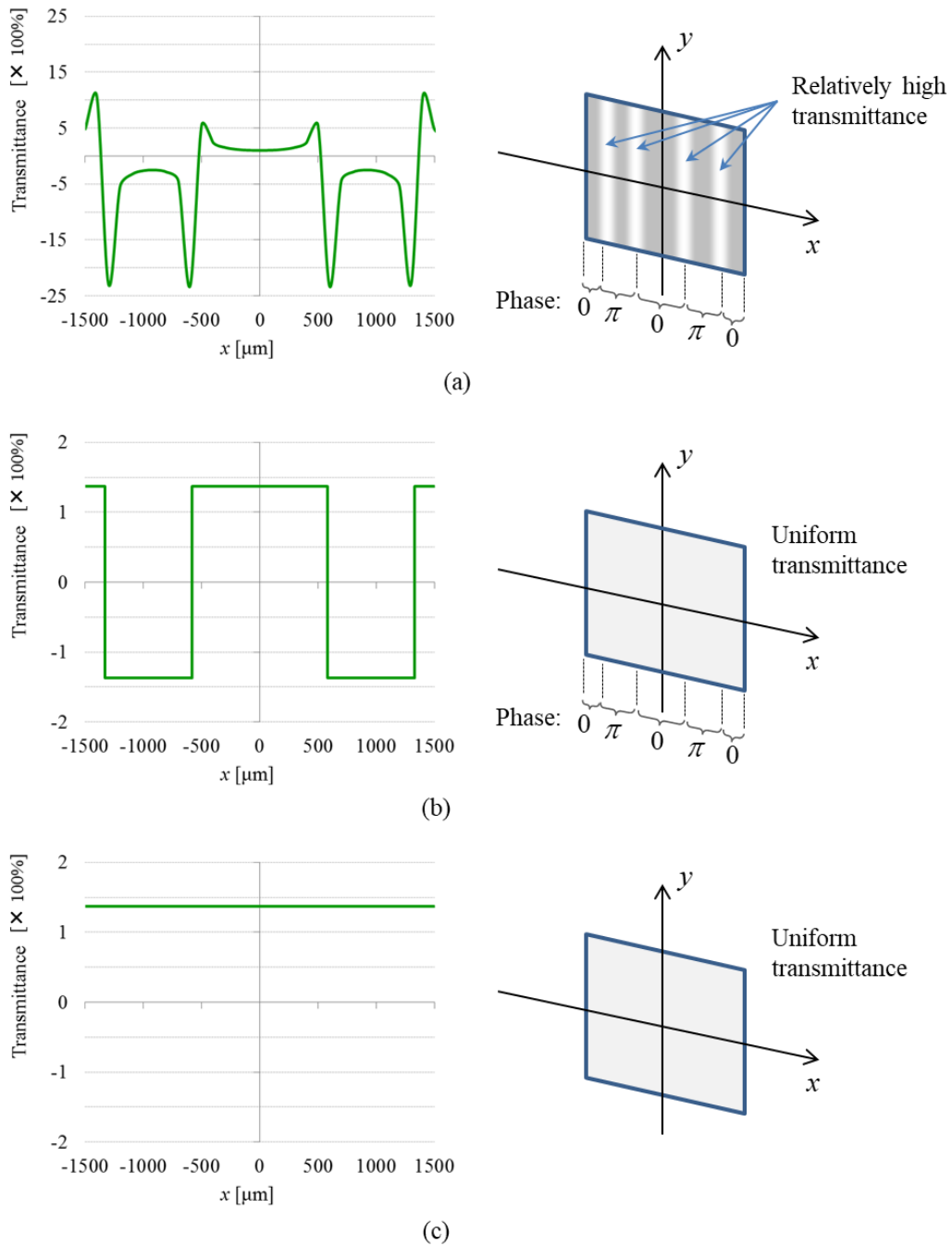


Fig. 3.11 Amplitude and phase profile of the (a) an ideal amplitude and phase combined optical filter, (b) phase only optical filter, and (c) amplitude optical filter, under the condition that a_w is 40 mdeg, θ_0 is 40 deg and λ is 405 nm.

Figure 3.12 shows simulated SNR as a function of a_w for the three filters. According to a_w , the characteristics of amplitude and phase profiles of each filter were optimized. The SNR of all the three optical filters exceeded the original SNR which was calculated in the case of no compensation. Although the compensation effect due to the first optical filter showed the best effect among the three filters as expected, the second optical filter showed comparable effect to the first filter. The third optical filter also showed comparable effect within the range of small amplitude of oscillation a_w because a noise independent of amount of light such as electrical noise of camera was taken into account in the simulation, however SNR dropped dramatically when a_w exceeds approximately 40 [mdeg]. Considering these results, the second optical filter is most practical among these filters because the filter shows fine balance of required amplitude modulation with required power, although 1.4 times larger amplitude of reference beam was necessary than first filter and SNR slightly deteriorated around $a_w = 40$ [mdeg] due to amplitude modulation not eliminated by the second filter. Also, phase correction was crucial factor for the compensation compared to amplitude correction. We consider this is reasonable because the deterioration of SNR was caused by the decrease of intensity of reproduced beam. The decrease was caused by superimposition of reproduced beams generated from each z position in various phases as described in Fig 3.7. Phase modulation due to the first and second optical filters fulfilled the role to correct phase relationship among each reproduced beam at each z position and superimpose in phase.

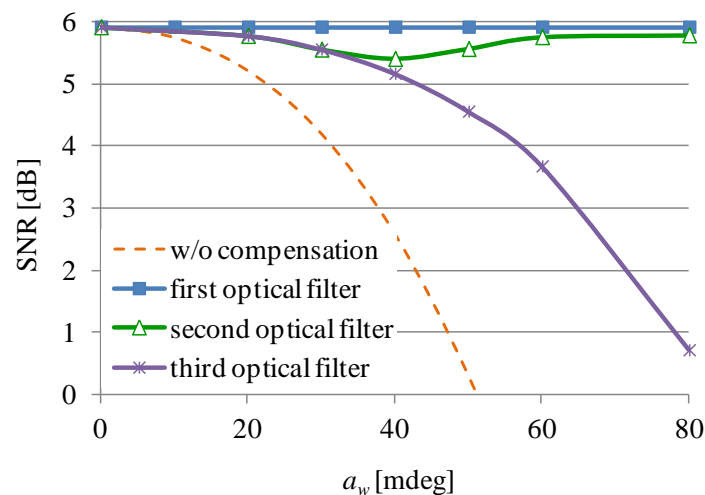


Fig. 3.12 SNR with and without compensation.

Figure 3.13(a) shows the cross section of amplitude profile of reproduced beam at each z position with reference to the center position of the plane wave of signal beam with the compensation employing the second filter under the condition that $a_w = 60$ [mdeg], $\theta_0 = 40$ [deg], $\theta_S = 14$ [deg] and $\lambda = 405$ [nm]. Because each reproduced beam at each z position can superimpose in phase due to the second filter, the amplitude of superimposed reproduced beam and $|PSF|^2$ were improved and increased as described in Fig. 3.13(b), compared to those on the same condition without the compensation as showed in Fig. 3.8(c).

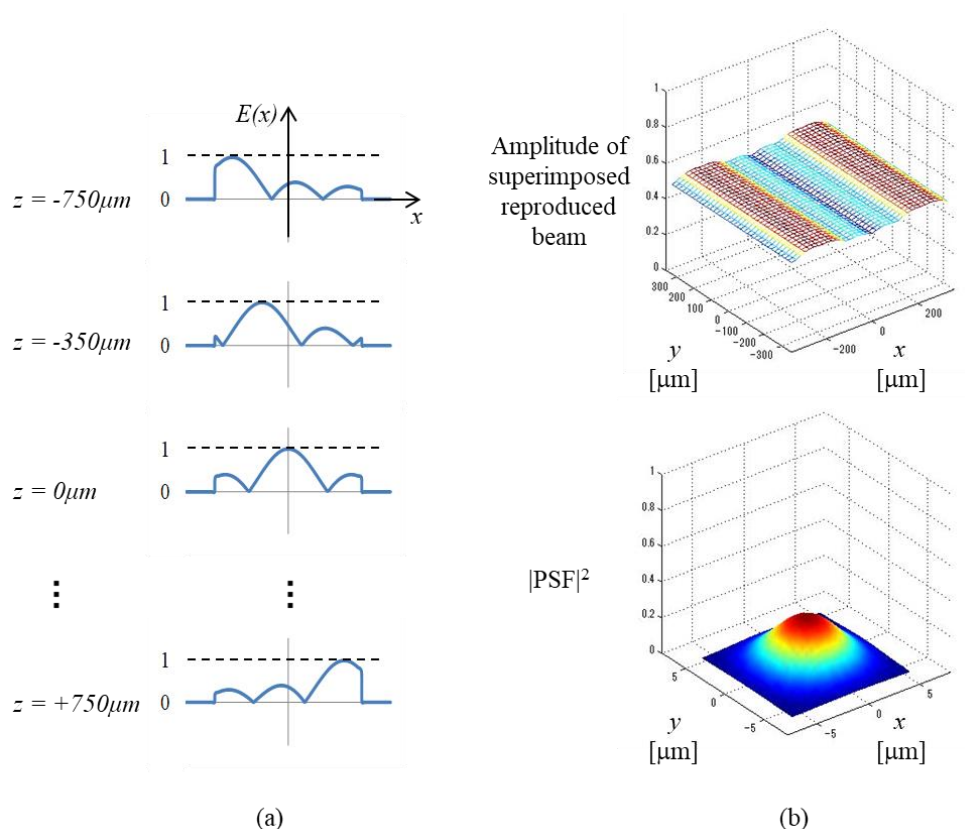


Fig. 3.13 (a) Cross section of amplitude profile of reproduced beams at each z position. (b) Amplitude profile of the superimposed reproduced beam and $|PSF|^2$, when $a_w = 60$ mdeg, $\theta_S = 14$ deg, θ_0 is 40 deg, and λ is 405 nm under the condition the second optical filter is implemented.

We believe, to the best of knowledge of authors, this is the first numerical confirmation of the possibility of the post compensation of degradation of the holographic data channel caused by mechanical instabilities during the recording process. The preliminary analysis for the compensation method indicates that it is highly feasible to increase a robustness of HDSS against mechanical instabilities.

3.3.3 Suppression of vibration effects on reproduced holographic image

Owing to the mathematical formulation of the vibration effects, as described in Sect. 3.1, it is possible to quantify the effects. For example, when hologram is recorded in the exposure time t_r earlier than the vibration cycle, it is possible to quantitatively show that the effect can be suppressed, as shown in the following.

When a temporal function of a vibration amplitude $h(t)$ is described as

$$h(t) = a_0 + a \sin(2\pi f_{\text{vib}}t + \phi_0) \quad (3.38)$$

where a_0 is a DC component, a is a vibration amplitude, f_{vib} is a frequency, and ϕ_0 is an initial phase of the vibration, the standard deviation σ_{vib} of the amplitude $h(t)$ is written as

$$\begin{aligned} \sigma_{\text{vib}} &= \sqrt{\frac{1}{t_r} \int_0^{t_r} |h(t) - \overline{h(t)}|^2 dt} \\ &= a \sqrt{\frac{1}{2t_r} \left[t_r - \frac{\sin\{2(2\pi f_{\text{vib}}t_r + \phi_0)\} + \sin 2\phi_0}{4\pi f_{\text{vib}}} \right] - \left(\frac{\cos \phi_0 - \cos(2\pi f_{\text{vib}}t_r + \phi_0)}{2\pi f_{\text{vib}}t_r} \right)^2} \end{aligned} \quad (3.39)$$

According to the previous research^{50,51}, it has been shown that the vibration effect on reproduced holographic image was almost uniquely determined by the standard deviation σ_{vib} of the vibration amplitude. Then, once acceptable standard deviation σ_{vib} is determined from the viewpoint of acceptable system noise explained in the next Chapter, acceptable vibration amplitude a_{acpt} can be expressed as

$$a_{\text{acpt}} = \frac{\sigma_{\text{vib}}}{\sqrt{\frac{1}{2t_r} \left[t_r - \frac{\sin\{2(2\pi f_{\text{vib}}t_r + \phi_0)\} + \sin 2\phi_0}{4\pi f_{\text{vib}}} \right] - \left(\frac{\cos \phi_0 - \cos(2\pi f_{\text{vib}}t_r + \phi_0)}{2\pi f_{\text{vib}}t_r} \right)^2}} \quad (3.40)$$

Figure 3.14 shows a graph of acceptable vibration amplitude as a function of vibration frequency f_{vib} when σ_{vib} is set to 20 [nm]. As the recording exposure time t_r becomes shorter, the amount of acceptable vibration amplitude a_{acpt} increases. Although it can be intuitively understood that shorter exposure time of recording hologram suppresses the vibration effects, it becomes possible to quantify numerically the suppression.

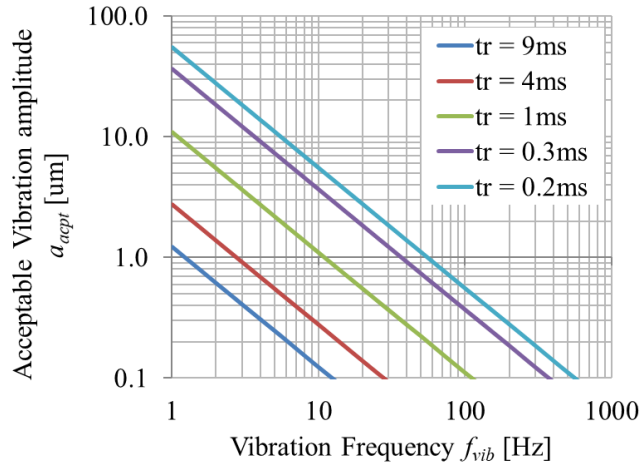


Fig. 3.14 Graph of acceptable vibration amplitude as a function of vibration frequency when σ_{vib} is set to 20 [nm].

3.4 Conclusions

The effects of vibration due to mechanical instabilities on HDSS were formalized by incorporating the concept of time-average holography. By replacing mechanical instabilities of galvano mirror and spindle motor with oscillation of reference beam angle and holographic disk displacement, these effects were formalized and successfully incorporated into the modeling of data recording and readout process for HDSS based on the Layer-by-Layer method. The modeling combined with the concept allowed us to take into account arbitral oscillation profile of the reference and signal beams during recording state. Through the comparison of the simulation results with experimental results, it was confirmed that for a realistic HDSS configuration having 576x1172 pixels recorded by high NA optics with 405 [nm] laser, the developed optical model was able to predict signal level of the degraded holographic image due to mechanical instabilities.

Based on the formalization and experimental verification, an optical compensation method to recover the degraded holographic image was examined. The preliminary numerical analysis showed that the method, optical filtering by modulating of the amplitude and phase of reference beam during the readout state, was effective to recover the degraded holographic data. The comparative study of the profile of the optical filter indicated phase modulation was a crucial factor to compensate for mechanical vibration effect.

Owing to the developed numerical formulation, it became possible to quantify the improvement how shorter exposure time of recording hologram suppressed the vibration effects, whereas the improvement had been intuitively understood so far.

Chapter 4

Estimation of System Noise at Recording Density of 1 Tbit/in²

As described in Chapter 1, bit cost of 0.01 [\$/GB] that is comparable to Tape media is required for HDSS to play the role of storage media for data archiving such as LTDP. If holographic disks of 1TB/disk can be supplied with less than \$10/disk, the bit cost will be realized. In this Chapter, required recording density for the bit cost and system noise of HDSS at the required density are discussed. In the discussion, a signal quality metric is introduced to estimate the system noise in order to confirm whether the required recording density is feasible or not. The polarization and vibration effects, which are discussed in Chapter 2 and 3, are clarified in the expression of the metric through the analysis of the system noise.

4.1 Parameters of optical system for realizing bit cost of 0.01 [\$/GB]

Achievable data capacity depends on recording density, size of recording area in holographic disk, and code rate which is the ratio of capacity of user data to raw data. Figure 4.1 shows an example of required recording density as a function of achievable data capacity on the condition that disk diameter is 120 [mm] and outer and inner radius of recording area in the disk are 57 [mm] and 25 [mm], respectively, as described in Table III. When the target of data capacity is set to 1 [TB/disk] for realizing bit cost of 0.01 [\$/GB], the recording density of 1 [Tbit/in²] is required at the code rate of 0.66.

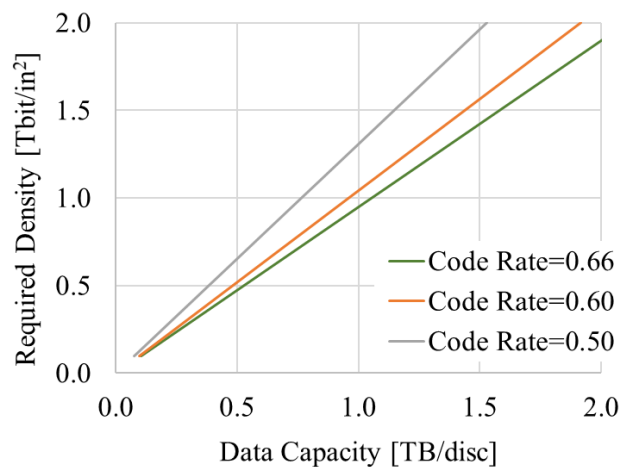


Fig. 4.1 Graph of Required recording density [Tbit/in²] as a function of data capacity [TB/disk]

Table III Example of disk structure.

<i>Disc</i>	<i>diameter</i>	120 [mm]
<i>Disc Recording area</i>	<i>Outer radius</i>	57[mm]
	<i>Inner radius</i>	25 [mm]

Then, the system parameters of HDSS to achieve the recording density of 1 [Tbit/in²] is designed. The system parameters are summarized in Table IV.

Table IV Designed system parameters for realizing recording density of 1[Tbit/in²].

<i>ECLD</i>	<i>Wavelength</i>	405 [nm]
<i>Optical axis with respect to medium (in free space)</i>	<i>Reference beam</i>	35 - 61 [deg]
	<i>Signal beam</i>	-25 [deg]
<i>SLM</i>	<i>Pixel pitch</i>	7.8 [μm]
	<i>Pixel number</i>	2100 × 2100
	<i>Raw data size of a page data</i>	2.8 [M bits]
	<i>Number of angular multiplexing</i>	220
<i>Objective lens</i>	<i>Focal length</i>	12.4 [mm]
	<i>Numerical Aperture</i>	0.6
<i>Nyquist aperture</i>	<i>Size (Compared to Nyquist size)</i>	$\sqrt{1.3}$ times larger
<i>Hologram size</i>	<i>Bragg</i>	500 [μm]
	<i>Radial</i>	734 [μm]
	<i>Code rate</i>	0.66
	<i>Disc size (Diameter)</i>	12 [cm]

The optical architecture described in Fig. 2.5 is followed for the system. The Nyquist aperture is placed in the signal beam path to reduce the size of the recorded hologram to maximize the recording density and eliminate unnecessary signals generated from the adjacent hologram for readout. The width of the Nyquist aperture was set to be $\sqrt{1.3}$ times larger than the Nyquist size. Therefore, the hologram size h_{holo} in the

radial direction is

$$h_{\text{holo}} = \sqrt{1.3} \times \frac{\text{wavelength} \times \text{focal length of objective lens}}{\text{SLM pixel size}} = \sqrt{1.3} \times \frac{0.405 \times 12.4 \times 10^3}{7.8} = 734 [\mu\text{m}] \quad (4.1)$$

On the other hand, the hologram size in the Bragg direction cannot be calculated simply because optical axis of signal beam is obliqued and run-length-limited (RLL) coding⁵²⁾ which optically reduces the hologram size is used in the direction. Figure 4.2 shows the graph of numerically analyzed the effect of inter-books crosstalk as a function of distance between books in the Bragg direction. The vertical axis shows the estimated noise whose definition is explained in the next section. According to the graph of Fig. 4.2, the hologram size in the Bragg direction was estimated to be 500 μm within the range that the noise is not generated.

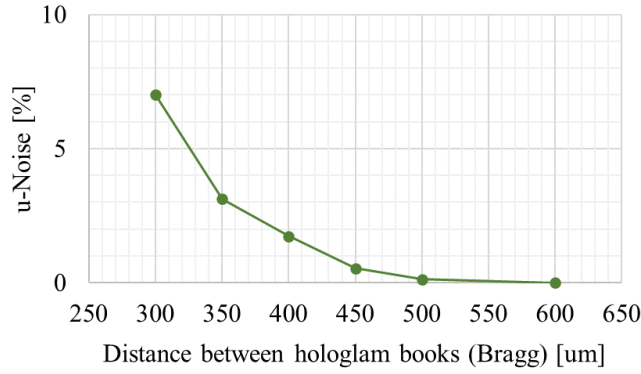


Fig. 4.2 Graph of numerically analyzed inter-books crosstalk as a function of distance between books in the Bragg direction.

Under the condition of the hologram size, the recording density D_r of HDSS with the system parameters described in Table IV is

$$\begin{aligned} D_r &= \frac{\text{raw data size of a page}}{\text{hologram size(Bragg)} \times \text{hologram size(Radial)}} \times \text{multiplexing number} \\ &= \frac{2.8 [\text{Mbit}]}{734 [\mu\text{m}] \times 500 [\mu\text{m}]} \times 220 = 1.08 [\text{Tbit}/\text{inch}^2] \end{aligned} \quad (4.2)$$

The system noise of HDSS is estimated in the next section.

4.2 Estimation of system noise

4.2.1 Signal quality metric to estimate system noise

To estimate the signal quality when multiple obstructive factors which degrade optical quality of reproduced holographic image are applied to the system, a signal quality metric as written in Eq. (4.3) is introduced^{53,54}.

$$\sigma_N = \frac{\sqrt{\sigma_{\text{on}}^2 + \sigma_{\text{off}}^2}}{\mu_{\text{on}} - \mu_{\text{off}}} \quad (4.3)$$

The metric σ_N is termed “normalized noise⁵³” in this Chapter. Standard deviations can be regarded as noise because these are root mean square (rms) values of the intensity captured by the camera. The normalized noise, when multiple obstructive factors x_i ($i = 1, 2, \dots, n$) are applied to the system, can be calculated by the root sum square as below.

$$\sigma_N(x_1, x_2, \dots, x_n) = \sqrt{\sum_{i=1}^n \sigma_i(x_i)^2} \quad (4.3)$$

The noise σ_i generated by each factor x_i is termed “unique noise” in this Chapter. Next, the limit of the normalized noise was determined. The noise has a high relationship with the page quality. The relationship between the normalized noise and bit error rate (bER) after error correction is shown in Fig. 4.3. The limit of the normalized noise on the condition of the code rate of 0.66 was determined as 56% which is sufficient not to cause read errors.

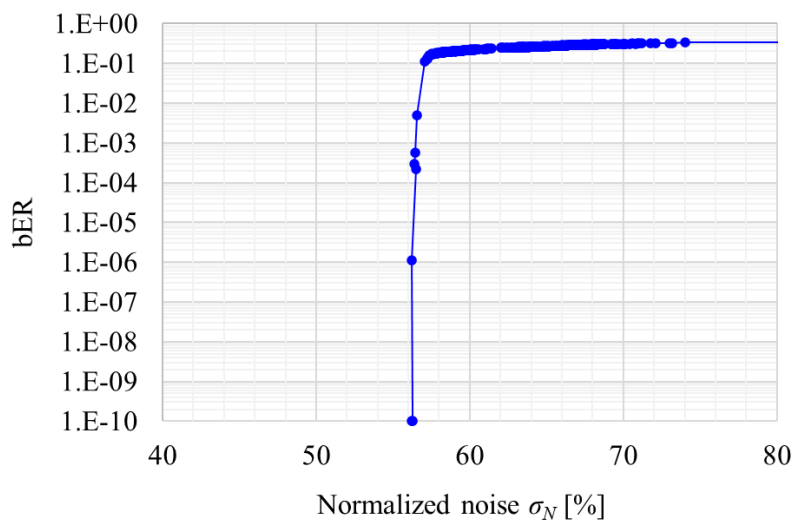


Fig. 4.3 Graph of bER as a function of normalized noise on the condition of code rate of 0.66.

4.2.2 System noise at recording density of 1 Tbit/in²

As shown in Table V, the sixteen factors which degrade optical quality of reproduced holographic image are selected from past experience to estimate the system noise at recording density of 1 [Tbit/in²].

Table V Selected factors which degrade optical quality of reproduced holographic image.

#	Obstructive factors		typical value	notes
1	polarization effect		-	explained in the section 1.1.4(e)
2	vibration effect	ref. beam angle	amp. = 0.001 [deg]	explained in the section 1.1.4(f)
3		de-track	amp. = 1 [μ m] (freq. = 30 [Hz])	explained in the section 1.1.4(f)
4	disk de-track		75 [μ m]	radial runout due to eccentricity of optical disk
5	disk defocus		150 [μ m]	axial runout due to vertical deviation of optical disk
6	uneven intensity distribution	sig. beam	-	ringing due to beam propagation, dust, etc.
7		ref. beam	-	ringing due to beam propagation, dust, etc.
8	ref. beam angle offset		0.005 [deg]	explained in the section 1.1.3(b)(c)
9	wavelength offset		0.1 [nm]	explained in the section 1.1.3 (b)
10	thermal change		± 9 [$^{\circ}$ C]	explained in the section 1.1.3(b)
11	wavefront aberration of ref. beam		0.07 [λ rms]	explained in the section 1.1.3(d)
12	misalignment of relative position b/w ref. and sig. beams		0.2 [mm]	due to misalignment of ref. and sig. beams
13	effect of Nyquist filter		1.3 \times Nyquist size	due to lack of high frequency signal
14	inter-page crosstalk		3.2 null	leakage of unnecessary signal from adjacent page
15	deterioration of signal intensity		-	due to excessive exposure after hologram recording
16	scatter noise (SSR: signal-to-scatter ratio)		SSR=15	due to rough surface of disk, molecules in a medium

Each unique noise caused by each factor in Table V is numerically calculated by the established optical model described in Chapter 2 and 3.

Figure 4.4 shows the calculated unique noise caused by the polarization effect. When the reference beam was p-polarized during readout, large unique noise was generated because of the intensity gradient explained in Chapter 2.

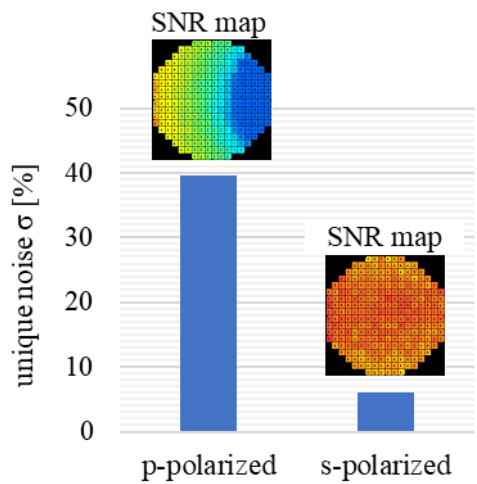


Fig. 4.4 Estimated unique noise caused by polarization effect.

Then, the unique noise caused by the vibration effect was examined. Fig. 4.5 shows the measured oscillatory waveform of the galvano-mirror angle. The vibration amplitude of 0.5 [mdeg] that corresponds to 1 [mdeg] for reference beam angle was observed. And Fig 4.6 shows the measured oscillatory waveform of disk position controlled by the spindle motor. The vibration amplitude of 1 [μm] with representative frequency of approximately 30 [Hz] was observed. Considering these vibration amplitudes, the vibration effect was estimated under the condition that the exposure time t_r was set to 1 [ms] based on the performance of conventional system.⁵⁶⁾ Although the vibration amplitude of 1 [mdeg] of reference beam angle did not affect the signal quality of the reproduced holographic image, the vibration amplitude of 1 [μm] of disk position had a significant influence on the signal quality on the condition of $t_r = 1$ [ms], as shown in Fig. 4.7.

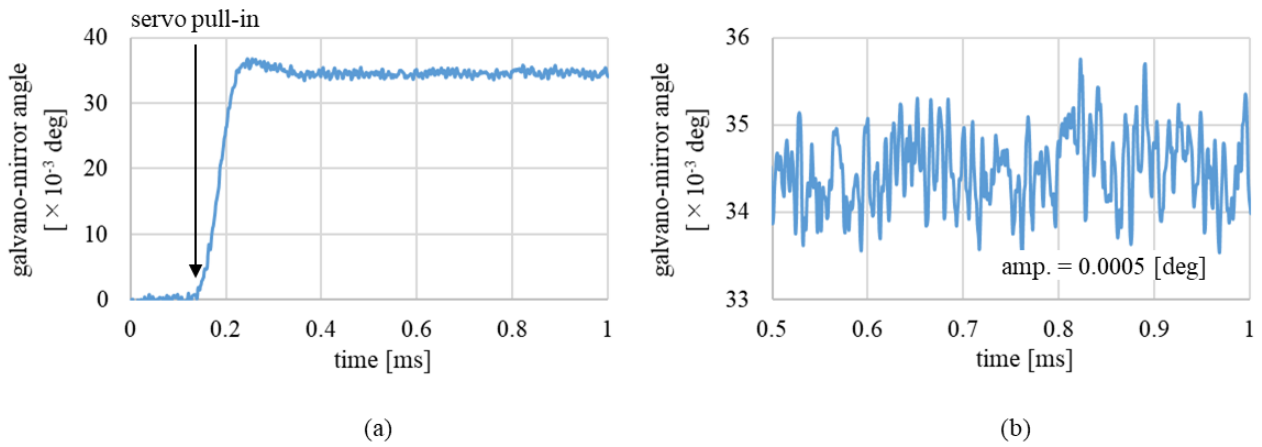


Fig. 4.5 (a) Graph of measured oscillatory waveform of galvano-mirror angle, and (b) expanded graph in the vertical axis of the graph (a).

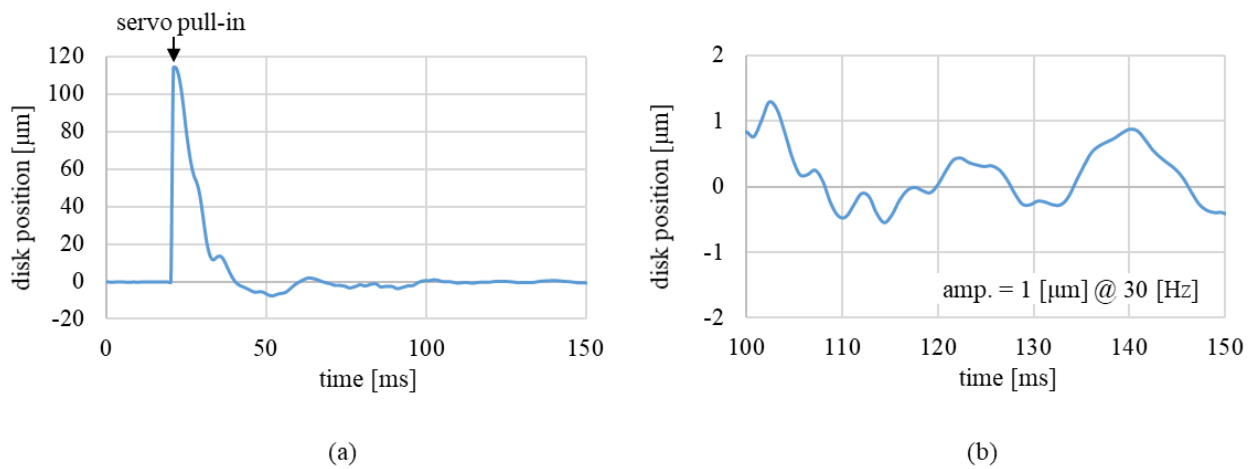


Fig. 4.6 (a) Graph of measured oscillatory waveform of disk position, and (b) expanded graph in the vertical axis of the graph (a).

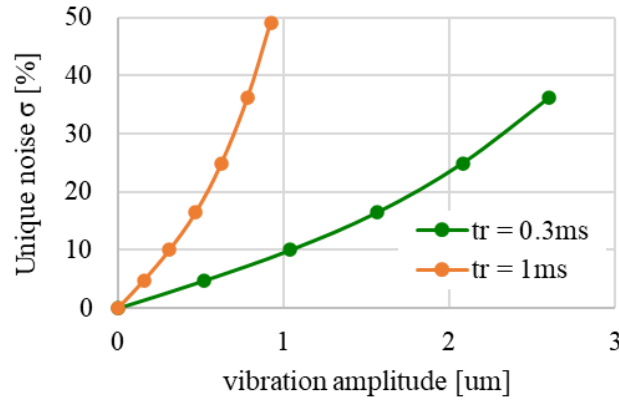


Fig. 4.7 Estimated unique noise caused by vibration effect (disk position).

Figure 4.8 shows the numerically calculated result of accumulated noise caused by each factor in Table V. There are two bars in Fig. 4.8. The bar (a) indicates the estimated system noise when reference beam is p-polarized during readout and exposure time during recoding t_r is 1 [ms]. Significant noise due to the polarization and vibration effects was confirmed. Due to these effects, the system noise greatly exceeds the required threshold of $\sigma_N = 56$ [%].

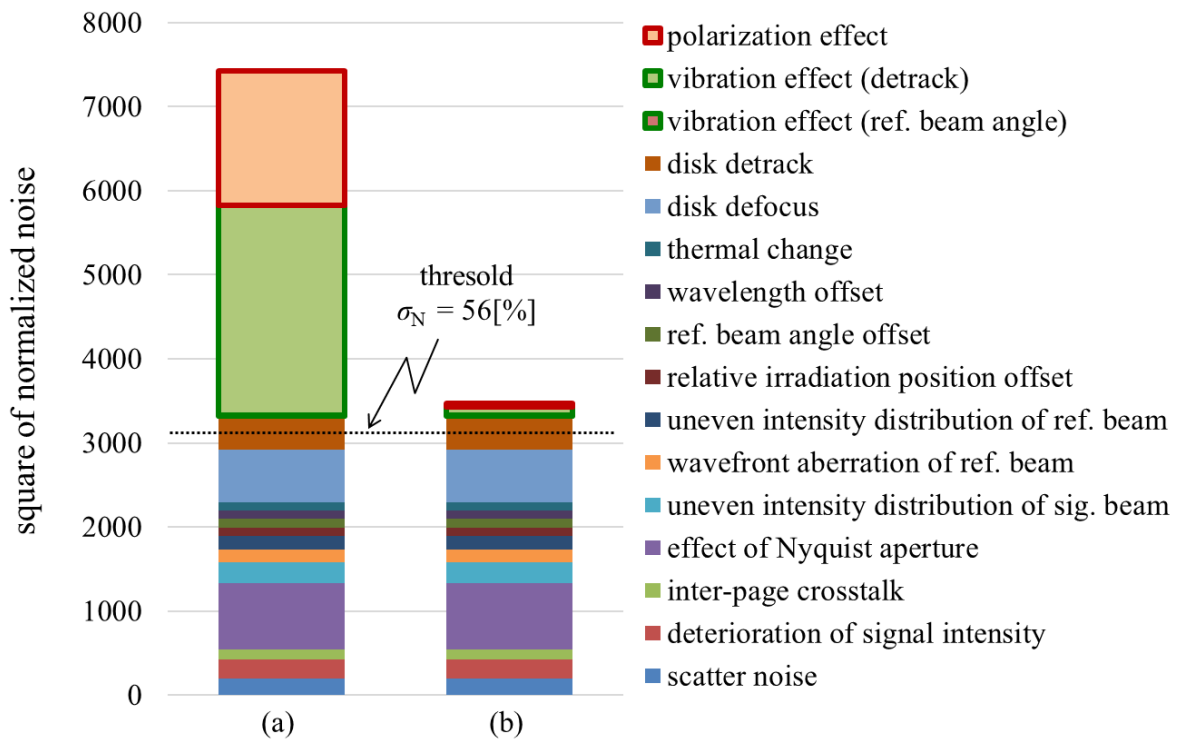


Fig. 4.8 Bar graph of estimated system noise when (a) ref. beam is p-polarized and t_r is 1 [ms], (b) ref. beam is s-polarized and t_r is 0.3 [ms].

On the other hand, the bar (b) indicates the estimated system noise when reference beam is s-polarized during readout and exposure time during recoding t_r is shortened to 0.3 [ms]. It was confirmed that the polarization and vibration effects were sufficiently suppressed. The short exposure time can be achieved by a high-power laser and a holographic medium with high sensitivity.

However, the system noise still exceeds the threshold. It is necessary to further suppress the system noise. According to the breakdown of the system noise, the effect of Nyquist aperture is relatively larger than others. The Nyquist aperture is used to save M# consumption for recording multiplexed holograms and to eliminate crosstalk noise from neighboring holograms for readout. In exchange for these effects, the system noise is increased because a part of original signal is filtered. Although the system noise can be suppressed by enlarging the area of the Nyquist aperture, the achievable recording density is reduced. Figure 4.9 shows graphs of the normalized noise σ_N and the achievable recording density D_r as a function of the area of the Nyquist aperture. The amount of the area is normalized by the square of the Nyquist size. The decrease in the noise σ_N by increasing the area of the Nyquist aperture is insignificant. On the contrary, a large side effect of decreasing the achievable recording density becomes obvious. Other countermeasure instead of enlarging the area of the Nyquist aperture is preferable. The noise caused by disk displacement such as disk de-track and disk defocus are also relatively larger than others. Further improvement of the noise is examined in the next Chapter.

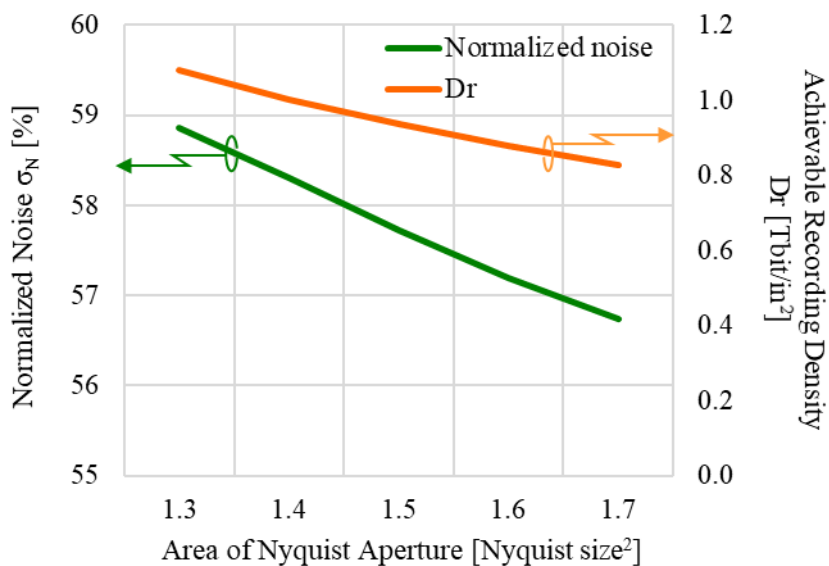


Fig. 4.9 Graphs of normalized noise σ_N and achievable recording density D_r as a function of area of Nyquist aperture

4.3 Conclusions

System parameters of HDSS to achieve the targeted recording density of 1 [Tbit/in²] for realizing the bit cost of 0.01 [\$/GB] was designed. Then, the system noise of the designed system was analyzed to confirm the feasibility of the targeted recording density. Owing to the noise mitigation method, such as applying s-polarized reference beam for readout hologram discussed in Chapter 2, and shorter exposure less than 0.3 [ms] for recording hologram discussed in Chapter 3, the system noise was significantly reduced. However, it was clarified the noise still exceeded the permissible level. Further improvement of the system noise, the necessity of suppression of positional error of holographic disk, which also had a large impact on the system noise, was proposed.

Chapter 5

Technique to Compensate for Influence of Disk De-track

The positional tolerance of a holographic disk is subject to become tight in exchange for their high-density recording. the positional tolerance of the holographic disk for readout should be within the order of micrometers to ensure readout quality.⁵⁴⁾ To strike a balance between large data capacity of terabyte class and a high transfer rate of the Gbps class, not only highly precise but also high-speed control of reference beam angle and holographic disk positioning is needed. Although several previous studies of the positioning of the holographic disk in a HDSS using angularly multiplexed recording were reported,^{55,56)} an effective technique that satisfies both the highly precise and high-speed positioning of the holographic disk has not been proposed yet. One of the difficulties is the higher inertia moment of the holographic disk than of the galvano mirror. Moreover, considering that the disk is often clamped eccentrically within 50-70 [μm], the mechanical accuracy achieved by the conventional control based on spindle or sled motors^{57,58)} no longer satisfies the required specification anymore.

In this study, a compensation method for the effect of positioning error, which precisely controls the positioning of a Nyquist aperture instead of a holographic disk, has been developed.⁵⁹⁻⁶¹⁾ The method relaxes the severe positional tolerance of the holographic disk so that a coarse positioning control performed by spindle or sled motors conventionally a conventional way can be sufficient for the positioning of the holographic disk. In addition, owing to the overwhelmingly light weight of the aperture, positioning control within the required time frame becomes feasible; consequently, contributes to realizing a HDSS with a large data capacity of terabyte class and a fast readout of gigabits per second class.

5.1. Methods

5.1.1 Compensation for effect of positioning error of holographic disk

The technique for positioning a holographic disk consists of a coarse positioning control performed by spindle or sled motors conventionally and a new compensation method by which the effect of a residual positioning error of the holographic disk caused by the coarse positioning is compensated. The details of the new compensation method are discussed in this section.

Figure 5.1(a) illustrates the basic geometry for the readout of a hologram. For data recovery, a reference beam illuminates the recorded hologram in the holographic disk. A mirror is placed on the back surface of the disk to retroreflect the reference beam for data recovery in a quasi-phase conjugate readout geometry. The reproduced beam diffracted from the hologram travels through an objective lens and a relay lens, and then the hologram image is reproduced by a camera. A Nyquist aperture is placed in the Fourier plane of the relay lens. The aperture is originally used to save $M\#$ consumption for the recording hologram and to eliminate crosstalk noise from neighboring holograms for readout. The width of the Nyquist aperture was set to be 1.14 times larger than the Nyquist size D_{Nyq} , which is defined as

$$D_{Nyq} = \frac{\lambda f_r}{\Delta_{SLM}} \quad (5.1)$$

where Δ_{SLM} is the spatial light modulator (SLM) pixel pitch, λ is the wavelength, and f_r is the focal length of the relay lens.

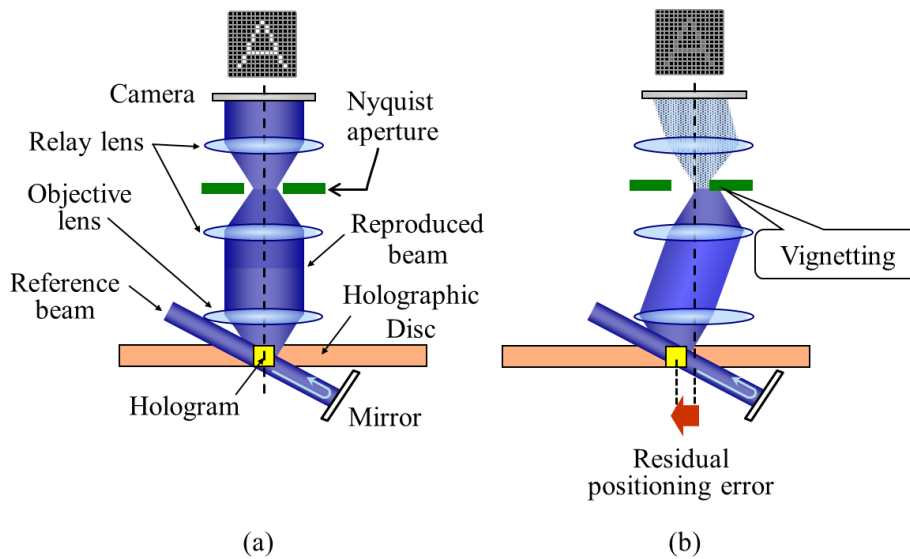


Fig. 5.1 (a) Basic geometry for readout of hologram and (b) beam propagation of reproduced beam when residual positioning error caused by coarse positioning exists.

When a residual positioning error caused by the coarse positioning exists as shown in Fig. 5.1(b), part of the reproduced beam is blocked by the aperture, as is obvious from the optical geometry. As a result, the quality of a reproduced hologram image deteriorates. the positional tolerance of the holographic disk for readout

should be within the order of micrometer to ensure high readout quality.⁵⁴⁾ To relax the severe tolerance of the positioning during readout, the aperture is utilized to compensate for the effect of the positioning error of the holographic disk.

The compensation method is illustrated conceptually in Fig. 5.2. To prevent the deterioration caused by the vignetting of the reproduced beam at the aperture, the position of the Nyquist aperture is optimized accordingly to allow the reproduced beam to pass through the aperture instead of the precise positioning control of the disk.

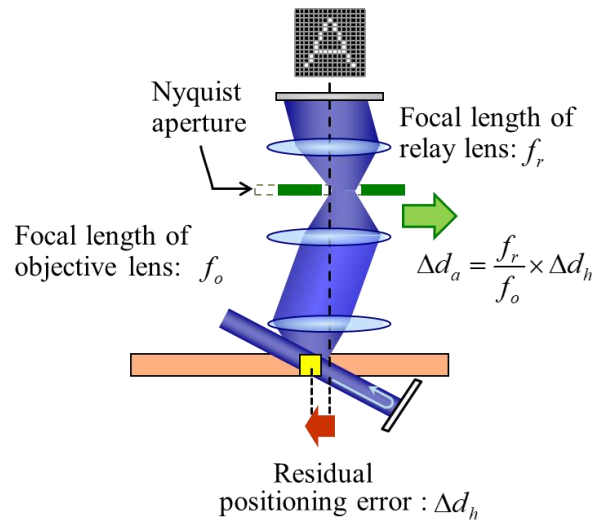


Fig. 5.2 Schematic of new compensation method for effect of residual positioning error of holographic disk.

The positional displacement Δd_a of the aperture is determined by the magnification calculated using the ratio of the focal length of the relay lens f_r to that of the objective lens f_o ,

$$\Delta d_a = \frac{f_r}{f_o} \times \Delta d_h \quad (5.2)$$

where Δd_h is the residual positioning error of the holographic disk. For example, when $f_r = 40$ [mm], $f_o = 12.4$ [mm] and the residual positioning error of the disk Δd_h remains 50 [μm], the Nyquist aperture is moved $\Delta d_a = 161$ [μm] to an appropriate direction to ensure high readout quality, even when the residual positioning error of the disk Δd_h is outside of the tolerance range.

Compared with the size and weight of the holographic disk, those of the Nyquist aperture can be markedly reduced, which is advantageous for realizing fast readout. Furthermore, there is another advantage in that the

compensation method has high affinity with an objective lens actuator for conventional ODS systems such as DVDs and Blu-ray discsTM. Conventional actuator technologies are applicable to moving the Nyquist aperture.

5.1.2 Positioning error signal for Nyquist aperture control

In this section, how to generate a positioning error signal to achieve feedback position control of the Nyquist aperture is described. The error signal can be generated if the intensity of the reproduced beam illuminating the outer area of the Nyquist aperture can be detected, as shown in Fig. 5.3.

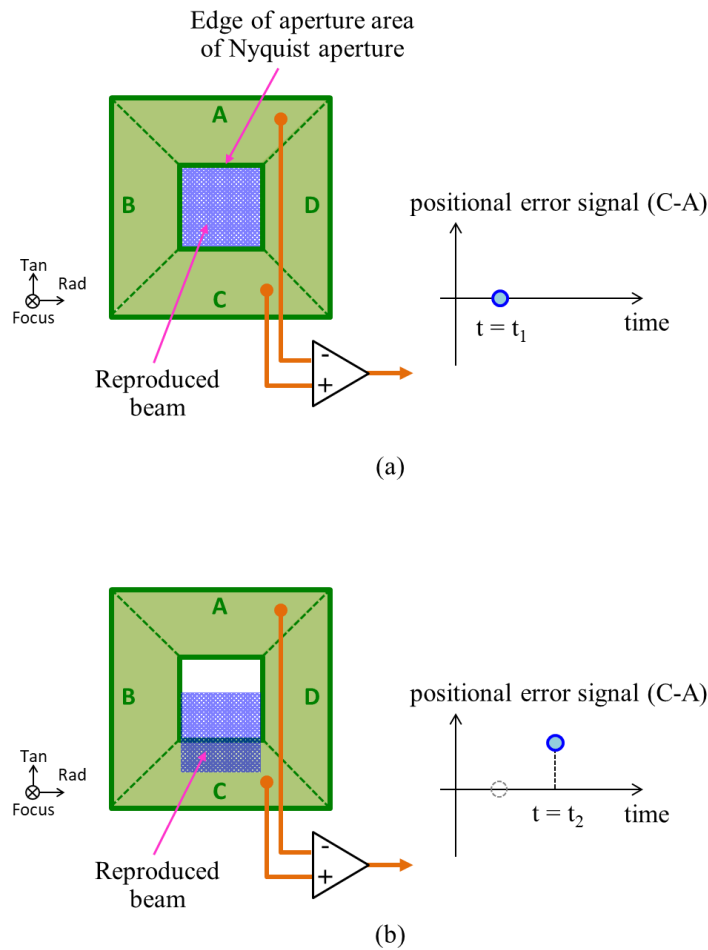


Fig. 5.3 Schematic diagram of state generating positioning error signal for Nyquist aperture control at (a) $t = t_1$ and (b) $t = t_2$.

For example, the positioning error signal in the tangential direction related to the relative displacement between the reproduced beam and the aperture can be generated by subtracting an output signal A from signal C, because the larger the relative displacement becomes, the more the area of the reproduced beam protruding

from the aperture area increases.

To realize this concept, an optical filter was designed. The optical filter fulfills both the function of extracting the intensity of the beam illuminating the outer area of the aperture area to generate the positioning error signal and the original function of the Nyquist aperture as explained in Sect. 5.2.1. The optical filter is composed of two regions. The first region is just a transparent area that plays the original role of the Nyquist aperture. The reproduced s-polarized beam passing through the first region is reflected by a polarized beam splitter (PBS) prism and is then incident on the camera for readout, as described in Fig. 5.4. The second region surrounding the first region of the filter consists of a half-wave plate (HWP). The reproduced s-polarized beam passing through the second region penetrates the PBS prism because the polarization direction changes from s to p because of the HWP and is then incident on the quadripartite detector to generate the positioning error signal.

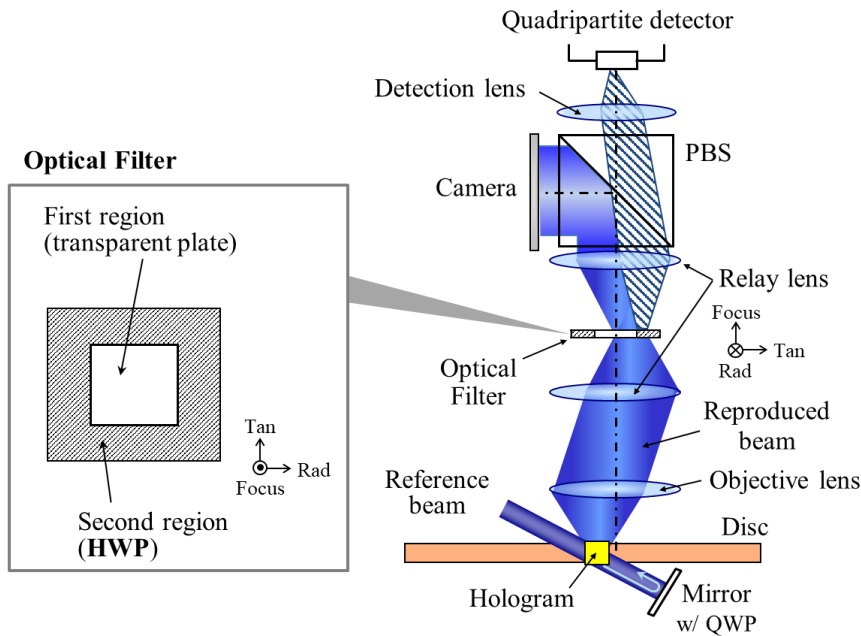


Fig. 5.4 Schematic of new optical filter and beam propagation of reproduced beam.

Figure 5.5 shows a diagram of the situation in which the p-polarized beam illuminates the quadripartite detector. Consequently, the positioning error signal in the tangential direction (TES) can be generated by calculating the output signal from the detector.

$$TES = (DetA + DetD) - (DetB + DetC) \quad (5.3)$$

Similarly, the positioning error signal in the radial direction (RES) can also be generated by calculating the

output signal from the detector.

$$RES = (DetA + DetB) - (DetC + DetD) \quad (5.4)$$

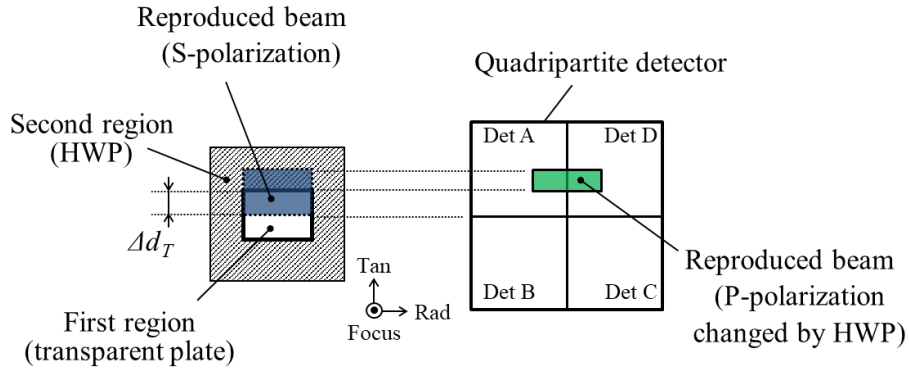


Fig. 5.5 Schematic of situation in which the P-polarized beam for generating positional error signal illuminates the quadripartite detector.

In large-data-capacity HDSSs, stacks of angularly multiplexed holograms (books) are densely located in the in-plane direction of a holographic disk. There is a strong possibility that adjacent books induce a crosstalk noise and decrease the accuracy of the positioning error signal when generating the positioning error signal, because reference beam angles are conventionally set to the same angular configuration in each book when recording holograms, as described in Fig. 5.6(a). To prevent the crosstalk noise from mixing with the positioning error signal, the allocation of reference beam angles was made different among books located next to each other when recording holograms.^{62, 63} For example, the reference beam angle of the 1st hologram page in each even number book is slightly shifted $\Delta\theta_R$ from that in each odd number book in advance, as described in Fig. 5.6(b). If the $\Delta\theta_R$ is much larger than the width of the angular Bragg selectivity of the 1st hologram page, the positioning error signal can be generated using the 1st hologram page without the crosstalk noise caused by adjacent books located next to each other.

Owing to the architecture of the optical filter, the intensity of the reproduced beam illuminating the outer area of the Nyquist aperture can be extracted to generate the positioning error signal while detecting the reproduced beam filtered by the Nyquist aperture for readout.

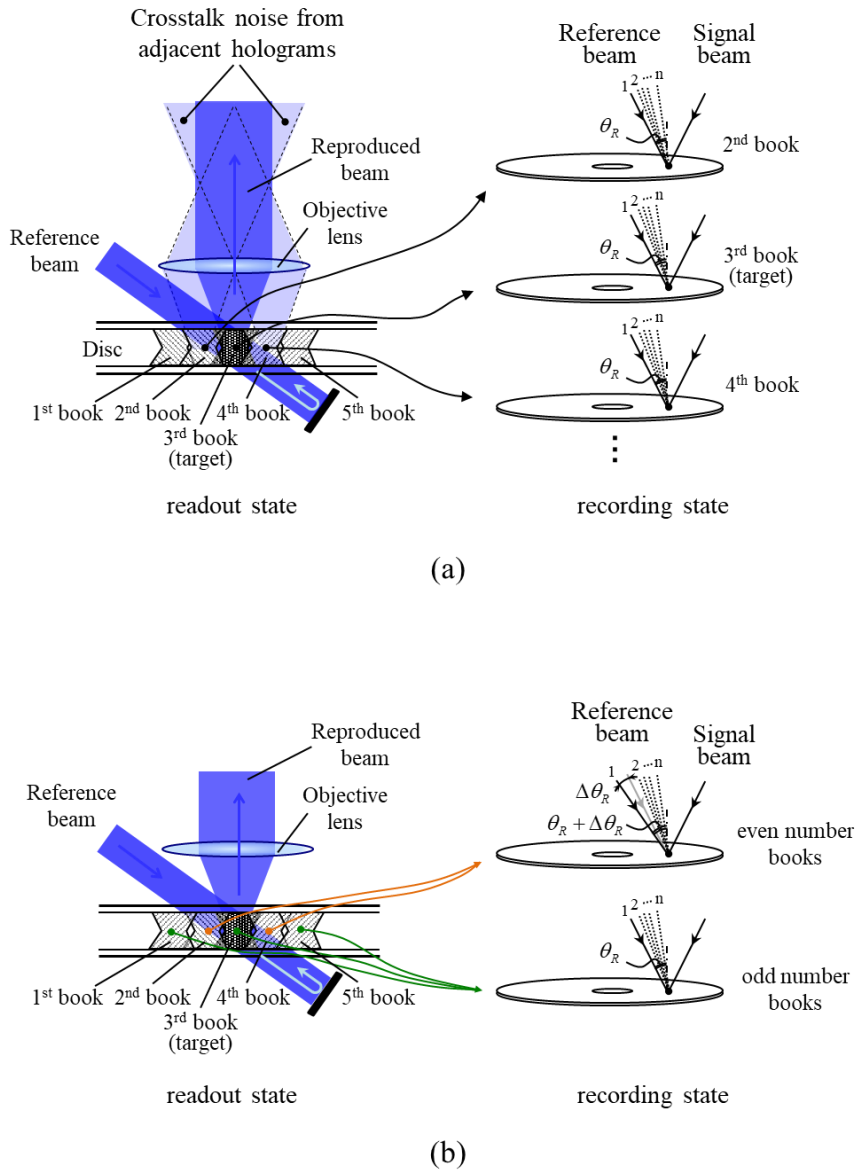


Fig. 5.6 (a) Conventional and (b) proposed angular configurations of reference beam in each book for recording holograms.

5.2 Results and discussion

5.2.1 Validity of compensation for effect of positioning error of holographic disk

The experimental setup for the verification of the compensation method is shown in Fig. 5.7. A blue laser beam 405 nm in wavelength from an external cavity laser diode (ECLD) is divided into the signal and reference beams by a PBS. The amplitude of the signal beam is spatially modulated using data on an encoded page on a 576 x 1152 pixel SLM with an 8 μm pixel pitch. A Nyquist aperture is placed in the signal beam path to reduce the size of the recorded hologram to maximize the recording density and eliminate unnecessary signals

generated from the adjacent hologram for readout. The width of the Nyquist aperture w_{NA} was set to be 1.14 times larger than the Nyquist size D_{Nyq} .

$$w_{NA} = 1.14 \times \frac{0.405[\mu m] \times 40[mm]}{7.8[\mu m]} = 2.4 [mm] \quad (5.5)$$

The focal point of the reference beam is at the back focal plane of the objective lens, resulting in a collimated reference beam at a holographic medium. A second galvano mirror (Galvo2) is placed on the back surface of the medium to retroreflect the reference beam for data recovery in a quasi-phase conjugate readout geometry. The recovered hologram is imaged using a 2000 x 2000 pixel camera with a 5.5 [μm] pixel pitch. In order to verify the validity of the compensation method, the position of the aperture and the holographic medium are adjustable manually in a plane perpendicular to the optical axis, and then an experiment to observe the validity of the method was conducted.

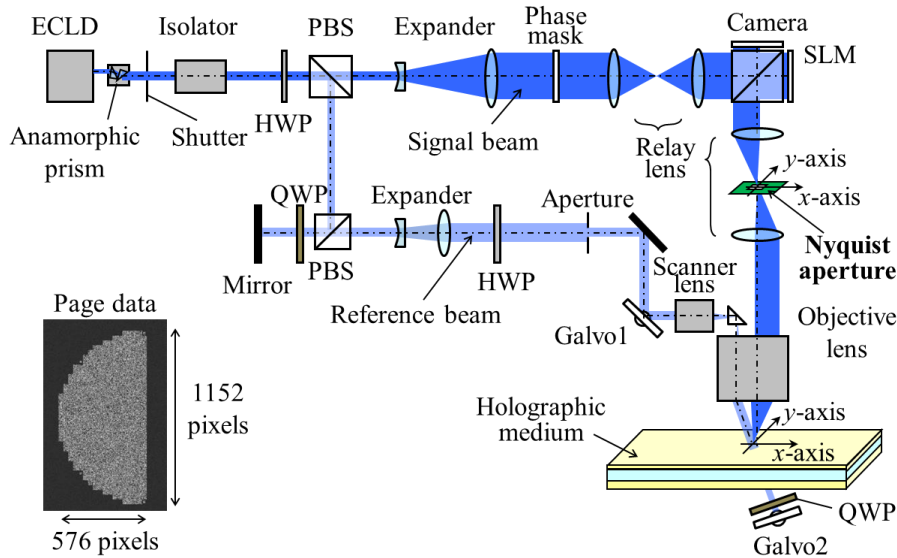


Fig. 5.7 Schematic of experimental setup

Figure 5.8 shows a graph of the experimentally measured and numerically analyzed signal-to-noise ratios (SNRs) by the Layer-by-Layer modeling approach under the condition that (a) the holographic medium is precisely positioned, (b) the medium is displaced (Δd_h) by 100 [μm] in the direction of the x -axis, and (c) the position of the Nyquist aperture is optimally adjusted in the direction of the x -axis while keeping the medium

displacement Δd_h of 100 [μm]. According to Eq. (5.2), the relative displacement (Δd_a) between the reproduced beam and the aperture caused by the medium displacement of 100 [μm] is estimated as

$$\Delta d_a = \frac{40}{12.4} \times 100 = 322 \mu\text{m}. \quad (5.6)$$

The SNR results show that the proposed method effectively compensated for the deterioration of signal quality caused by a residual positioning error of the hologram. On the basis of the same principle, the method is also applicable to the compensation for the effect of a residual positioning error of the hologram in the y -axis.

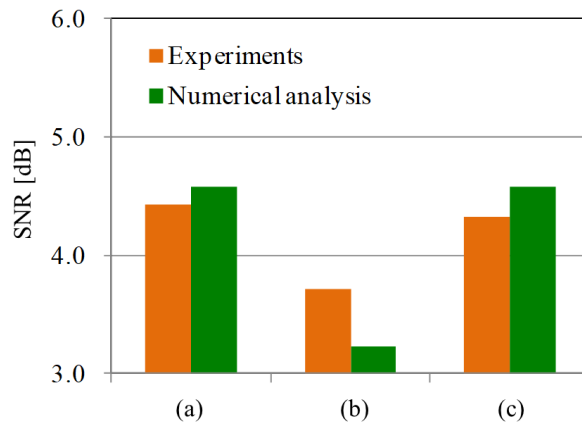


Fig. 5.8 Graph of experimentally measured and numerically analyzed SNRs under conditions that (a) holographic medium is precisely positioned, (b) medium is displaced 100 [μm] in direction of x -axis, and (c) position of Nyquist aperture is optimally adjusted in direction of x -axis while keeping medium displacement of 100 [μm].

5.2.2 Verification of method for generating positioning error signal

In order to verify the validity of the method of generating the error signal, first the illumination pattern of the incident beam on the quadripartite detector described in Fig. 5.4 was observed using the experimental setup shown in Fig. 5.9, where the quadripartite detector in the figure was temporarily replaced with a camera to observe intensity distribution. The movable optical filter in Fig. 5.9 can be moved in triaxial (tangential, radial, and focus) directions using a triaxial actuator. The actuator consists of a biaxial (focus and tangential)

electromagnetic actuator and a single axis (radial) actuator based on a stepping motor, as shown in Fig. 5.10. The configuration of the biaxial actuator is almost the same as that of an objective lens actuator for conventional ODS systems.

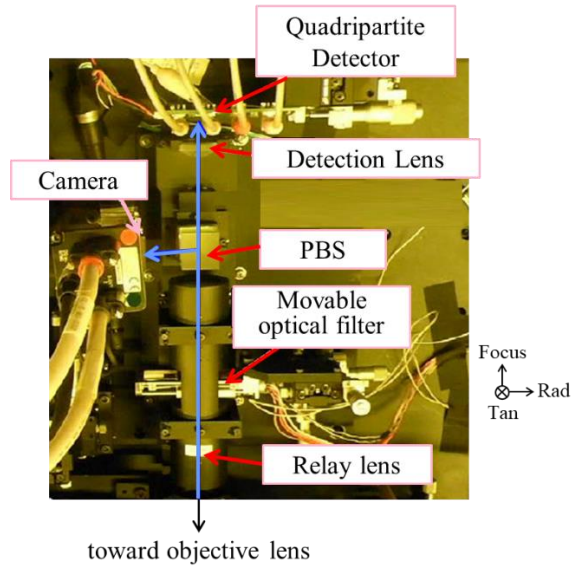


Fig. 5.9 Photograph of part of experimental setup.

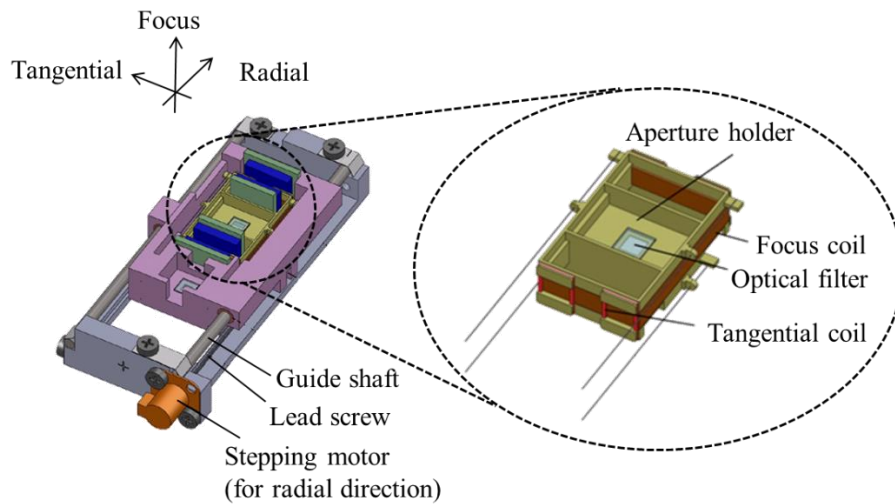


Fig. 5.10 Configuration diagram of triaxial actuator.

Experimental conditions are summarized in Table VI, where the size of the Nyquist aperture in the tangential direction w_{NAt} was half as large as that in the radial direction w_{NAr} , because run-length limited (RLL) coding, which limits the lengths of runs of repeated pixels to two pixels in the tangential direction, was incorporated into the signal modulation for recording holograms in the experiment.⁵²⁾ Adjacent holograms were recorded next to the target hologram like a cross shape in the in-plane direction of the disk to take into account the crosstalk noise generated by the adjacent holograms, although the reference beam angle for recording the adjacent holograms was shifted by $\Delta\theta_{\text{R}} = 0.125$ degree from that for recording the target hologram to suppress crosstalk noise, as explained in Sect. 5.2.2.

Table VI Experimental conditions.

ECLD	Output power for readout	P_o	10	mW
	Wavelength	λ	405	nm
Optical filter	Width in radial (Nyquist aperture)	w_{NAr}	2.4	mm
	Width in tangential (Nyquist aperture)	w_{NAt}	1.2	mm
	Weight (including aperture holder)	M_o	< 1	g
Holographic disc	Weight	M_d	~ 100	g
SLM	Pixel pitch	Δ_{SLM}	7.8	μm
Objective lens	Focal length	f_o	12.4	mm
Relay lens	Focal length	f_r	40	mm
Optical axis with respect to holographic disc	Reference beam	θ_r	48	deg
	Signal beam	θ_s	- 25	deg
Recorded hologram	Width ^{a)} in radial	h_r	0.8	mm
	Width ^{a)} in tangential	h_t	0.7	mm
Reproduced beam	Input power ^{b)}	P_i	~ 9	μW
Quadripartite detector	Sensitivity	η	4.5	V/ μW

a) width in the middle of the depth of the holographic disc

b) input power of beam illuminating the quadripartite detector

Figure 5.11 shows the calculated Bragg angular selectivity curve of the recorded hologram under the conditions shown in Table V. Owing to the angular shift $\Delta\theta_{\text{R}}$, the intensity of the reproduced beam generated

from adjacent holograms could be reduced by approximately 0.7%. Consequently, the crosstalk noise became negligible.

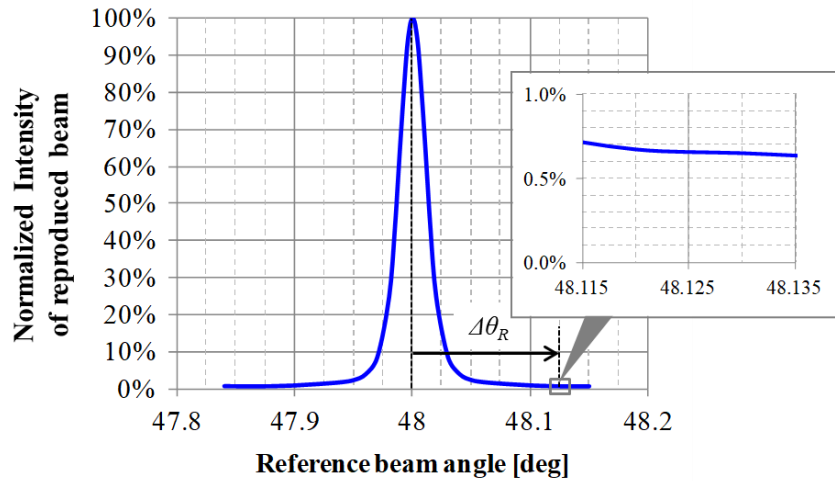


Fig. 5.11 Graph of numerically calculated Bragg angular selectivity curve.

Figure 5.12 shows the observed images when the holographic disk was shifted at different positional displacements in the tangential or radial direction. When the tendency of change in the bright area in these images was focused on, it was confirmed that the bright area expanded in the expected direction, as explained in Sect. 5.2.2. For example, as the displacement increased when the disk was displaced in a tangential direction, it was confirmed that the bright area expanded in the vertical direction in the figure because the area of the reproduced beam protruding from the Nyquist aperture increased. Similarly, it was confirmed that the bright area expanded in the horizontal direction in the figure when the disk was displaced in a radial direction as expected. Likewise, a relatively high beam intensity was observed in the middle of each image in the figure. This high beam intensity was due to a residual hot spot that occurred in the Fourier plane of the objective lens, although a random phase mask was incorporated into the signal beam path to make the intensity distribution spatially uniform. Then, the residual hot spot leaked to the camera during readout in accordance with the extinction ratio of the PBS.

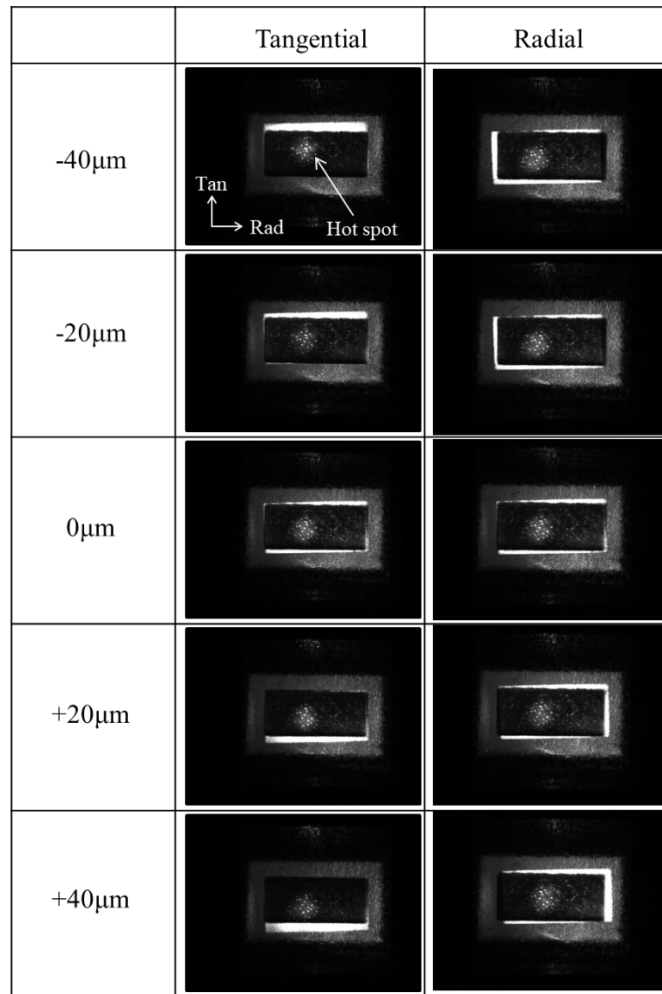


Fig. 5.12 Images observed when holographic disk was shifted at different positional displacements in tangential or radial direction.

Next, the experiment for generating the positioning error signal for the Nyquist aperture control was conducted. Figure 5.13 shows a graph of the error signal generated on the basis of Eq. (5.3) with the positional displacement of the disk in the tangential direction. Although a slight fluctuation was observed in the graph, it was confirmed that the graph was basically linear within the range from -100 to +100 [μm], and the average sensitivity was 12.4 [$\text{mV}/\mu\text{m}$]. Similarly, in the radial direction, a linear graph on the basis of Eq. (5.4) was observed, as shown in Fig. 5.14. The average sensitivity in the radial direction became 6.9 [$\text{mV}/\mu\text{m}$], which was half that in the tangential direction because RLL coding was incorporated in the tangential direction, as previously explained, and the Nyquist size in the tangential direction became half of that in the radial direction.⁵²⁾

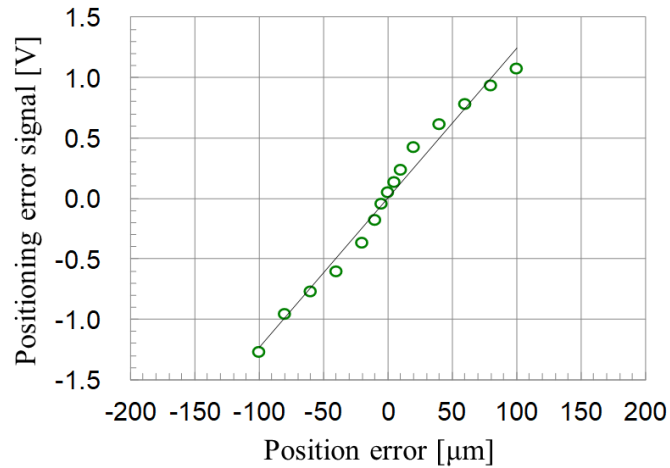


Fig. 5.13 Positional error signal as function of positional displacement of holographic disk in tangential direction.

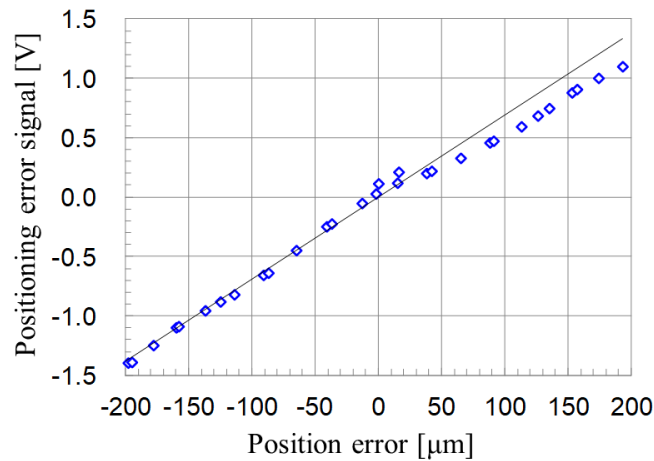


Fig. 5.14 Positional error signal as function of positional displacement of holographic disk in radial direction.

Then, a feedback position control of the Nyquist aperture in the tangential direction was experimentally conducted. The feedback control system block is described in Fig. 5.15. The block consists of the photodetector (PD) circuit, an analog front end, an arithmetic unit, and a servo controller. The PD circuit converts each output current from the quadripartite detector into voltage and then amplifies the voltage signal. The analog front end adjusts the offset of the voltage signal and to reduce noise using a low-pass filter. The voltage signal is inputted into the arithmetic unit. The arithmetic unit calculates the positioning error signal TES accordingly, as

expressed in Eq. (5.3). The servo controller consists of a proportional integral derivative (PID) controller and performs feedback phase compensation of the positioning error signal. Then, the position of the Nyquist aperture can be controlled in the tangential direction depending on the phase-compensated TES.

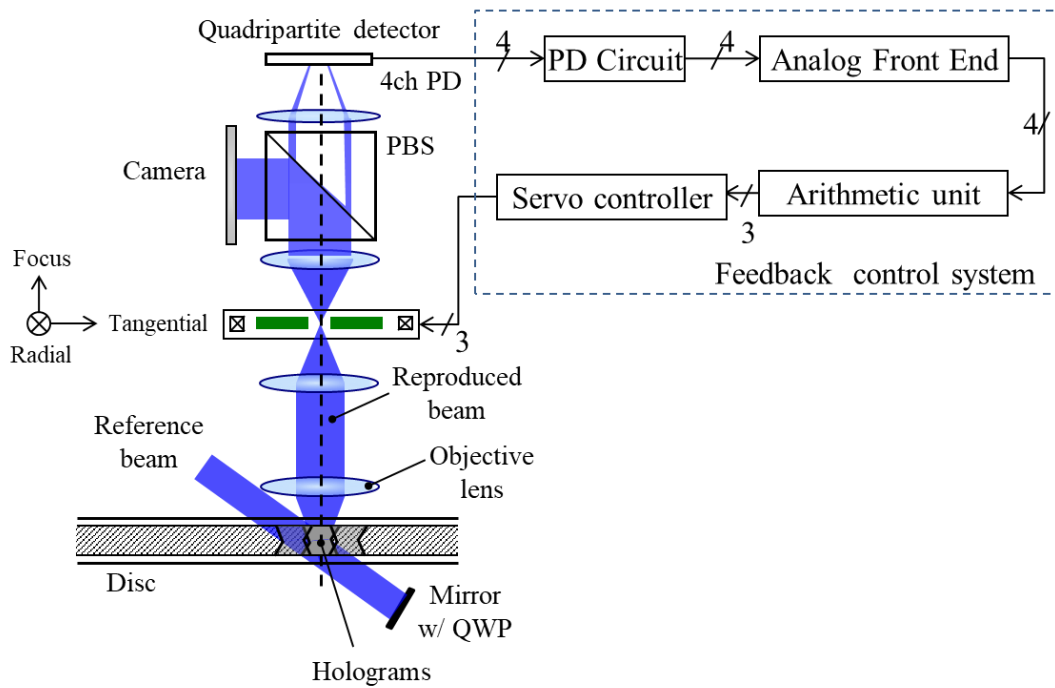


Fig. 5.15 Schematic of feedback control system for positioning Nyquist aperture.

Figure 5.16 shows the experimental results of the positioning accuracy and settling time of the aperture control. A servo pull-in operation was executed at the point of A in the figure when there was a positional displacement of the holographic disk of about 50 [μm] in the tangential direction, which easily occurs owing to the eccentricity of the disk. The graph shows that the servo pull-in was successfully achieved within 10 [ms] and with high accuracy, corresponding to the positioning of the disk in error by less than ±5 [μm].

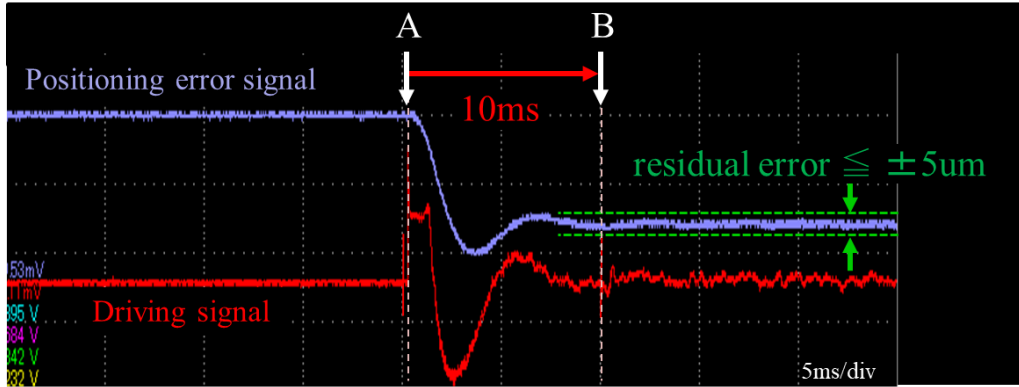


Fig. 5.16 Experimental results of positioning accuracy and settling time of Nyquist aperture control.

Then, a settling time of positioning of a holographic disk under the assumption that the positioning is performed by only the conventional feedback control of a spindle motor based on a certain feedback control error signal was roughly estimated. When the positioning in a tangential direction is performed, the servo control of the rotation angle of the holographic disk employing a stop & go scheme is carried out. For example, when there is positional displacement of 50 [μm] of the holographic disk in the tangential direction at radial position of 40 [mm], the spindle motor needs to rotate the holographic disk by $\Delta\theta = 1.25 \times 10^{-3}$ [rad]. The input parameters for the numerical calculation are summarized in Table VII. Each value of the input parameters was assigned to correspond to specifications of a typical spindle motor.

Table VII Input parameters for numerical calculation of angular control of holographic disk.

Armature resistance	1	Ω
Armature inductance	0.5	mH
Viscous friction coefficient	0.1×10^{-4}	$\text{Nm} \cdot \text{s}/\text{rad}$
Motor voltage constant	0.01	$\text{V} \cdot \text{s}/\text{rad}$
Motor torque constant	0.02	Nm/A
Total inertia of load	0.2×10^{-3}	$\text{kg} \cdot \text{m}^2$
Mass of disc	0.1	kg
Radius of disc	65	mm

Figure 5.17 shows a graph of the numerically calculated step response of the control value $\Delta\theta$ as a function of time. The settling time of the positioning performed by a conventional feedback control based on a spindle motor was estimated to be approximately 100 [ms], which was about 10 times slower than that of the aperture control. That is, owing to the overwhelmingly light weight of the aperture compared with the holographic disk, a fast fine control method to satisfy the positional tolerance of a holographic disk becomes feasible.

In addition, it is considered that the proposed method can also compensate for the effect of the positioning error of the holographic disk in the depth direction of the disk on the basis of the same principle as well as in the in-plane such as tangential and radial directions. The positioning error signal in the depth direction (FES) can be generated by calculating the output signal from the detector.

$$FES = DetA + DetB + DetC + DetD \quad (5.7)$$

Figure 5.18 shows a graph of the error signal generated on the basis of Eq. (5.7) with the positional displacement of the disk in the depth direction. Although the graph is nonlinear to the positional displacement, the Nyquist aperture can be controlled adequately.⁶¹⁾ By using the error signal, the positional displacement of the disk in the depth direction can be suppressed to the amount equivalent to less than ± 20 [μm].⁶¹⁾ The triaxial positioning control of the Nyquist aperture will be extremely useful for relaxing the severe positional tolerance of holographic disks to balance large data capacity with fast readout.⁵⁹⁻⁶¹⁾

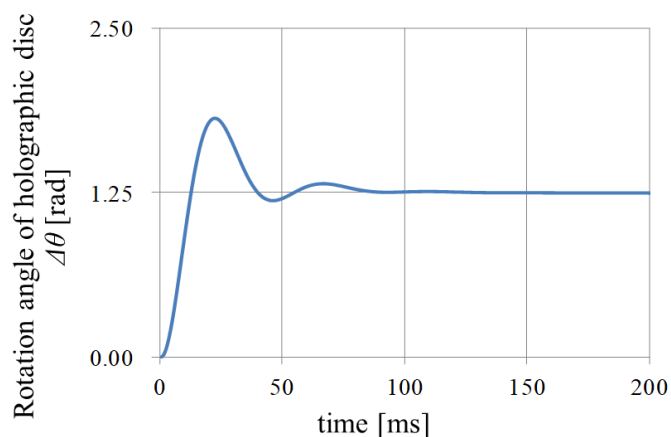


Fig. 5.17 Plot of numerically calculated step response of controlled value as a function of time.

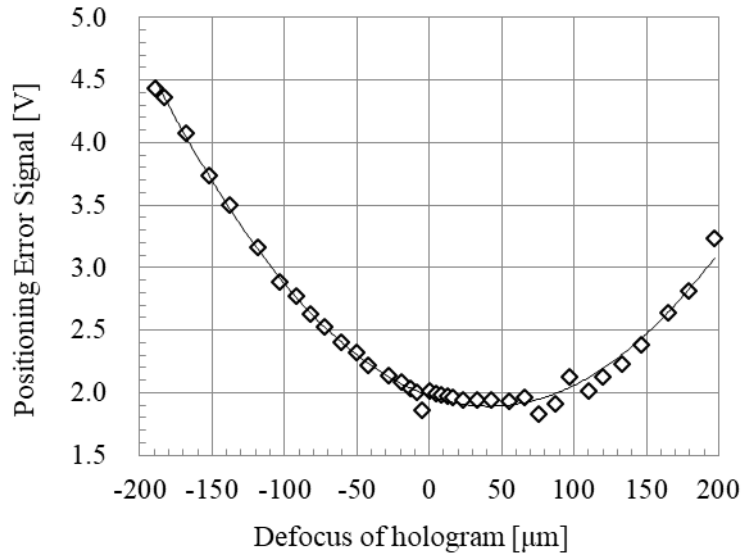


Fig. 5.18 Positional error signal as function of positional displacement of holographic disk in depth direction.

5.2.3 System noise after compensation for effect of positioning error of holographic disk

Owing to the compensation method, the benefit that disk de-track and defocus can be suppressed to the amount equivalent to less than $\pm 5 \mu\text{m}$ and $\pm 20 \mu\text{m}$, respectively, can be received. Therefore, the unique noise caused by disk de-track can be reduced from 20 to 5 [%] [Fig. 5.19(a)]. Similarly, the unique noise caused by disk de-track can be reduced from 25 to 7 [%] [Fig. 5.19(b)].

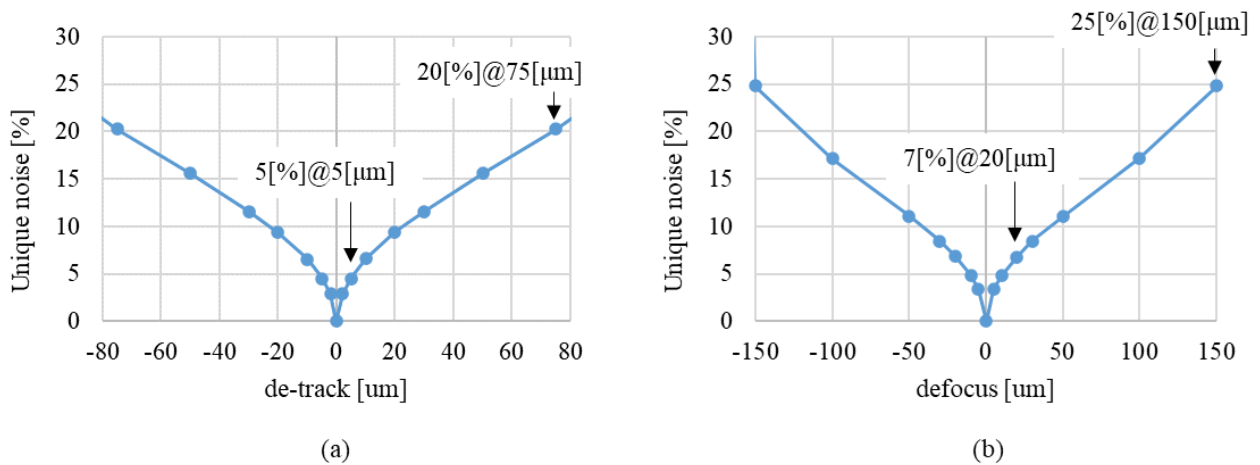


Fig. 5.19 Graph of estimated unique noise caused by (a) de-track and (b) defocus of holographic disk.

Figure 5.20 shows the numerically calculated result of accumulated noise caused by each factor in Table V (a) before applying the compensation method, and (b) after applying the compensation method. By applying the compensation method, the system noise can be reduced below the threshold of $\sigma_N = 56$ [%].

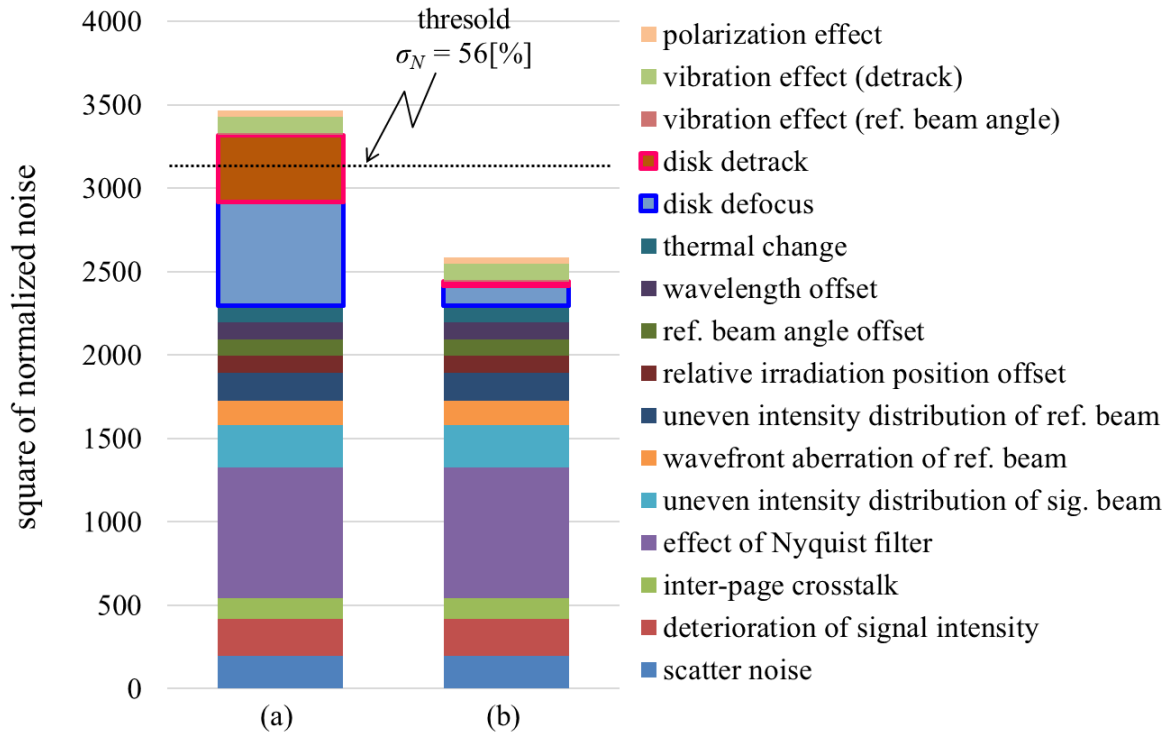


Fig. 5.20 Bar graph of estimated system noise (a) before and (b) after compensation for effect of positioning error of holographic disk.

Figure 5.21 shows the experimental results of acquired SNR when 220 hologram pages were angularly multiplexed at the recording density of 1 [Tbit/in²]. SNR of all of the recorded hologram pages were below the threshold $\sigma_N = 56$ [%].

Through the numerical analysis and experiments, the feasibility of the targeted recording density at 1 [Tbit/in²] was confirmed.

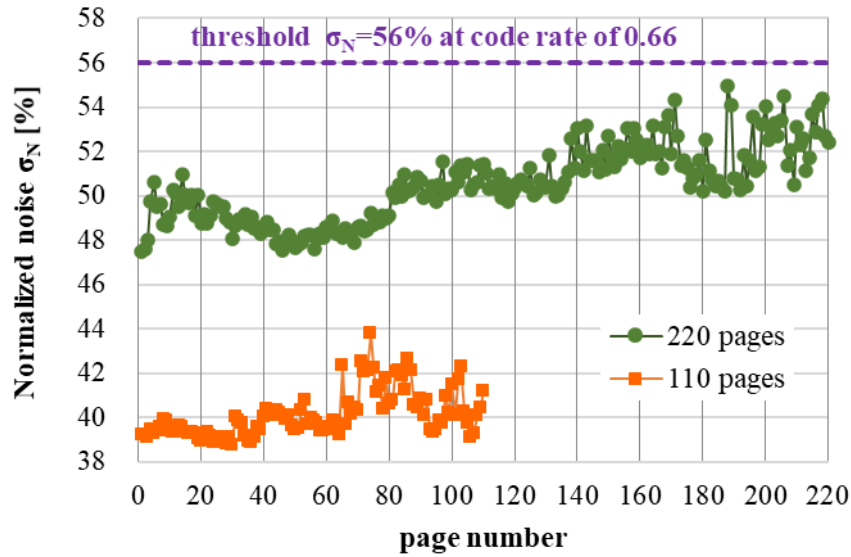


Fig. 5.21 Experimental results of acquired SNR of angularly multiplexed holograms.

5.3 Conclusions

The method for positioning a holographic disk has been devised to strike a balance between large data capacity and fast readout in a HDSS. The method consists of a coarse positioning control performed by spindle or sled motors conventionally and a Nyquist aperture control, which compensates for the effect of a residual positioning error of the disk caused by the coarse positioning. The effectiveness of the compensation method was proven by a preliminary experiment using a HDSS configuration having 576×1172 pixels recorded by high-numerical-aperture (NA) optics with a 405 nm laser and by the simulation corresponding to the specifications of the experimental setup. In addition, to realize the feedback position control of the Nyquist aperture for the compensation, a new optical filter with a HWP was designed to generate a positioning error signal. We confirmed that the positioning error signal, depending on the relative positional displacement between the holographic disk and the aperture, was successfully generated in both the tangential and radial directions by computing the detected signal from a quadripartite detector through the optical filter. Owing to the positioning error signal and the markedly light weight of the Nyquist aperture, which is approximately a hundredth part of the holographic disk's weight, a servo pull-in was successfully achieved within 10 [ms] with high accuracy corresponding to the positioning of the disk with an error of less than ± 5 [μm]. The developed method is applicable to compensating for the effect of positional error not only in the in-plane directions such as tangential and radial directions, but also in the depth direction of the holographic disk on the basis of the

same principle. The triaxial positioning control of the Nyquist aperture will be extremely useful for relaxing the severe positional tolerance of holographic disks.

Then, the system noise at the targeted recording density of 1 [Tbit/in²] was examined through numerical analysis and experiments. The feasibility of the targeted recording density was confirmed because the noise was successfully reduced below the permissible level. By applying the devised method to a HDSS, the realization of a HDSS that strikes a balance between large data capacity of the terabyte class and a fast readout of the gigabits per second class is highly expected.

Chapter 6

Conclusions

The volume of digital data in the worldwide is expanding exponentially every year, then there are many opportunities that require long-term data preservation (LTDP). The tendency of LTDP is increasing because of not only complying with laws and regulations, but also considering acquired digital data as an important asset for the future utilization on business due to the rise of Artificial Intelligence and Data Analytics. The storage media for LTDP is required to store digital data at a low cost because reducing the total cost of ownership is important.

The holographic memory employing angularly multiplexed recording that the dissertation focuses on is a promising candidate as a storage system for LTDP owing to its longevity and low running cost. To realize high recording density which is enough to achieve comparable bit cost against Tape, the dissertation aimed to explore the feasibility of the targeted recording density of 1 [Tbit/in²]. Considering that recording density is proportional to the square of numerical aperture (NA) of an objective lens, a high NA objective lens should be used for high-density recording. However, a high NA objective lens tends to induce an inhomogeneous intensity distribution in the reproduced 2-dimensional (2D) holographic page data because the area of the page data becomes larger due to higher NA ; consequently, it becomes difficult to maintain the uniformity of the intensity profile over the entire area of the page. The inhomogeneous intensity distribution degenerates the signal quality of the data channel. There are several deterioration factors which induces the inhomogeneous intensity distribution. Among them, the dissertation has clarified polarization and vibration effects which have not been sufficiently discussed at previous literatures. The main results of the dissertation were shown in each Chapter.

In Chapter 2, the effect of polarization states of reference and signal beams during recording and readout on a signal amplitude of a reproduced holographic page data was analytically formulated. The amplitude was able to be expressed in the form of multiplying a signal amplitude calculated from scalar diffraction theory by attenuation coefficients dependent on the polarization states, when Born approximation is applicable. By using the analytical formulation, the polarization effect on an intensity profile over the entire area of the page data was clarified without calculation using vector diffraction theory which requires high computational complexity.

Through the numerical analysis and experiments, it was found that s-polarized reference beam was suitable for achieving a uniform intensity profile of the page data. However, even when the reference beam was s-polarized, an intensity degradation in the Bragg degenerate direction in the page data was observed. The intensity decreased by about 30% in an area corresponding to NA of 0.6 in the Bragg-degenerate direction. As the NA of an objective lens becomes higher, the rate of the intensity decrease becomes larger. In order to suppress the intensity decrease, the method which controls the polarization direction of the signal and reproduced beams in-plane direction by applying an area division retarder was developed. Owing to the method, it was confirmed the intensity at the coordinate corresponding to an NA of 0.9 in the Bragg-degenerate direction increased by about 10%.

In Chapter 3, the effects of vibration due to mechanical instabilities on HDSS were formalized by incorporating the concept of time-average holography. By replacing mechanical instabilities of galvano-mirror and spindle motor with oscillation of reference beam angle and holographic disk displacement, these effects were formalized and successfully incorporated into the modeling of data recording and readout process for HDSS based on the Layer-by-Layer method. Owing to the developed numerical formulation, it became possible to quantify the improvement how shorter exposure time of recording hologram suppressed the vibration effects, whereas the improvement had been intuitively understood so far. Through the comparison of the simulation results with experimental results, it was confirmed that the developed optical model was able to predict signal level of the degraded holographic image due to mechanical instabilities.

In Chapter 4, the system parameters of HDSS to achieve the targeted recording density of 1 [Tbit/in²] for realizing the bit cost of 0.01 [\$/GB] was designed. Then, the system noise of the designed system was estimated to confirm the feasibility of the targeted recording density. Owing to the mitigation method, such as applying s-polarized reference beam for readout hologram discussed in Chapter 2, and shorter exposure less than 0.3 [ms] for recording hologram discussed in Chapter 3, the system noise was significantly reduced but still exceeded the permissible level. For further improvement of the system noise, the necessity of suppression of positional error of holographic disk, which also had a large impact on the system noise, was proposed.

In Chapter 5, The method for positioning a holographic disk has been devised to strike a balance between high density recording and fast readout in a HDSS. The method consists of a coarse positioning control performed by spindle or sled motors conventionally and a Nyquist aperture control, which compensates for the effect of a residual positioning error of the disk caused by the coarse positioning. Owing to the positioning error signal

and the markedly light weight of the Nyquist aperture, which is approximately a hundredth part of the holographic disk's weight, a servo pull-in was successfully achieved within 10 [ms] with high accuracy corresponding to the positioning of the disk with an error of less than ± 5 [μm] through experiments.

As a result, the system noise was successively reduced below the permissible level, then the feasibility of the targeted recording density of 1 [Tbit/in²] was confirmed through numerical analysis and experiments. Owing to the results, the realization of a HDSS employing angularly multiplexed recording with the comparable bit cost against Tape became highly promising. It is sincerely hoped that the realization of the HDSS contributes to the transition to a low-oxygen society.

Bibliography

- 1) J. Gantz and D. Reinsel, “*Big Data, Bigger Digital Shadows, and Biggest Growth in the Far East*,” IDC’s Digital Universe Study, p.3 (2012).
- 2) L. Freeman, “*What’s Old Is New Again – Storage Tiering*”, SNIA Tutorial, (2012).
- 3) R. Fontana, G. Decad, “*A Ten Year (2008-2017) Storage Landscape - \$/GB and Exabytes LTO Tape Media, HDD, NAND*”, Int. Conf. on Massive Storage Systems and Technology, (2018).
- 4) Y. Choi, M. Kurebayashi, H. Nishimura, A. Watanabe, and H. Lee, Int. Symp. Optical Memory Tech. Dig., Mo-A-02, (2013).
- 5) Panasonic Corp., “*Optical Disc Data Archiving: A New Age of Cold Data - The Storage Revolution Begins Now*”, White paper, (2017).
- 6) Ministry of Internal Affairs and Communications, “*Report on ICT policy for responding to global warming issues*,” p.50 (2008).
- 7) P. J. Van Heerden, Appl. Opt. **2**, 393 (1963).
- 8) H. Coufal, D. Psaltis and G. T. Sincerbox, Holographic Data Storage (Springer, New York, 2000) p.7.
- 9) L. Hesselink, S. S. Orlov and M. C. Bashaw, Proc.IEEE. **92**, 1231 (2004).
- 10) T. Hoshizawa, K. Shimada, K. Fujita, and Y. Tada, Jpn. J. Appl. Phys. **55**, 09SA06 (2016).
- 11) K. Anderson and K. Curtis, Opt. Lett. **29**, 1402 (2004).
- 12) K. Anderson, SMPTE: Motion Imaging J. **115**, 200 (2006).
- 13) H. Horimai and Xiaodi Tan, “*Collinear technology for a holographic versatile disk*,” Appl. Opt. **45**, 910-914 (2006).
- 14) K. Tanaka, et al., “*415 Gbit/in² recording in coaxial holographic storage using low-density parity-check codes*,” Proc. ODS2009 Tech. Dig. 64 (2009).
- 15) H. J. Eichler, et al., “*High-density disk storage by multiplexed microholograms*,” IEEE J. Select. Topics Quantum Electron. **4**, pp.840-848 (1998).
- 16) K. Saito and S. Kobayashi “*Analysis of Micro-Reflector 3-D Optical Disc Recording*,” Proc. ODS2006 Tech. Dig. 188 (2006).
- 17) T. Shimura, Y. Ashizuka, M. Terada, R. Fujimura, and K. Kuroda, Proc. ODS2007 Tech. Dig., TuD1 (2007).
- 18) S. Zhang, G. Neil, and M. Shinn, Opt. Express. **11**, 1942 (2003).

- 19) J. Hoffnagle and C. Johnson, Appl. Opt. **39**, 5488 (2000).
- 20) Vilkomerson, D. and D. Bostwick, “*Some effects of emulsion shrinkage on a hologram’s image space,*” Appl. Opt. **6**, pp.1270-1272 (1967).
- 21) Jordan, M. and L. Solymar, “*A note on volume holograms,*” Electronics Letters, **14**, pp.271-272 (1978).
- 22) Dhar, L., et al., “*Temperature-induced changes in photopolymer volume holograms,*”. Appl. physics letters, **73**, pp.1337-1339 (1998).
- 23) M. Toishi, et al., “*Evaluation of polycarbonate substrate hologram recording medium regarding implication of birefringence and thermal expansion,*” Optics communications, **270**, pp.17-24 (2007).
- 24) Hoskins, A., et al., “*Temperature compensation strategy for holographic storage,*” in Optical Data Storage Topical Meeting, (2006).
- 25) M. Hosaka, T. Ogata, K. Yamada, K. Yamazaki, and K. Shimada, Jpn. J. Appl. Phys. **55**, 09SA03 (2016).
- 26) K. Yamazaki, M. Hosaka, K. Yamada, T. Ogata, K. Shimada, Opt Rev. **23**, 848 (2016).
- 27) K. Yamada, T. Ogata, M. Hosaka, K. Fujita, and A. Okuyama, Jpn. J. Appl. Phys. **55**, 09SA04 (2016).
- 28) Y. Takahata, Y. Kajiwara, Y. Sasa and M. Yamamoto, “*Relationship between image distortion and bit error characteristics*”, The Institute of Image Info. and Television Engineers, MMS2008-68, (2008).
- 29) T. Oguma, Y. Kajiwara, N. Yoshida and M. Yamamoto, “*Analysis of recording characteristics of photopolymers in holographic memory*”, The Institute of Image Info. and Television Engineers, MMS2009-30, (2009).
- 30) T. Ohori, S. Yoshida and M. Yamamoto, “*Analysis tolerance of holographic memory by simulation*”, The Institute of Image Info. and Television Engineers, MMS2010-17, (2010).
- 31) A. Nakajima, K. Akieda, K. Katakura and M. Yamamoto, “*Influence of reference wave aberration on signal quality*”, ITE Annual Convention 2010, (2010).
- 32) K. Shimada, M. Hosaka, K. Yamazaki, T. Ide, T. Utsugi, M. Nagasawa, T. Mouri, H. Takatsuji, K. Izumi, and H. Suenaga, Jpn. J. Appl. Phys. **57**, 09SC03 (2018).
- 33) H. Kogelnik, Bell System Technical Journal. **48**, 2909 (1969).
- 34) M. Moharam and T. Gaylord, J. Opt. Soc. Am. **71**, 811 (1981).
- 35) N. Kinoshita, H. Shiino, N. Ishii, N. Shimidzu, and K. Kamijo, Jpn. J. Appl. Phys. **44**, 3503 (2005).
- 36) S. R. Lambourdiere, A. Fukumoto, K. Tanaka, and K. Watanabe, Jpn. J. Appl. Phys. **45**, 1246 (2006).
- 37) M. Miura, K. Nitta, and O. Matoba, J. Opt. Soc. Am. A. **26**, 2269 (2009).

- 38) N. Kinoshita, T. Muroi, N. Ishii, K. Kamiyo, H. Kikuchi, N. Shimizu, T. Ando, K. Masaki, and T. Shimizu, *Jpn. J. Appl. Phys.* **50**, 09ME02 (2011).
- 39) R. L. Powell and K. A. Stetson, *J. Opt. Soc. Am.* **55**, 1593 (1965).
- 40) R. J. Pryputniewicz, *Optical Engineering*. **24** [5], 843 (1985).
- 41) T. Usui, K. Watabe, H. Okano, A. Ogawa, Y. Ueda, S. Tatsuta, and Y. Kubota, *Int. Symp. On Optical Memory Tech. Dig. Th-M-01* (2010).
- 42) K. Shimada and Y. Takashima, "*Optical information recording/reproducing apparatus, optical information recording/reproducing method*," United States Patent No. US9977402 (2018).
- 43) K. Shimada, T. Ishii, T. Hoshizawa and Y. Takashima, *Int. Symp. on Optical Memory Tech. Dig. Th-K-02* (2014).
- 44) A. Hoskins, B. Ihas, K. Anderson, K. Curtis, *Jpn. J. Appl. Phys.*, **47**(7S1), 5912 (2008).
- 45) K. Shimada, T. Ishii, T. Ide, S. Hughes, A. Hoskins, and K. Curtis, *Optical Data Storage*, Vol. 7505 of *Proceedings of SPIE-OSA* (2009).
- 46) K. Curtis, K. Anderson, F. Schlottau, T. Ide, K. Shimada, T. Shimano, and H. Miyamoto, U.S. Patent 7742209 (2010).
- 47) K. Shimada, T. Ide, T. Shimano, K. Anderson, and K. Curtis, *Optical Engineering*. **53**(2), 025102 (2014).
- 48) B. Ihas, S. Weaver, K. Anderson, A. Wegner, U.S. Patent 7813017 (2010).
- 49) M. O'Callaghan, *Proc. SPIE 5362, Advanced Optical and Quantum Memories and Computing*, 150 (2004).
- 50) T. Ishii, K. Shimada, T. Hoshizawa, and Y. Takashima, "*Analysis of vibration effects on holographic data storage system*," *Jpn. J. Appl. Phys.*, **54**, 09MA04, pp.1-3 (2015).
- 51) T. Ishii, K. Shimada, T. Hoshizawa, and Y. Takashima, "*Modeling and analysis of vibration effects on signal quality for angular multiplexed holographic data storage*," *Jpn. J. Appl. Phys.*, **55**, 09SA05, pp.1-11 (2016).
- 52) Y. Nakamura, K. Shimada, T. Ishii, H. Ishihara, M. Hosaka, and T. Hoshizawa, "*High-Density Recording Method with RLL Coding for Holographic Memory System*," in *Nonlinear Optics, OSA Technical Digest, OMB5* (2011).
- 53) T. Ishii and K. Shimada, "*Signal quality evaluating apparatus and method, and information recording medium*", United States Patent No. US8184514 (2012).
- 54) T. Ishii, K. Shimada, S. Hughes, A. Hoskins, and K. Curtis, *Tech. Dig. Optical Data Storage, PD1* (2009).

- 55) H. Song, N. Kim, D. Kim, S. Lim, J. Cho, H. Yang, N. Park, K. Park, and Y. Park, *Microsyst. Technol.* **17**, 1057 (2011).
- 56) C. Lee, B. Kwak, C. Chung, and M. Tomizuka, *IEEE/ASME Trans. Mechatronics* **15**, 242 (2010).
- 57) I. Redmond, *Tech. Dig. Optical Data Storage*, MA1 (2006).
- 58) K. Curtis, L. Dhar, A. Hill, W. Wilson, and M. Ayres, “*Holographic Data Storage: From Theory to Practical Systems*,”(Wiley, New York, 2011).
- 59) M. Nagayoshi, K. Shimada, K. Yamazaki, M. Hosaka, and T. Ishii, “*Optical information recording reproducing apparatus*,” United States Patent No. US8804474 (2014).
- 60) K. Shimada, M. Hosaka, K. Yamazaki, and T. Ide, *Int. Symp. Optical Memory Tech. Dig.*, Mo-C-01 (2016).
- 61) Y. Tanaka, T. Ide, J. Hashizume, and T. Hoshizawa, *Int. Symp. Optical Memory Tech. Dig.*, Mo-C-02 (2016).
- 62) T. Ide and K. Shimada, Japan Patent 2009-87448 pending (2009).
- 63) M. Nagasawa, N. Nakai, K. Shimada, T. Ishii, and K. Yamazaki, PCT International Publication WO2016/017020 pending (2016).

List of Publications

Journals

- 1) K. Shimada, T. Ide, T. Shimano, K. Anderson, and K. Curtis, “New optical architecture for holographic data storage system compatible with Blu-ray Disc™ system,” *Optical Engineering*, 53, (2014), 025102, pp. 1–7.
- 2) K. Shimada, T. Ishii, T. Hoshizawa, and Y. Takashima, “New optical modeling and optical compensation for mechanical instabilities on holographic data storage system using time averaged holography,” *Jpn. J. Appl. Phys.* 54, (2015), 09MA01, pp. 1–11. [Spotlights 2015]
- 3) K. Shimada, M. Hosaka, K. Yamazaki, S. Onoe, and T. Ide, “Technique for positioning hologram for balancing large data capacity with fast readout,” *Jpn. J. Appl. Phys.* 56, (2017), 09NA04, pp. 1–8.
- 4) K. Shimada, M. Hosaka, K. Yamazaki, T. Ide, T. Utsugi, M. Nagasawa, T. Mouri, H. Takatsuji, K. Izumi, and H. Suenaga, “Reduction of intensity gradient in two-dimensional holographic data page,” *Jpn. J. Appl. Phys.* 57, (2018), 09SC03, pp.1–7.
- 5) K. Shimada and Masahide Itoh, “Modeling and Analysis of Polarization Effect on Signal Intensity Profile of Two-Dimensional Page Data in Holographic Data Storage System,” *Opt. Comm*, (2021).

Oral Presentations

- 1) ○K. Shimada, T. Ishii, T. Ide, S. Hughes, A. Hoskins, and K. Curtis, “High density recording using monocular architecture for 500GB consumer system,” in Optical Data Storage, Technical Digest (2009), TuC2, pp. 61–63.
- 2) K. Curtis, M. Ayres, A. Hoskins, S. Hughes, T. Ishii, and ○K. Shimada, “Commercial Holographic Data Storage,” in Int. Symp. Optical Memory, Technical Digest (2009), Th-J-01. [invited]
- 3) ○K. Shimada, T. Ishii, T. Hoshizawa and Y. Takashima “New optical modeling of the Effect of Mechanical Instabilities on Holographic Data Storage System using Time Averaged Holography,” in Int. Symp. Optical Memory, Technical Digest (2014), Th-K-02, pp. 196–197.
- 4) ○K. Shimada, T. Ishii, T. Hoshizawa and Y. Takashima, “Modeling and measures against the effect of mechanical instabilities on holographic data storage system,” in Optical Data Storage, Technical Digest (2015), 9587-14. [invited]
- 5) ○K. Shimada, M. Hosaka, K. Yamazaki and T. Ide, “New Compensation for Positioning Error of Hologram for Balancing Large Data Capacity with Fast Transfer Rate,” in Int. Symp. Optical Memory, Technical Digest (2016), Mo-C-01.

Poster Presentations

- 1) ○K. Shimada, M. Hosaka, K. Yamazaki, T. Ide, T. Utsugi, M. Nagasawa, T. Mouri, H. Takatsuji, K. Izumi, and H. Suenaga, “Homogenization of intensity profile of 2D holographic data page in holographic data storage system,” in Int. Symp. Optical Memory, Technical Digest (2017), Tu-J-26, pp. 105–106.